Direct Photon Center-of-Mass Angular Distributions in Proton-Antiproton Collisions at $\sqrt{s} = 1.8$ TeV

A Dissertation

Presented to

The Faculty of the Graduate School of Arts and Sciences
Brandeis University
The Department of Physics

In Partial Fulfillment of the Requirements
for the Degree of

Doctor of Philosophy

by

Leslie F. Nakae
April, 1992

This dissertation, directed and approved by the candidate's Committee, has been accepted and approved by the Graduate Faculty of Brandeis University in partial fulfillment of the requirements for the Degree of

DOCTOR OF PHILOSOPHY

Dean, Graduate School of
Arts and Sciences

MAY 2 4 1992

Dissertation Committee:

James Bensinger, Chairman

Seth Fraden
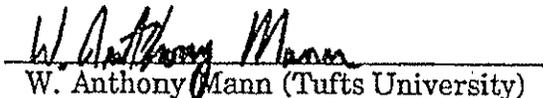
W. Anthony Mann (Tufts University)

Direct photon center-of-mass angular distributions in proton-antiproton collisions at $\sqrt{s} = 1.8$ TeV

Nakae, Leslie F., Ph.D.

Brandeis University, 1992

Abstract

Direct Photon Center-of-Mass Angular Distributions in Proton-Antiproton Collisions at $\sqrt{s} = 1.8$ TeV

by Leslie F. Nakae

The center-of-mass angular distribution of direct photon events, resulting from proton-antiproton collisions at a center-of-mass energy of 1.8 TeV, as measured by the Collider Detector at Fermilab (CDF) during the 1988-1989 experimental run, is presented. The direct photon events are identified primarily through the direct photon's characteristic isolation from other particles. The main source of background is from rare fragmentation of QCD partons into single isolated neutral mesons, which decay into two or more photons. The background is removed statistically by exploitation of the expected difference in the resulting shower profiles. The resulting angular distribution for direct photons, in the transverse momemtum range from 22 to 45 GeV is found to agree favorably with the predictions of Quantum Chromodynamics (QCD) for an interaction with a fermion (spin $\frac{1}{2}$) propagator.

Acknowledgements

The CDF Collaboration

F. Abe,[8] D. Amidei,[4] G. Apollinari,[11] M. Atac,[4] P. Auchincloss,[14] A. R. Baden,[6]
A. Bamberger,[19] A. Barbaro-Galtieri,[9] V. E. Barnes,[12] F. Bedeschi,[11] S. Behrends,[2]
S. Belforte,[11] G. Bellettini,[11] J. Bellinger,[18] J. Bensinger,[2] A. Beretvas,[4] J. P. Berge,[4]
S. Bertolucci,[5] S. Bhadra,[7] M. Binkley,[4] R. Blair,[1] C. Blocker,[2] A. W. Booth,[4]
G. Brandenburg,[6] D. Brown,[6] E. Buckley,[14] A. Byon,[12] K. L. Byrum,[18] C. Campagnari,[3]
M. Campbell,[3] R. Carey,[6] W. Carithers,[9] D. Carlsmith,[18] J. T. Carroll,[4] R. Cashmore,[19]
F. Cervelli,[11] K. Chadwick,[4] G. Chiarelli,[5] W. Chinowsky,[9] S. Cihangir,[4] A. G. Clark,[4]
D. Connor,[10] M. Contreras,[2] J. Cooper,[4] M. Cordelli,[5] D. Crane,[4] M. Curatolo,[5]
C. Day,[4] S. Dell'Agnello,[11] M. Dell'Orso,[11] L. Demortier,[2] P. F. Derwent,[3] T. Devlin,[14]
D. DiBitonto,[15] R. B. Drucker,[9] J. E. Elias,[4] R. Ely,[9] S. Errede,[7] B. Esposito,[5]
B. Flaugher,[14] F. Flintstone,[19] G. W. Foster,[4] M. Franklin,[6] J. Freeman,[4] H. Frisch,[3]
Y. Fukui,[8] Y. Funayama,[16] A. F. Garfinkel,[12] A. Gauthier,[7] S. Geer,[6] P. Giannetti,[11]
N. Giokaris,[13] P. Giromini,[5] L. Gladney,[10] M. Gold,[9] K. Goulianos,[13] H. Grassmann,[11]
C. Grosso-Pilcher,[3] C. Haber,[9] S. R. Hahn,[4] R. Handler,[18] K. Hara,[16] R. M. Harris,[9]
J. Hauser,[3] T. Hessing,[15] R. Hollebeek,[10] L. Holloway,[7] P. Hu,[14] B. Hubbard,[9]
B. T. Huffman,[12] R. Hughes,[10] P. Hurst,[7] J. Huth,[4] M. Incagli,[11] T. Ino,[16] H. Iso,[16]
H. Jensen,[4] C. P. Jessop,[6] R. P. Johnson,[4] U. Joshi,[4] R. W. Kadel,[4] T. Kamon,[15]
S. Kanda,[16] D. A. Kardelis,[7] I. Karliner,[7] E. Kearns,[6] R. Kephart,[4] P. Kesten,[2]
R. M. Keup,[7] H. Keutelian,[7] S. Kim,[16] L. Kirsch,[2] K. Kondo,[16] S. E. Kuhlmann,[1]
E. Kuns,[14] A. T. Laasanen,[12] J. I. Lamoureux,[18] W. Li,[1] T. M. Liss,[7] N. Lockyer,[10]
C. B. Luchini,[7] P. Maas,[4] M. Mangano[11] J. P. Marriner,[4] R. Markeloff,[18] L. A. Markosky,[16]
R. Mattingly,[2] P. McIntyre,[15] A. Menzione,[11] T. Meyer,[15] S. Mikamo,[8] M. Miller,[3]
T. Mimashi,[16] S. Miscetti,[5] M. Mishina,[8] S. Miyashita,[16] Y. Morita,[16] S. Moulding,[2]
A. Mukherjee,[4] L. F. Nakae,[2] I. Nakano,[16] C. Nelson,[4] C. Newman-Holmes,[4] J. S. T. Ng,[6]
M. Ninomiya,[16] L. Nodulman,[1] S. Ogawa,[16] R. Paoletti,[11] A. Para,[4] E. Pare,[6]
J. Patrick,[4] T. J. Phillips,[6] R. Plunkett,[4] L. Pondrom,[18] J. Proudfoot,[1] G. Punzi,[11]
D. Quarrie,[4] K. Ragan,[10] G. Redlinger,[3] J. Rhoades,[18] M. Roach,[17] F. Rimondi,[19]
L. Ristori,[11] T. Rohaly,[10] A. Roodman,[3] B. Rubble,[19] A. Sansoni,[5] R. D. Sard,[7]
A. Savoy-Navarro,[4] V. Scarpine,[7] P. Schlabach,[7] E. E. Schmidt,[4] M. H. Schub,[12]
R. Schwitters,[6] A. Scribano,[11] S. Segler,[4] Y. Seiya,[16] M. Sekiguchi,[16] P. Sestini,[11]
M. Shapiro,[6] M. Sheaff,[18] M. Shochet,[3] J. Siegrist,[9] P. Sinervo,[10] J. Skarha,[18]
K. Sliwa,[17] D. A. Smith,[11] F. D. Snider,[3] R. St. Denis,[6] A. Stefanini,[11] R. L. Swartz, Jr.,[7]
M. Takano,[16] K. Takikawa,[16] S. Tarem,[2] D. Theriot,[4] M. Timko,[15] P. Tipton,[9]
S. Tkaczyk,[4] A. Tollestrup,[4] G. Tonelli,[11] J. Tonnison,[12] W. Trischuk,[6] Y. Tsay,[3]
F. Ukegawa,[16] D. Underwood,[1] R. Vidal,[4] R. G. Wagner,[1] R. L. Wagner,[4] J. Walsh,[10]
T. Watts,[14] R. Webb,[15] C. Wendt,[18] W. C. Wester, III,[9] T. Westhusing,[11] S. N. White,[13]
A. B. Wicklund,[1] H. H. Williams,[10] B. L. Winer,[9] A. Yagil,[4] A. Yamashita,[16] K. Yasuoka,[16]
G. P. Yeh,[4] J. Yoh,[4] M. Yokoyama,[16] J. C. Yun,[4] F. Zetti[11]

[1] *Argonne National Laboratory, Argonne, Illinois 60439*

[2] *Brandeis University, Waltham, Massachusetts 02254*

[3] *University of Chicago, Chicago, Illinois 60637*

[4] *Fermi National Accelerator Laboratory, Batavia, Illinois 60510*

[5] *Laboratori Nazionali di Frascati, Istituto Nazionale di Fisica Nucleare, Frascati, Italy*

[6] *Harvard University, Cambridge, Massachusetts 02138*

[7] *University of Illinois, Urbana, Illinois 61801*

[8] *National Laboratory for High Energy Physics (KEK), Tsukuba, Ibaraki 305, Japan*

[9] *Lawrence Berkeley Laboratory, Berkeley, California 94720*

[10] *University of Pennsylvania, Philadelphia, Pennsylvania 19104*

[11] *Istituto Nazionale di Fisica Nucleare, University and Scuola Normale Superiore of Pisa, I-56100 Pisa, Italy*

[12] *Purdue University, West Lafayette, Indiana 47907*

[13] *Rockefeller University, New York, New York 10021*

[14] *Rutgers University, Piscataway, New Jersey 08854*

[15] *Texas A&M University, College Station, Texas 77843*

[16] *University of Tsukuba, Tsukuba, Ibaraki 305, Japan*

[17] *Tufts University, Medford, Massachusetts 02155*

[18] *University of Wisconsin, Madison, Wisconsin 53706*

[19] *Visitor, BU, Bedrock, BC 100000*

Contents

ix

List of Tables

List of Figures

xvi

Chapter 1

Introduction

High Energy Physics was born of this century to study the fine structure of matter and the forces that govern their interactions. In 1911 Rutherford was able to explain the observed angular distribution of α-particles scattered off of thin sheets of gold by modeling the atoms as dense localized nuclei with a positive charge, thus revealing the basic structure of atoms [1]. In the 1950's Hofstader scattered electrons off of helium nuclei and from the resulting distribution was able to determine the structure of the nucleus [2]. In the late 1960's deep-inelastic scattering experiments (electrons against protons) at the Stanford Linear Accelerator (SLAC) revealed again from the observed angular distribution of the outgoing electrons that the protons themselves also had substructure [3]. This provided some confirmation to a newly developing theory, first introduced independently by Gell-Mann [4] and Zweig [5] in the mid 1960's, that protons, neutrons and other baryons were themselves made from constituents which have been dubbed partons (quarks and gluons). The discovery of the J/ψ resonance in 1974 by independent groups at (SLAC) and at Brookhaven National Laboratory (BNL) all but confirmed the existence of quarks [6][7].

1

One of the paradoxes of particle physics is that it requires more and more energy to probe at a smaller and smaller scale. It is of great irony that the search for hidden clues to the structure of the infir 'tesimally small has led physicists to create mammoth accelerators which are themselves among the most visible of human creations. Indeed the Fermilab Accelerator Ring was one of only two man-made structures identifiable to observers on the Space Shuttle (the other being the Great Wall of China). However, while the accelerator sizes and their energies have increased dramatically over the years and the theories to explain their behavior have become more intricate, the basic experimental methods and techniques have remained the same. Physicists still scatter beams of particles off other particles and observe the rates of interactions and their angular distributions.

In the 1970's much of the known interactions and observed behavior of these particles were incorporated together into a relatively simple formalism which has become known as the 'Standard Model'. Briefly, in the Standard Model there are two basic types of particles, quarks and leptons, which are the constituents of matter, and bosons which mediate the interactions between them. The quarks and leptons are all fermions (spin $\frac{1}{2}$) and each come in 'six flavors' split into three generations of doublets, all but one of which (top) have been observed in some form. See (Table 1).

Particles interact with each other *via* four forces, three of which, strong, electromagnetism and weak are incorporated into the Standard Model and one, gravity, is currently not. The most familiar force, electromagnetism (EM), is beautifully described by the abelian gauge theory, quantum electrodynamics (QED), which models the force as an exchange of virtual photons (γ's) between charged particles. The modeling of a force well described macroscopically since the previous century by Maxwell's equations, at a microscopic level

2

Quarks			Leptons		
Flavor	Mass(GeV/c^2)	Charge(| e |)	Flavor	Mass(GeV/c^2)	Charge(| e |)
U Up	4×10^{-3}	$+\frac{2}{3}$	ν_e	$< 2 \times 10^{-8}$	0
D Down	7×10^{-3}	$-\frac{1}{3}$	e Electron	5.1×10^{-4}	-1
C Charm	1.5	$+\frac{2}{3}$	ν_μ	$< 3 \times 10^{-4}$	0
S Strange	0.15	$-\frac{1}{3}$	μ Muon	0.106	-1
T (Top)?	> 89	$+\frac{2}{3}$	ν_τ	$< 4 \times 10^{-2}$	0
B Bottom	4.7	$-\frac{1}{3}$	τ Tau	1.784	-1

Table 1.1: The Standard Model Particles

as the exchange of virtual gauge bosons (photons) was a triumph of modern physics. In QED the potential between particles is expanded into a perturbation series where the coefficient of expansion α_{em} is small, $\sim \frac{1}{137}$. The smallness of α_{em} guarantees that the perturbation series converges rapidly and each higher order term is of decreasing magnitude (after renormalization).[1] The real beauty of QED, and the key to its general acceptance, is the linkage between the perturbation expansion of the potential and a pictorial representation of each term (Feynman Diagrams) relating the theoretical formula term by term to an imagined interaction between particles. See figure 1.1 for a first order QED Feynman Diagram of compton scattering.[2]

QED has strongly influenced theoretical particle physics ever since its introduction in the 1930's, from its limited first order success, to its incredible quantitative results obtainable after renormalization. In the standard model this picture has been expanded to include the weak force and the strong force which are also modeled by the exchange of

---

[1] QED had the longtime problem that although the first order terms are well behaved and give reasonable results, the higher order terms all have mathematical infinities associated with closed loops. This was eventually handled independently in the late 1940's by Feynman, Tomonaga and Schwinger by incorporating the infinities (a limited number to all orders) into the field constants (electric charge and mass) and rescaling. This prescription is known as 'renormalization'.

[2] Calculations to first order in perturbation theory are called Leading-Order (LO), second order Next-to-Leading-Order (NLO), etc.
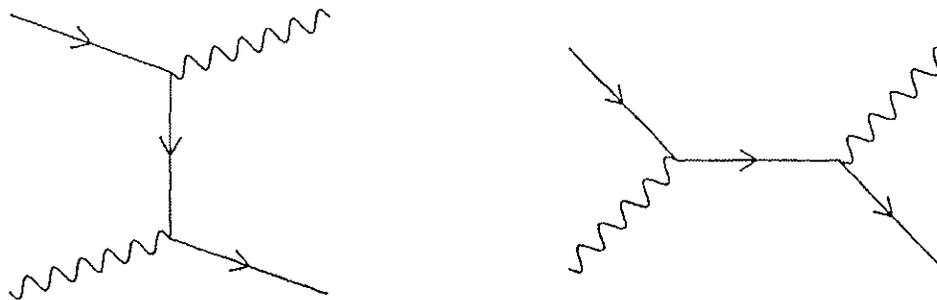
Compton Scattering (QED)

Figure 1.1: Compton Scattering:First Order QED diagram. Time flows from left to right. A incident electron and photon (left) scatter, with an electron propagator, the resulting electron and photon (right) exit with new energy and momenta. Fermion arrows with time indicate a particle (electron), reverse arrows would indicate antiparticle (positron).

4

Force		Boson			
Force	Coupling Strength	Boson	Mass(GeV/c^2)	Charge($|e|$)	Spin
Strong	~ 1	Gluon	0	0	1
EM	$\frac{1}{137}$	Photon	0	0	1
Weak	10^{-5}	$W^{\pm}, Z^0$	80.0,91.16	$\pm 1, 0$	1
Gravity	10^{-38}	(Graviton)?	?	0	2

Table 1.2: Standard Model Fundamental Forces

virtual gauge bosons. The weak force (which for example governs the nuclear decay of a neutron into a proton + an electron and neutrino) was incorporated into the unified Electroweak Model by Weinberg, Salam and Glashow in the late 60's, where the exchanged bosons for the weak force are the massive W^+'s, W^-'s, and Z^0's [9] [10] [8]. The strong force (which governs nuclear interactions and binds the like-charged protons together in the nucleus with neutrons) was incorporated in a slightly *ad hoc* fashion into the current theory, Quantum Chromodynamics (QCD), by assuming that the strong force is mediated by its own massless gauge boson, the gluon. The structure of QCD (force carried by the exchange of gauge bosons) was due principally to the success of the unified electro-weak theory. It is an observed peculiarity incorporated into the Standard Model that leptons do not couple strongly and that unlike the leptons and other gauge bosons, quarks do not exist in a singlet free state but rather only in certain allowed states called hadrons that carry an additional degree of freedom, 'color' charge, described by the symmetry group SU(3). Hadrons are only seen to exist in 'colorless' states of baryons, three quarks (qqq), or mesons, quark antiquark ($q\bar{q}$) pairs.[3] In Table 2 the four known forces have been ordered by the strengths of their couplings and matched with their appropriate boson.

---

[3]The term color coming from the analogy that one can form net colorless (white) light from mixing red, green and blue in equal proportions or by adding color plus anticolor.

As one can see the strong force is much 'stronger' than the other forces and would dominate all interactions if all particles had net color. However as stated above, leptons have no color and hadrons can only exist in net colorless states, so at the macroscopic level the effects of the strong force are rarely seen. At the planetary scale, gravity, by far the weakest of the four forces, dominates all interactions because large scale objects have no net charge or color. At the molecular scale EM effects dominate, gravity is insignificant and strong effects are still not seen. Strong interactions can only be observed by studying nuclei, or by studying hadrons at sufficiently high energy that the hadrons begin to lose cohesiveness and there is net local color. When scattering occurs between hadrons at sufficiently high energies one would naively expect to be able to liberate the partons in an analogous fashion to the ionization of an electron from an atom, or the breaking apart of an atomic nuclei, which occur at lower energies; however this is not what is observed. What is seen, first at the ISR ($\sqrt{s}$=44 and 53 GeV) [11] [12] in the early 1970's, are streams of tightly collimated hadrons and leptons (jets) confined to relatively small solid angles. These streams of particles are thought to represent the final states of the initial colliding partons, whose characteristics such as momentum, charge, color and other quantum numbers all sum to conserve the characteristics of the initial pair of colliding hadrons but only in the form of colorless hadrons and leptons.

In recent years with the advent of the high energy hadron colliders at CERN, the SPS with $\sqrt{s} = 600$ GeV, and at Fermilab, the Tevatron with $\sqrt{s} = 1800$ GeV, the observation of high momentum jets has become common and it has permitted the investigation of QCD, the theory of strong interactions. The 'strong' nature of QCD means that the strong force dominates all reactions that involve the strongly interacting particles, quarks and gluons.

6

For this reason at high energy hadron colliders like CERN and Fermilab, the dominant observed reactions of interest are jet events where all that is seen in the detector are two or more jets (figure 1.2).

Other less common types of events are of course possible and one such subclass of QCD events of particular interest is the subject of this dissertation. These events are characterized theoretically by the presence of an electromagnetic vertex in the Feynman diagram from which a Direct or Prompt Photon emerges and is observed as as real photon in the detector balanced by one or more jets (figure 1.3).

The direct photon events therefore are a hybrid of two distinct processes, one vertex is a strong vertex, described by QCD and the other, electromagnetic, described by QED. Direct photon events are of interest for several reasons. First experimentally while QCD jets have a very distinctive signature for detection they are subject to many measurement uncertainties such as statistical fluctuations for particles and non-linearities in the detector that cause measuring differences between single and multiple particles of the same energy (*i.e.* $E \neq \frac{E}{2} + \frac{E}{2}$). While these same uncertainties also exist in EM events,[4] they are much worse and far more complicated in hadronic jet events. The shower development of photons and leptons in EM calorimeters is better understood so the experimental uncertainty in the measurement of photon energies is smaller than for hadronic jets. Secondly, the presence of an EM vertex in the diagrams makes the theoretical calculations far more tractable and while QCD has been calculated to next-to- leading order[5] in α_s there also exists calculations

---

[4] An EM event is an event where one or more legs is electromagnetic in nature (*i.e.* a photon or an electron) and therefore at least one leg is measured electromagnetically (as opposed to hadronically).

[5] In QCD, LO events are characterized by two outgoing partons and NLO by three outgoing partons. In the detector this is seen as two and three jets respectively or in the case of direct photons, γ+1jet and γ+2jets.
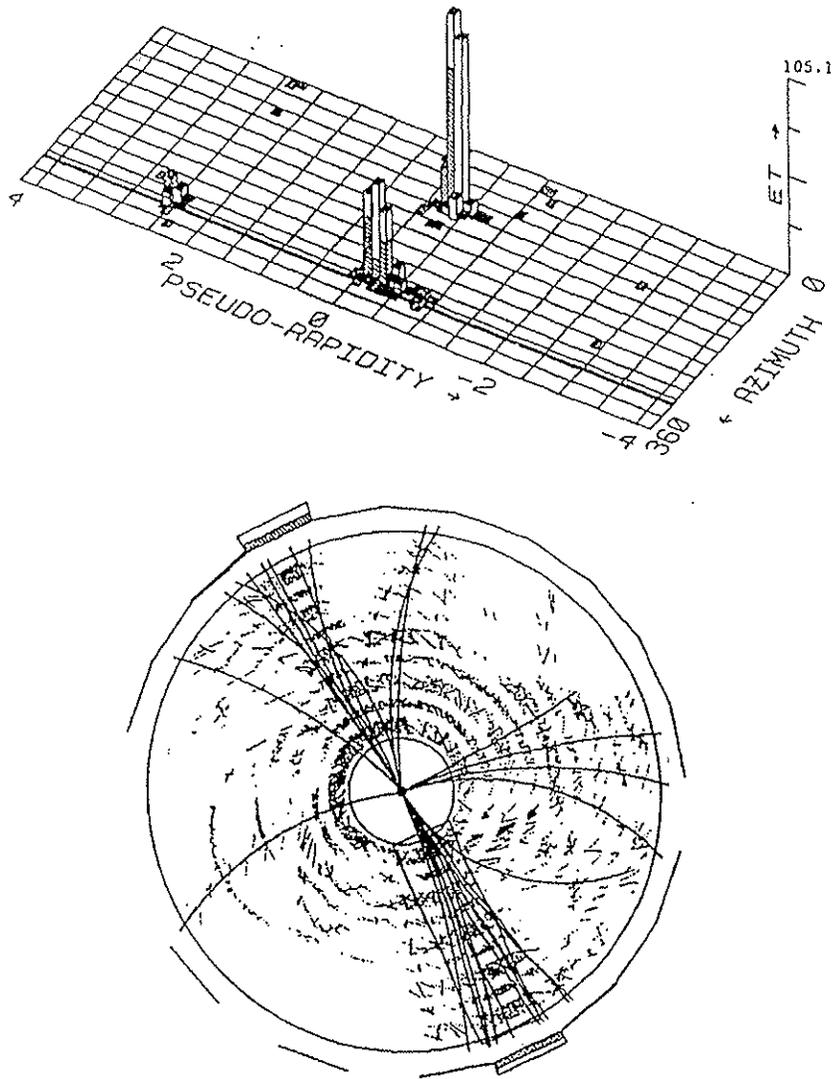
Figure 1.2: Central Dijet Event: Lego and CTC Plot. The top picture shows the energy deposition of the event within the CDF calorimeters. In this view the cylindrical barrel of the calorimeter has been unfolded so the azimuthal angle ϕ is shown linearly. The two jet clusters appear clearly in the view with a mixture of electromagnetic (hashed) and hadronic (clear) energy. The lower picture is a projection of the Central Tracking Chambers (CTC) collapsed along pseudorapidity η. The dots are hits in the CTC and the lines are reconstructed tracks. The jet clusters in this view are clearly back-to-back (opposite) in ϕ and since the jets are central, high momentum (straight looking) CTC tracks from charged particles can be seen pointing at the clusters. This is a very high P_T event as is evident from the large number of straight tracks (see Chapter 2).

8
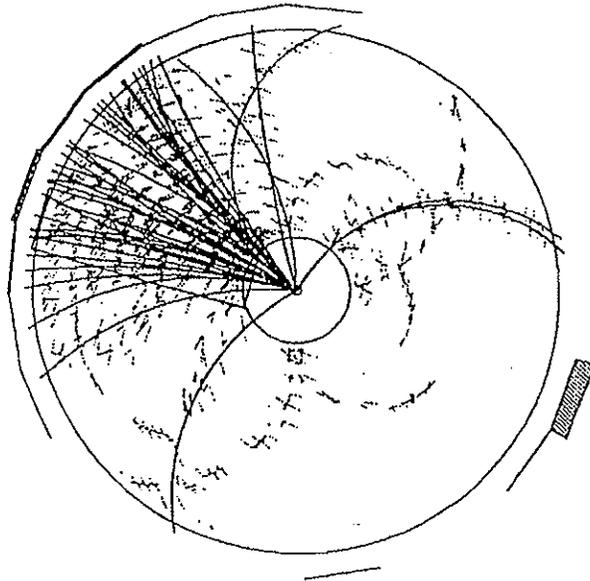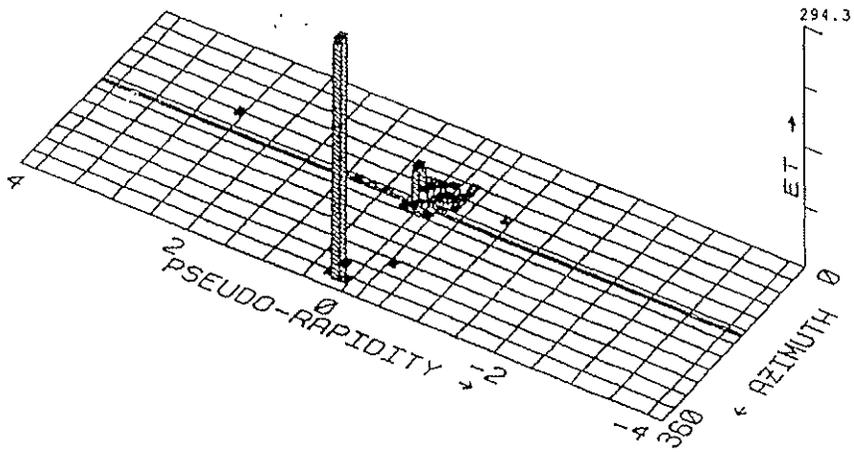
Figure 1.3: Direct Photon Candidate Event: Lego and CTC plot. A not-so-typical, very high P_T, Photon(γ)+jet event. Photon triggers were all in the central. Nearly all of the photon candidate energy is electromagnetic (hashed). Note the absence of any high momentum track pointing to the photon candidate cluster in the CTC picture.

9

of direct photon events to this order that are theoretically easier to calculate. Direct photons are also simply a distinct identifiable process that are calculated differently theoretically from other QCD processes and should provide an interesting independent check of QCD. It will be the subject of this thesis to measure the center of mass (CM) angular distribution of the direct photon process and compare it to the best available theoretical calculation of QCD, which includes NLO. These points will be elaborated upon in the next chapter.

Chapter 2

The Parton Model, QCD and

Direct Photons

2.1 The Parton Model and Hadronic Interactions

When scattering at very low energies, that is, when the momentum transfer scale (Q^2) is small, on the order of MeV's, hadrons will scatter as a coherent unit and the effects of QCD and the evidence for quark-gluon substructure are not seen. As the center of mass momentum increases (and consequently the Q^2) the observances become quite peculiar. The scattering no longer acts as though the collision occurs between two objects with the total momentum of the two incoming particles but rather as between objects with some fraction of the momentum. Even stranger yet, occasionally the incoming and outgoing particles no longer remain the same and whole streams of collimated particles (jets) are observed to exit a reaction and it may be that none of the outgoing particles are the same as the incoming particles. The apparent scattering of objects with some portion of a hadron's

11

total momentum is the evidence for the existence of hadron substructure and the basis of the quark model.

Naively from the Standard Model one can think of baryons such as protons and neutrons as being constructed of three valence quarks (qqq) and mesons such as π's and η's as consisting of valence quark anti-quark pairs ($q\bar{q}$). Hadrons are thought to consist of the aforementioned valence quarks as well as a sea of virtual gluons and quark-antiquark pairs that collectively share the total energy and momentum of the hadron. These hadron constituents are denoted by the nonspecific term of parton, coined by Feynman. The parton model attempts to explain the observed scattering of hadrons as the interaction between individual constituent partons from each of the incoming particles. QCD is currently the best theory that describes the interactions between these partons and will be elaborated upon here.

In the Parton Model, high energy collisions between hadrons are considered phenomenologically. While in the case of hadron colliders the beam energy and therefore the incoming hadron momentum may be fixed, the momentum sharing among the constituent partons implies that an individual parton may have any fraction of the total hadron momentum. Therefore a fixed energy hadron collider, unlike a lepton collider, has the feature (and the curse) that its collisions sample a broad range of the interacting parton CM energies. Figure 2.1 is a schematic representation of a high energy collision between two hadrons and can be referred to for a visualization for all that follows. The two circles at the left represent each of the incoming hadrons, in this case a proton (P) and an antiproton ($\bar{P}$).

A parton from each hadron with momentum fractions X with probability F(X) scatter with some cross section (σ) and angular distribution and the partons then hadronize

12
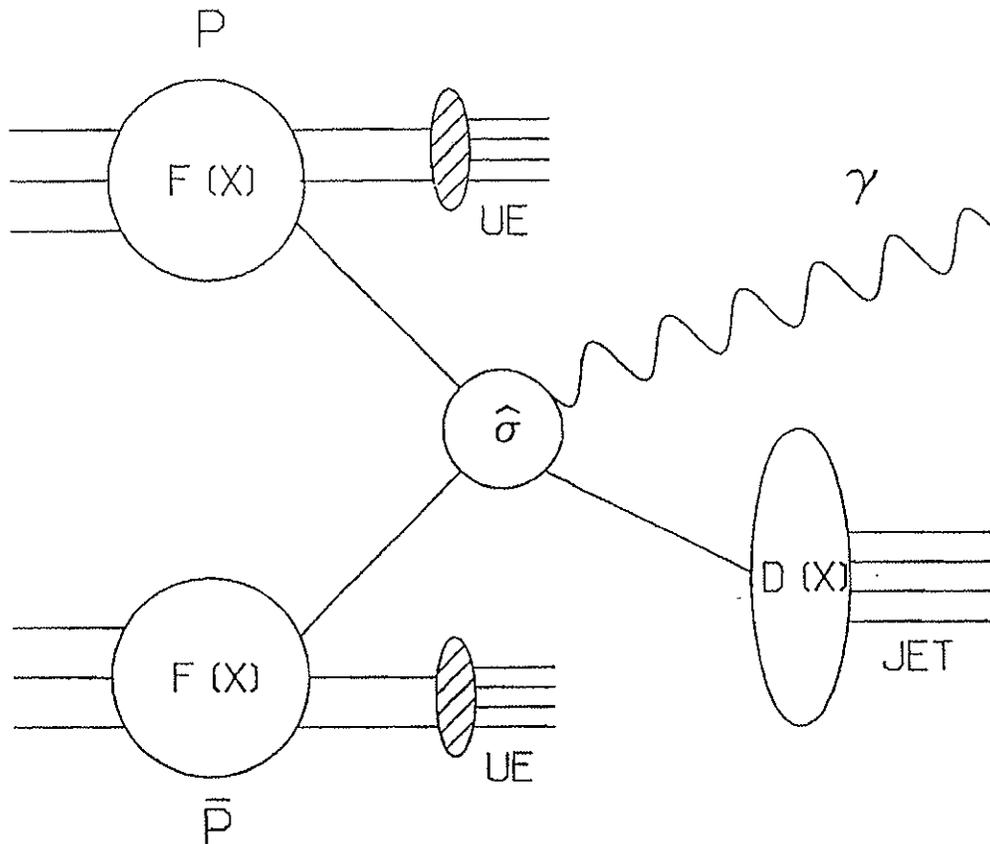
Figure 2.1: Schematic Representation of High Energy Collisions. The circles at left represent incoming proton and antiproton. An energetic parton from each scatter and any outgoing partons hadronize (fragment) into real particles. In this investigation in the signal one outgoing leg is a direct photon. The background is a fragmentation of one outgoing parton into a 'single' energetic neutral meson. See text.

13

(fragment) according to some function D(X) becoming real particles that are ultimately measured in the detector. The cross section (σ), the structure functions (F(X)), and the fragmentation function (D(X)) are ultimately dependent upon the details of the strong force. However, the only quantitative model available is QCD which is calculable only for so-called 'hard' scatterings which are events that have large momentum transfers. UE in the figure stands for the Underlying Event, which represents the remaining momentum of the incoming hadrons, carried by the partons not involved in the hard scattering.

The cross section for the hadronic scattering in figure 2.1 can be written in equation form as:

$$(2.1) \qquad \frac{d\sigma}{d\Omega} = \sum_{ij} \int dx_1 dx_2 F(x_1, Q^2) F(x_2, Q^2) \frac{d\hat{\sigma}_{ij}}{d\Omega}$$

Where i and j label the incoming partons, x_1 and x_2 are the intial momentum fractions of each of the partons, Q^2 is the momentum transfer scale, and the $\hat{\sigma}$'s are the individual parton cross sections which are the processes calculated by QCD.

Structure functions (the F(X)'s) are empirical functions which were originally obtained from deep inelastic scattering experiments (electrons and neutrinos scattered from protons). The structure functions are the average momentum distributions of the hadrons and can be found by considering many interactions and measuring the initial and final state momentum of the scattering leptons. There are two major difficulties involved with obtaining the structure functions in this fashion. First of all, lepton scattering can only reveal the momentum distribution of quarks and therefore the gluon structure functions must be inferred from the unaccounted for momentum; this is done by invoking the momentum sum

14

rule which requires the total momentum fraction of all the parts =1.0. Secondly, current lepton scattering occurs at much lower energies than hadronic collider energies, with corresponding lower average momentum transfers, and therefore must be evolved to the proper energy scale. The evolution can be handled through the Altarelli-Parisi equations [13] and is not a significant problem, but uncertainty as to what might be the proper choice of Q^2 for a given reaction is a significant problem. Figure 2.2 shows the structure functions and their evolution as a function of total hadron energy and Q^2. There are many different sets of structure functions that have a fairly broad range of parton distributions; however, since by definition $\cos\theta^*$ is boosted back to CM the different structure functions have very little effect on the angular distribution (after normalization the structure function differences are obscured by the width of a line). The structure functions used here are EHLQ1 [14].

2.2   Direct Photons and QCD

The present theory of the strong force, which dominates the interactions of partons, is the perturbative non-abelian gauge theory, QCD.[1]

In QCD, partons' fields of 'color' charge interact with each other /it via gluons, the mediating gauge bosons. The non-abelian nature of QCD means that gluons also carry 'color' charge (unlike photons in QED) and therefore can couple with other gluons. Additionally in perturbative QCD, the coupling 'constant' α_s is not actually a constant, but varies with the momentum transfer scale Q^2. An approximation for α_s is given by

---

[1]Technically QCD is not necessarily a perturbative theory (it has a well defined lagrangian). However, like most problems, the lagrangian has no closed solution and the only known way to obtain quantitative results is through perturbative methods.
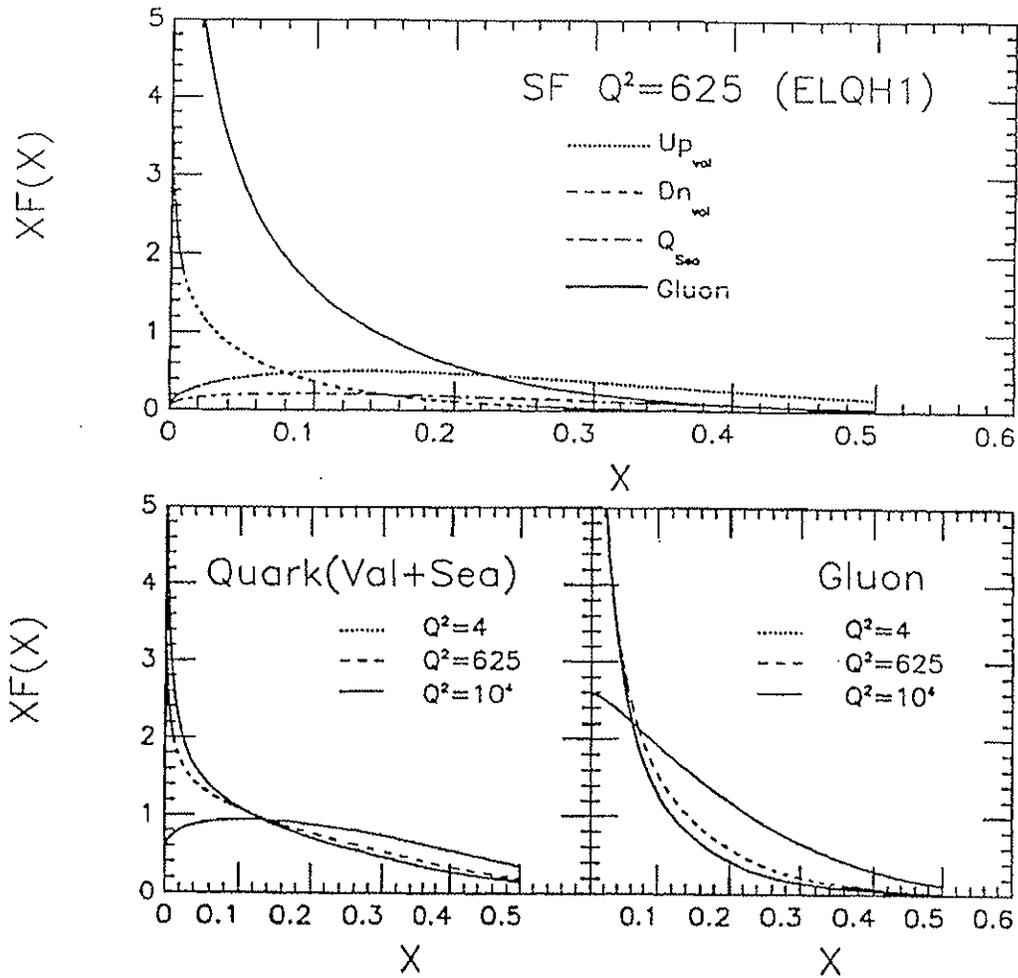
Figure 2.2: Structure Functions F(X) which represent the probability of finding a parton with momentum fraction X=p/P_{hadron} between X and X+dX. The upper figure is a composite for the valence up and down quarks, sea quarks, and gluons with Q^2 chosen to be 625, and the lower figure shows the evolution of structure function for different choices of Q^2 for contribution of all quarks, and gluons. Structure functions used here are EHLQ1.

$$(2.2) \qquad\qquad \alpha_s(Q) = \frac{1}{B \ln \frac{Q^2}{\lambda^2}}$$

where $B = \frac{(33-2f)}{12\pi}$ and f is the number of quark flavors.

The 'running' of α_s is an important feature of the theory and is needed to give the theory two essential characteristics at each end of the energy spectrum, confinement and asymptotic freedom. At high energies (short distances) and therefore in the region of high momentum transfers, the strong force coupling becomes weak enough for partons to behave like free particles ('asymptotic freedom'). However at lower energy scales, when the physical separation is larger, about the size of a proton (1 fermi=10^{-15} meters), the coupling between partons is so strong that instead having free energetic partons, quark-antiquark pairs are produced that are formed into hadrons (fragmentation) that have no net color charge. The low energy behavior of QCD explains why partons are 'confined' within hadrons and never seen as free particles. α_s becomes small enough where a perturbation expansion is meaningful only when Q^2 is large, on the order of a few GeV. This means that for the vast majority of hadronic collisions, in the region of soft gluon exchange (small Q^2), QCD is not calculable by perturbation theory. Perturbative QCD is only reliable in the region of hard scattering where large momentum transfer occurs and α_s is sufficiently small. Therefore we will endeavor to select 'hard-scattering' events to test this theory in a calculable region.

Fragmentation is itself a soft process and therefore the real particles produced have very little momentum transverse to the parton direction and therefore what should be observed are streams of collimated particles (jets), each one traveling in almost the same direction as the original outgoing parton. For the softly scattering partons this means that the outgoing particles travel along the direction of the beam and are not measurable; however, in the case

17

of hard scattering events the jets are easily detectable with significant momentum transverse to the beam direction.

The constituent pair of particles or partons that collide to give the interesting hard process are treated independently from the other partons which interact softly with each other and therefore continue moving in the same direction as the initial state hadrons. In practice these 'spectator' partons continue down the beamline and are not directly measurable but will carry away some net momentum along the beam (longitudinal direction) and therefore the longitudinal momentum of the hard-interacting pair of partons will not sum to zero. This prevents one from using the lab as the center-of-mass of the system. The lab system always has an arbitrary Lorentz boost, with respect to the center-of-mass system, mostly along the beam direction (Z-axis). For this reason the study of QCD is concentrated on the transverse components of momentum (P_T) and energy (E_T) which are not boosted much on average in the lab. It is also convenient when dealing with relativistic particles, to define the variables rapidity (y) and pseudorapidity (η). Rapidity is a theoretically interesting variable which is defined so that a Lorentz boost amounts to a shift of the origin along the boost axis (*i.e.* rapidities are additive). It is also observed that the average particle density is roughly flat in $\frac{dn}{dy}$ and $\frac{dn}{d\phi}$.

$$(2.3) \qquad y = \frac{1}{2} \ln \left(\frac{E + P_z}{E - P_z} \right) = \frac{1}{2} \ln \left(\frac{1 + \beta \cos\theta}{1 - \beta \cos\theta} \right)$$

Pseudorapidity (η) is an experimental variable that is a close approximation to rapidity. They are equal when $\beta = 1$, that is, when the rest mass $=0$. For high energies this is a

18

very good approximation and simplifies measurements considerably because psuedorapidity simplifies into an expression that is dependent only upon the easily measured polar angle θ (see figure 2.3). From here we will assume equality and substitute η for y in measurements.

$$(2.4) \qquad\qquad \eta = \frac{1}{2} \ln \left(\frac{1 + \cos\theta}{1 - \cos\theta} \right)$$

As mentioned above, QCD is a perturbative theory with the additional feature that the coefficient of expansion α_s gets smaller with increasing Q^2. Since before the interaction there is very little P_T for any parton, if one chooses events with sufficiently high P_T it guarantees that the momentum transfer Q^2 is sufficient for perturbative QCD to be viable. The non-abelian nature of QCD means that the gluons can self-couple and hence the internal loop diagrams have non-zero contributions and the theory itself only logarithmically converges. Therefore unless one is at extremely high P_T, higher order terms are not negligible and the importance of Next-to-Leading-Order calculations is obvious.

The direct photon diagrams have one of the strong vertices replaced by an EM vertex. The EM vertex is described by QED which is well understood and the most successful of all physics theories. This simplifies calculation of the lowest order diagrams (figure 2.4) and any higher order diagrams (figure 2.6). In part because one vertex is well behaved and well understood, but mostly because there are many fewer diagrams to calculate than in purely QCD diagrams (figure 2.5).

The additional diagrams are due mainly to the fact that gluons unlike photons can self-interact so there are many more possible internal loops in QCD than in QED. To first

19
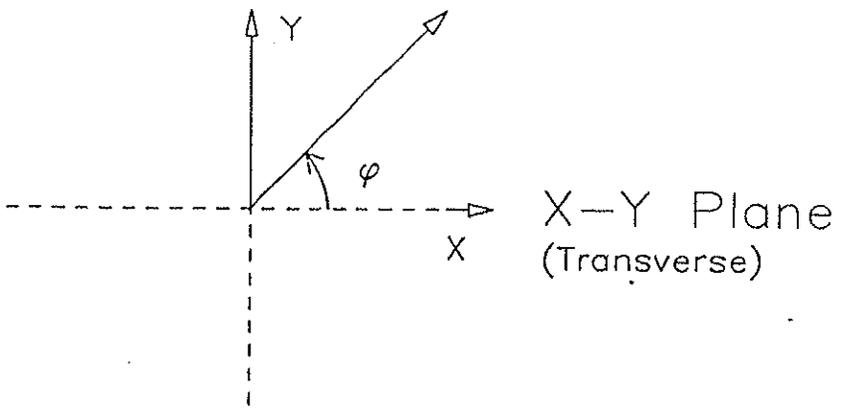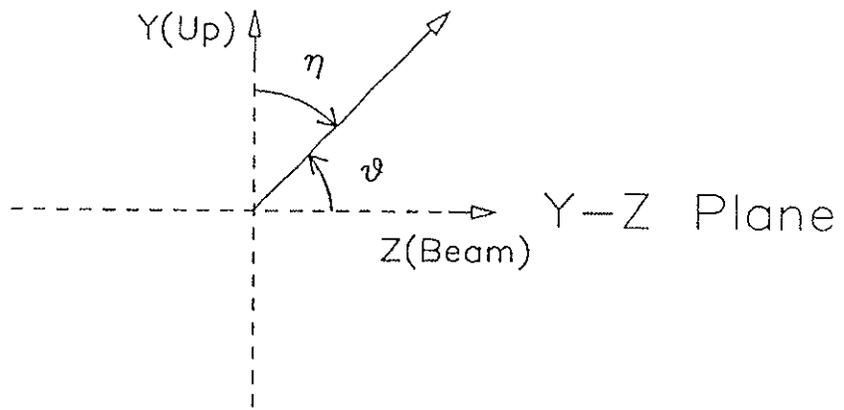
Figure 2.3: Definition of Variables.
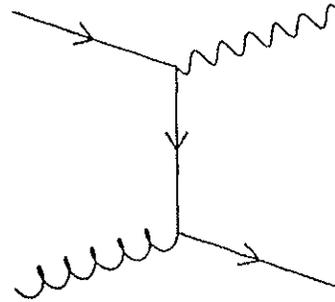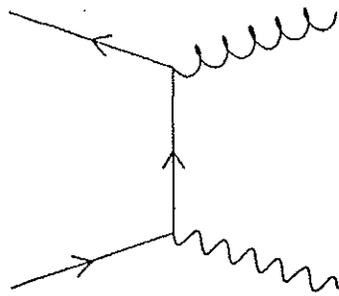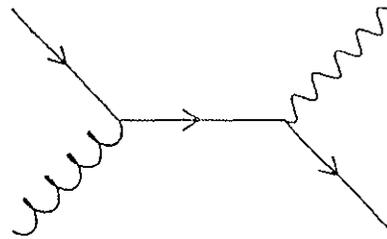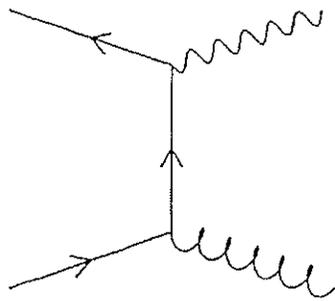
a) Annihilation   b) Compton

Figure 2.4: Lowest Order Direct Photon Diagrams. The dominant process is the Compton subprocess (qg→ γq) which is 75-80% of the cross section. Annihilation (q$\bar{\text{q}}$ → γg) is 20-25%. This comes from the higher fraction of gluons than quarks in the structure functions at Tevatron energies. (Compare the diagrams of b) to figure 1.1; they are the same except with a gluon replacing the intial state photon.)
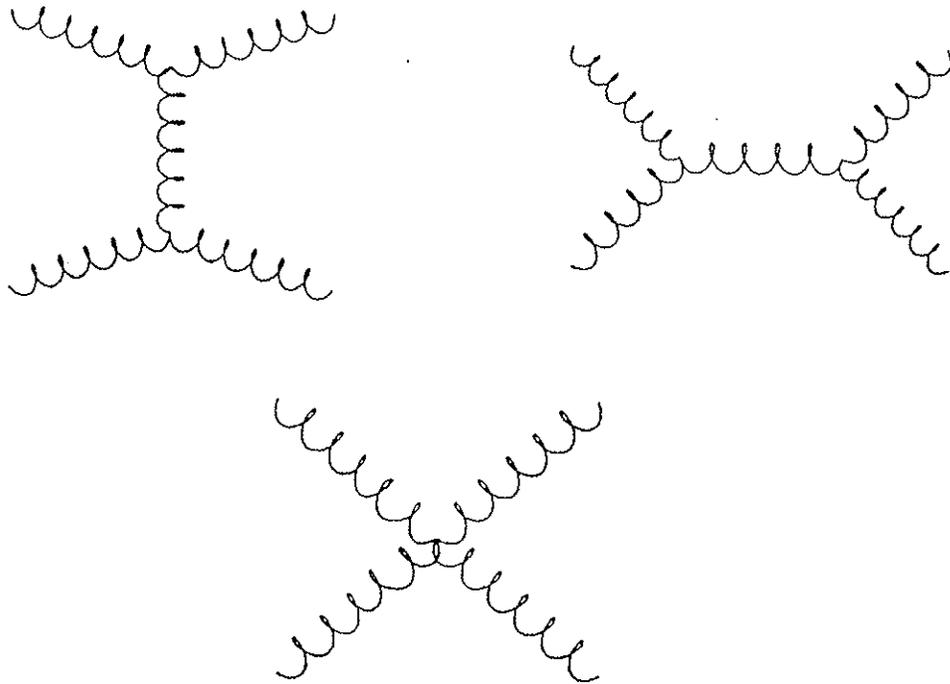
Gluon Fusion (Tree-Level Only)

Figure 2.5: Dominant QCD diagrams. Gluon-Gluon scattering (gg → gg).

order in α_s ($O(\alpha_s^2)$), there are only 2 direct photon subprocesses[2] and 4 diagrams but 4 dijet subprocesses or 10 diagrams. However there are also radiative corrections or so called 'loop' diagrams that contribute to these $O((\alpha_s^2)$) calculations that contribute even more diagrams, 6 for the direct photon subprocesses and 28 for the dijet subprocesses (which leads to hundreds of separate terms) [15]. The number of separate diagrams contributing to each process is even more disparate as the order of the calculations increase. (There are no fewer than 21 Direct Photon diagrams and 11 single loop diagrams for the Compton subprocess alone to $O(\alpha\alpha_s^2)$ [16]; there are hundreds of $2 \to 3$ process multijet diagrams.) Some of the NLO direct photon diagrams can be seen in figure 2.6, grouped by subprocess.[3]

Therefore the theoretical uncertainties of direct photon calculations are smaller. There exists a next-to-leading order calculation of direct photon production by Owens [17] and a more recent calculation by (Pierce and Hincliffe) [18] that we can compare to the data. This makes direct photon production a potentially more stringent test of QCD than the purely QCD jet processes as well as simply a distinct separate calculation.

One of the ways in which the direct photon calculation is distinct from a purely QCD calculation is in the expected angular distribution of the the outgoing partons. At Collider energies hard scattering events are far more likely to involve gluons than quarks and so the dominant leading order QCD process is $gg \to gg$ with a gluon (spin 1) propagator (see figure 2.5). The dominant leading order direct photon diagram is $qg \to q\gamma$ with a quark (spin $\frac{1}{2}$) propagator (figure 2.4). The former (see Appendix A) should have an angular distribution where $\frac{dN}{d\cos\theta^*}$ goes $\sim \sin^{-4}\left(\frac{\theta^*}{2}\right)$ (just like Rutherford Scattering) and the latter goes like

---

[2]By a subprocess we mean a group of terms (diagrams) that have identical initial and final state particles.

[3]In figure 2.6 we have ignored time ordering, so additional diagrams can obviously be found by turning diagrams on their sides or considering gluon radiation from various legs.
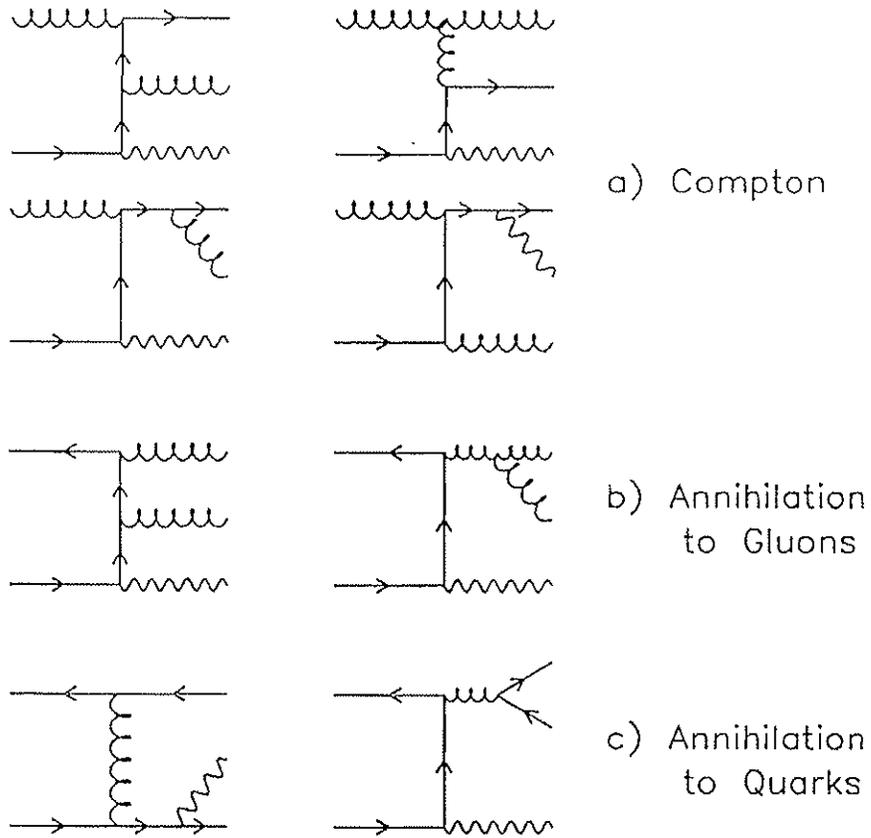
Figure 2.6: Some NLO direct photon diagrams divided into subprocesses. a) qg → γqg, b) q̄q → γqq̄, c) q̄q → γgg. Time ordering has been ignored.

$\sim \sin^{-2}\left(\frac{\theta^*}{2}\right)$ (θ^* being the CM scattering angle). Figure 2.7 is the QCD prediction of $\cos \theta^*$ for dijets and direct photon events.

The dijet prediction (dots) and the LO direct photon (dashes) are LO QCD calculations done from tree-level graphs only (Papageno) [19], and the NLO direct photon (solid) is a full NLO calculation with the partons merged within cones to match CDF jet definitions and in order to handle the collinear singularities [17].

2.3 Experimental Motivation and Showering

There are also several experimental advantages to selecting DP events. Direct photons have a very distinctive signature for triggering, a cluster of mostly EM energy in the calorimeter with no charged track balanced in ϕ by a hadronic jet. In testing QCD there is always one unavoidable complication. Theoretically the outgoing partons are quarks and gluons which, because of confinement, are never seen experimentally as partons but only in form of real mesons and baryons. The linkage from theory to experiment is made by identifying QCD jets and associating them with outgoing patrons from theory. There is always some uncertainty as to what exactly constitutes a jet. For simplicity CDF defines a jet *via* a cone drawn around the centroid of large (GeV scale) energy depositions; the exact algorithms used are discussed in Chapter 4. Here we illustrate some of the ambiguities. Jets consist of multiple particles clumped together within a relatively small solid angle, but there is always some question as to which particles close by also might have originated from the same parton, not to mention the difference between single and multiple particle measurements. No calorimeter is perfectly linear in its response so one particle of energy E will not on average deposit the

25

Direct Photon dN/dCosΘ* Theory
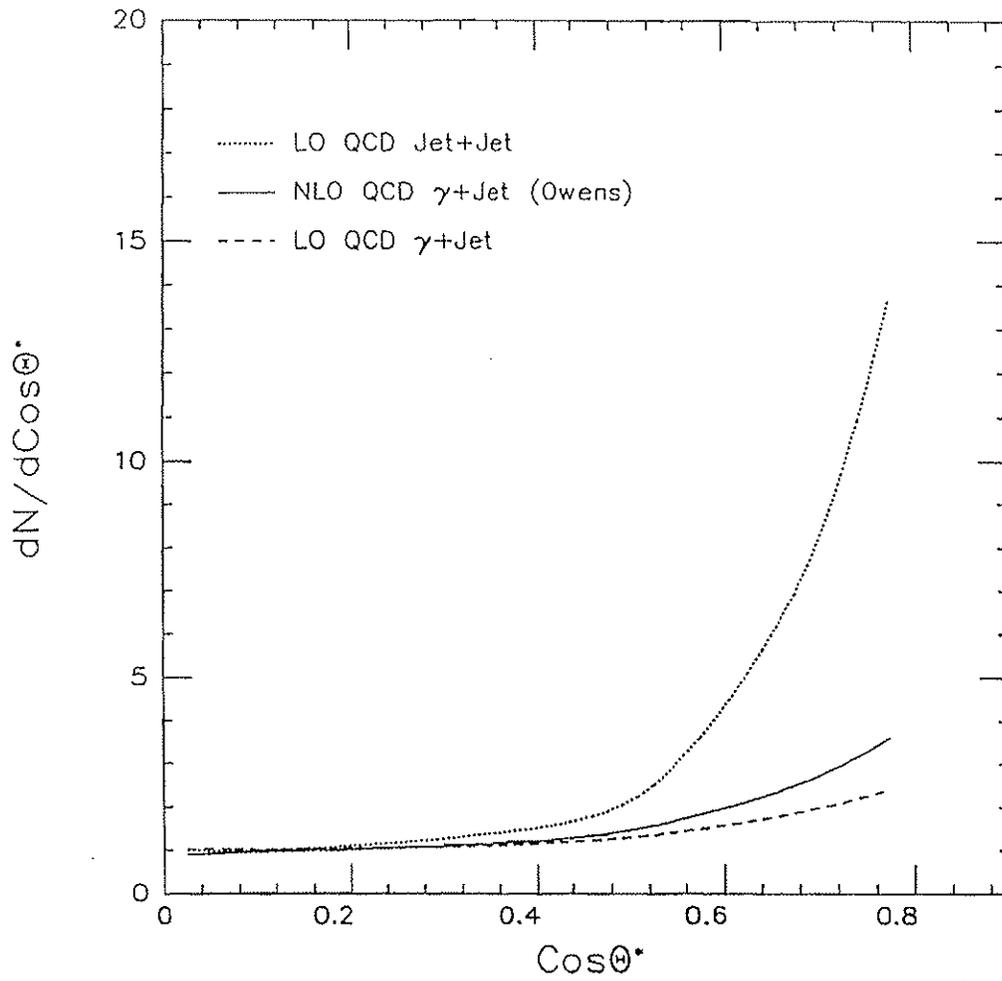
Figure 2.7: Cosθ^* Predictions from Theory. Note the relative steepness of the curves. The curves are normalized to an equal area (=0.3) for $|\cos\theta^*| < 0.3$.

same amount of energy as two identical particles, each with energy E/2. Therefore partons of the same energy that fragment into different numbers of particles will on average give a different detector response. Direct photons have the advantage that they are *explicitly* the outgoing particle predicted by the theory and that there is little ambiguity of identification. Additionally the actual measurement of energy, once identified, is better for photons than jets.

To measure energy, the CDF detector uses a series of sampling calorimeters which are described in more detail in the following section; here we wish to briefly describe the measurement advantages of direct photons. Electromagnetic showers are relatively simple and well understood. The shower develops simply as a photon traveling through matter (lead absorbers in the CDF EM calorimeters) which interacts with the charge of the nucleus, and pair-produces. Each electron then passes through more matter and again interacting with the charge on another nucleus, creates another photon through bremstrahlung radiation and then the process repeats itself, eventually leading to a whole stream of photons and electrons collectively sharing the momentum of the original particle. The individually charged electrons then interact with the detector medium, scintillator in the case of the CDF Central EM calorimeters. The passage of charged particles through scintillator produces light whose intensity is proportional to the number and energy of the particles. The hadron calorimeters work similarly; however, the interactions are not driven by EM forces producing electrons and photons, but rather by strong forces in the nucleus producing more hadrons and breaking up nuclei. A considerable amount of the energy in a hadronic shower goes into breaking up the nucleus of the absorbing media or is transferred to slow neutrons and is not measured. Most of the energy going into hadrons goes into producing charged

pions (π^+ and π^-) and they will go on showering by the same process, interacting with other nuclei in the absorbing media. Eventually the charged pions are detected just like electrons in the detecting media, scintillator in the CDF central hadron calorimeters. However a third of the energy goes into producing neutral π^0's which decay quickly into 2 $\gamma's$ that shower electromagnetically and therefore leave a different signature in the calorimeters than charged pions. There is some energy dependence to the charged particle reaction with the scintillator, but principally the strength of the signal is dependent upon the number of charged particles interacting with the detecting media [20]. It is evident that since a third of the energy goes to neutral π^0's and since a nuclear interaction is much less probable than an electromagnetic one per unit distance traversed, the fluctuations in hadron showers are much greater than EM showers and consequently the energy resolution is much worse in Hadron calorimeters.

The net result, for the reasons listed above, is that direct photons can be measured with a far better energy resolution than QCD jets can ever be measured because one of the legs (the photon) is directly identifiable and measurable in a purely electromagnetic fashion.

Chapter 3

The Collider Detector at Fermilab

3.1 Detector Coordinates and Subsystems

The Collider Detector at Fermilab (CDF) resides at B0, one of the interaction regions of the Tevatron accelerator at Fermi National Accelerator Laboratory. CDF is a nearly hermetic, general purpose detector designed to provide good lepton as well as jet identification (figure 3.1).

The central region of the CDF detector is a 2000-ton movable cylinder whose axis lies along the beamline when in place in the interaction region. The body of the cylinder consists of muon chambers outside of the central calorimeters which themselves are placed around a 1.4 Tesla superconducting solenoidal magnet used to bend charged particles for tracking. The endcaps of the cylinder are filled by the plug calorimeters which provide calorimetry coverage at angles shallower than the central region. There are also fixed in the collision hall a 3000-ton forward region, which contains calorimeters for angles even shallower than the plug region, large torroidal magnets and detectors for forward muon identification. The

29
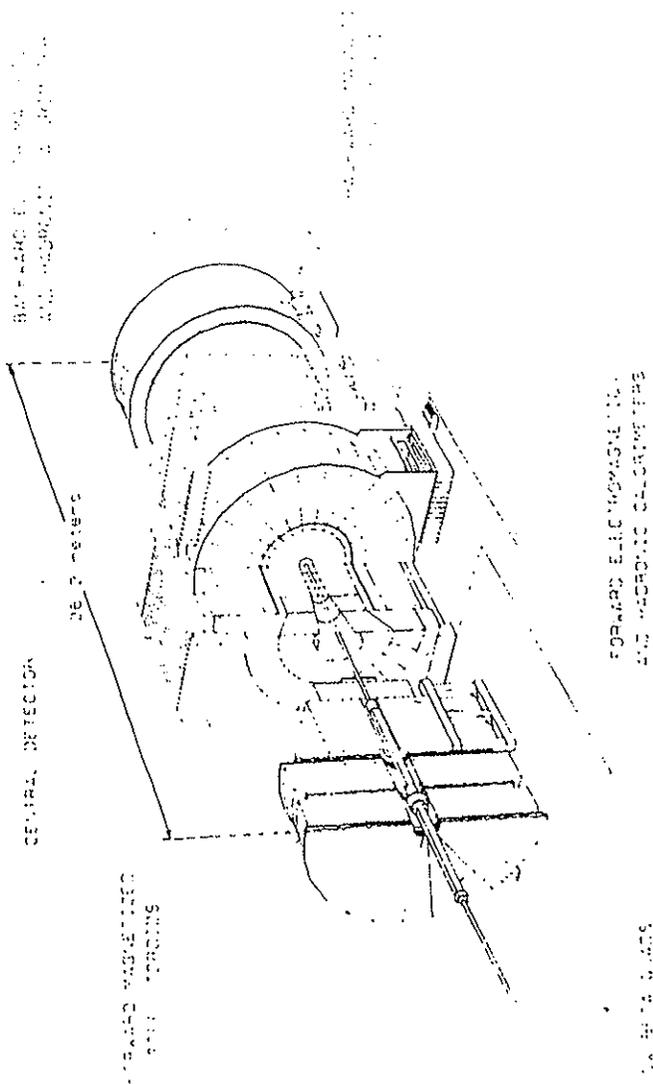
Figure 3.1: The Collider Detector at Fermilab (CDF).

subsystems of the detector are arranged with tracking closest to the beam line, then the electromagnetic, hadronic and finally the muon calorimeters. This is because the basic principle used in experimental measurement is the detection of charged particles. As mentioned in the previous section the calorimeters convert the energy of incoming particles into showers of charged and neutral particles either electromagnetically if they are photons or leptons or through nuclear interactions if they are hadrons. Tracking is done first to measure the 'primary' particles coming from the interaction and reducing the possibility of there being non-primaries from early showering to a minimum. The EM calorimeters are then placed in line with enough material to shower light leptons (electrons) and photons, but not enough to cause hadrons to shower, followed by the hadronic calorimeters with more material and finally the muon chambers with still more. For the purposes of this study the CDF detector consists of a central tracking chamber (CTC), a vertex time projection chamber (VTPC), central (CEM), plug (PEM) and forward (FEM) electromagnetic and central (CHA), plug (PHA) and forward (FHA) hadronic calorimeters, providing coverage for nearly 98% of the solid angle. The systems used in this analysis will be discussed in brief below. A full in depth description of the CDF Detector has been published elsewhere [21].

In CDF coordinates, the proton direction (east in Batavia coordinates) is taken to be +Z, up is +Y and south is +X. The detector covers a range in θ of $2° < \theta < 178°$. As mentioned in the previous chapter, the average particle density from the interactions is approximately flat in η so the CDF detector was constructed with projective tower geometry in η-ϕ space, the actual tower size varying by detector (figure 3.2).
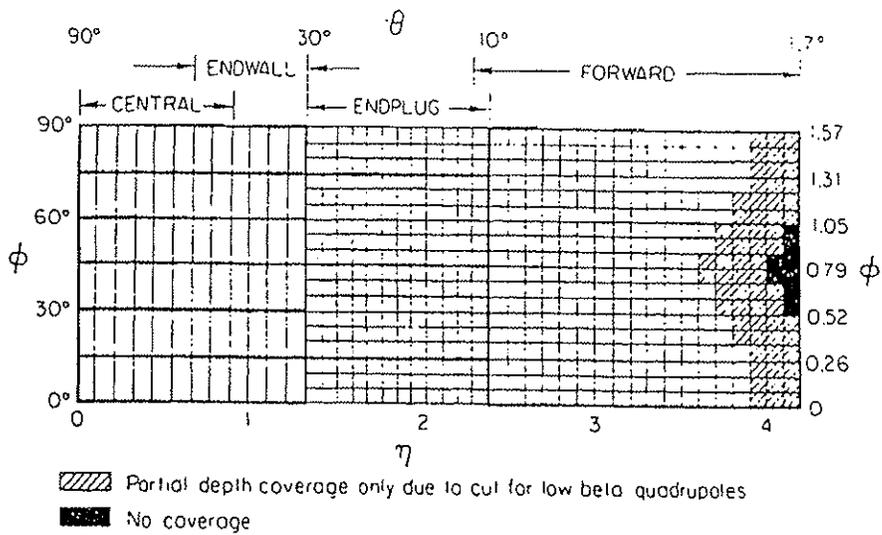
Figure 3.2: Calorimeter Tower Segmentation for an octant of the detector. Tower ($\eta \times \phi$) is 0.1x15° in the central and endwall areas of the detector and 0.1x5° in the gas calorimeters.

32

Angular coverage:	
Inner	$3.5° < \theta < 176.5°$
	$-3.5 < \eta < 3.5$
Outer	$8° < \theta < 172°$
	$-2.7 < \eta < 2.7$
Mechanical Parameters:	
Number of Modules	8
Module Length	35.3 cm
Module Spacing	35.94 cm
Inner Radius	7.0 cm
Outer Radius	21.0 cm
Octants/Module	16
Wire/Module	24
Pads/Module	24
Mag Field	1.5 Tesla
Drift Field	256 V/cm
Drift Length	15.25 cm
Drift Velocity	42 μm/ns
Gas	50/50 Ar/Ethane
Resolution:	
Spatial	200-500 μm
Track	6 mm(r-Z), 3 cm (ϕ)

Table 3.1: Vertex Time Projection Chamber (VTPC) Specifications

3.2 Tracking

In the 1988-1989 run the VTPC lay closest to the beam line of the CDF detector. The main purpose of the VTPC is to extract the Z position of the event interaction(s) over an angular range of $8° < \theta < 172°$.

The VTPC is a time projection chamber that measures the R-Z positions of single charged particles passing through its volume. The charged particles ionize the gas in the volume and the ionized electrons are then allowed to drift through the volume to sense wires that are lying perpendicular to Z and held at a potential (see figure 3.3). The wire positions determine radial position and the drift times deliver Z position. The resulting 'hit'

33

positions are then used to reconstruct charged particle tracks and are extrapolated back to the interaction area to determine a Z vertex position of the event (see figure 3.4). The resulting event Z vertex is used to correct the event angle θ. Relevant parameters of the VTPC are shown in Table 3.1.

The central tracking chamber CTC) is a large 1.3 meter radius cylindrical drift chamber surrounding the VTPC and in turn embedded within a 1.4 Tesla superconducting solenoidal coil with an axial field direction. The CTC is used to measure the paths of single charged particles in R-Z-ϕ over an angular range of $40^\circ < \theta < 140^\circ$. The CTC consists of 84 rows of axial sense wires grouped into 9 superlayers. The superlayers alternate 12 rows of pure axial wires and 6 rows with wires canted at 3° for a stereo effect to resolve the Z position (figure 3.5).

All the wire cells are inclined at a 45° angle (see figure 3.5) with respect to the radial direction from the beam axis to compensate for the Lorentz angle of the electron drift direction in an electric and magnetic field. Multiple rows within a superlayer are for redundancy in case of wire failure and to resolve corrupted or ambiguous data. The sense wire positions are used to determine the R position and the drift times are used to determine the ϕ position. The axial magnetic field bends the charged particle trajectories along ϕ preserving their Z position but allowing the measurement of the charged particle's momentum for particle identification. Relevant parameters for the CTC are listed in Table 3.2. The CTC was used mainly in this analysis to veto events with charged particle tracks pointing at the electromagnetic cluster.

34

SENSE WIRES
SENSE WIRE READ-OUT
CATHODE PADS
CENTER H.V. GRID
CARBON FIBER OCTOGON
RADIAL BOARD
CARBON FIBER OCTOGON
PAD READ-OUT
INNER FIELD CAGE
DRIFT
DRIFT
P.W.C. CATHODE GRID
OUTER FIELD CAGE
RESISTIVE DIVIDER

V.T.P.C. MODULES
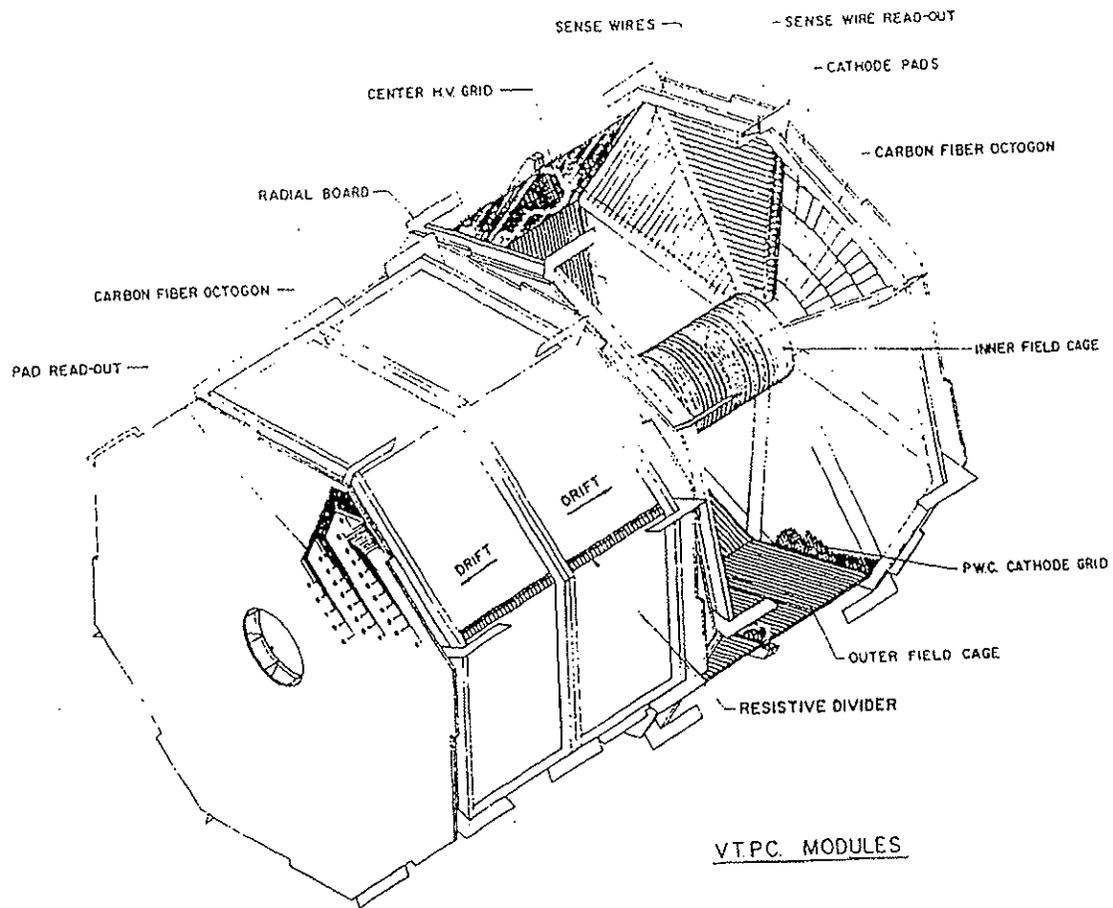
Figure 3.3: View of the Vertex Time Projection Chamber (VTPC).

35

a

F →

p̄bar ←
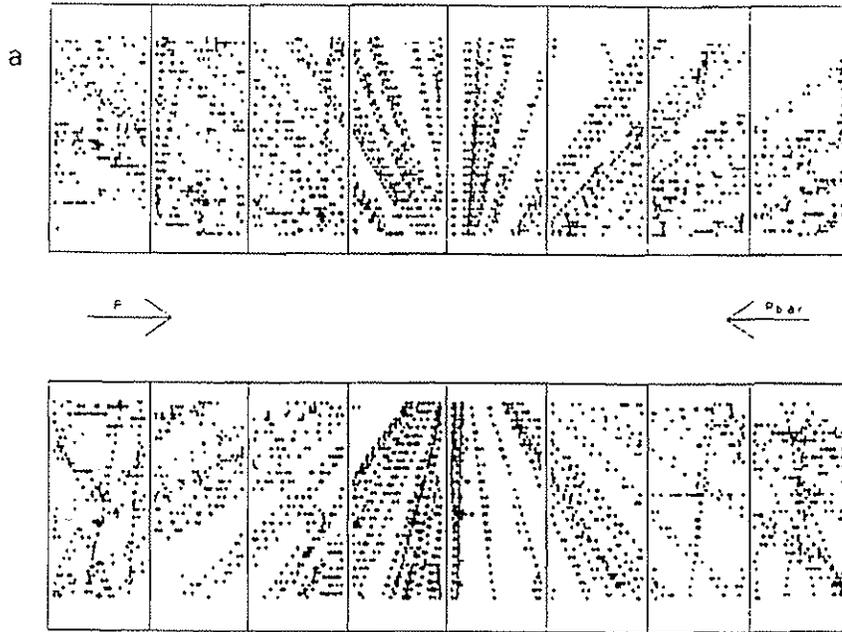
Figure 3.4: VTPC Hits for a High E_T Jet Event.

36
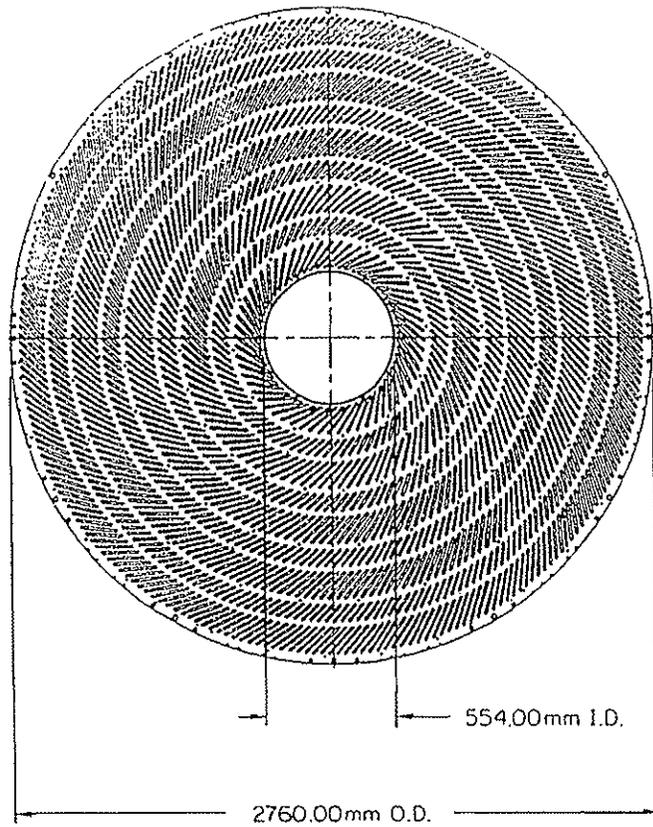
Figure 3.5: Endplate View of Central Tracking Chamber (CTC) Wires. Compare this to figures 1.2, 1.3 and hits and reconstructed tracks from the CTC.

37

Angular coverage:	
Inner	$15° < \theta < 165°$
	$-2.0 < \eta < 2.0$
Outer	$40° < \theta < 140°$
	$-1.0 < \eta < 1.0$
Mechanical Parameters:	
Number of Layers	84
Number of Superlayers	9
Layers/axial superlayer	12
Layers/stereo superlayer	6
Stereo angle	$\pm 3°$
Radius Inner	309 mm
Radius Outer	1320 mm
Mag Field	1.5 Tesla
Drift Field	1350 V/cm
Drift Length (Max)	40 mm
Gas	nominally 50/50 Ar/Ethane
Resolution:	
Spatial r-ϕ	$< 200 \ \mu$m/wire
Spatial Z	4 mm
Momentum	$\frac{\delta P_T}{P_T} = 0.0020 \times P_T$
Momentum (Beam Const)	$\frac{\delta P_T}{P_T} = 0.0011 \times P_T$

Table 3.2: Central Tracking Chamber (CTC) Specifications

3.3 Central Calorimeters

The central calorimeters form the barrel of the central cylinder and consist of 24-15° wedges on each side of the detector. The Wall Hadron calorimeters are placed outside of the barrel to complete hadronic coverage from the central and the plug regions. The single most important subsystem of the detector for this analysis is the central electromagnetic calorimeter (CEM). The limited range of the effective tracking (CTC only) restricted our identification of photons to the central region. All of the triggered events utilized the CEM which covers an angular range of $39° < \theta < 141°$. The CEM was designed as a hybrid (scintillator and gas) calorimeter in order to take advantage of the good energy resolution of scintillator and the finer positional segmentation possible with gas proportional wire chambers (PWC). The CEM consists of 31 layers of polystyrene scintillator interspersed with sheets of lead absorber segmented into towers 0.13 in η by 15° in ϕ allowing for positional determination of the energy flow. Light guides then take the signal to the phototubes for measurement after wave shifters converted the blue Cherenkov light to a frequency to which the phototubes were more sensitive (a pale green). Each scintillator layer itself consists of two layers, each half connected to a different phototube for redundant protection against a single faulty phototube. At 6 radiation lengths in depth into the lead-scintillator sandwich, the position of maximum shower development (shower max) for electrons, are placed the central strip/wire chambers (CES). The CES chambers are gas proportional wire chambers whose finer segmentation allow measurement of the electromagnetic shower profiles in both Z through its cathode strips and R-ϕ through its anode wires. The CES shower profiles are important in this analysis for the separation of signal and background and are discussed in

39

	Central EM	Central Had	EndWall Hadron
Angular ($\lvert \eta \rvert$):	0.0-1.1	0.0-0.9	0.7-1.3
Coverage (θ):	$39 - 141°$	$45 - 135°$	$30 - 45°$ and $135 - 160°$
Tower Size($\Delta\eta \times \Delta\phi$)	$0.11 \times 15°$	$0.11 \times 15°$	$0.11 \times 15°$
Mechanical Parameters:			
Number of Modules	48	48	48
Module Length(Z)	250 cm	250 cm	100 cm
Module width (ϕ)	45.5cm(@r=173cm)	133 cm	80 cm
Module depth (r)	34.5 cm		110 cm
Module Weight	900 Kg	1200 Kg	7000 Kg
Active Media:	SCSN-38	PMMA doped	PMMA doped
(Scintillator)	Polystyrene	Acrylic	Acrylic
Thickness	5.0 mm	1.0 cm	1.0 cm
Layers	21-31	32	15
Absorber:	Pb	Fe	Fe
Thickness	3.18 mm	2.5 cm	5.0 cm
Layers	20-30	32	15
Energy Resolution $\left(\frac{\sigma}{E(GeV)} \right)$	$\frac{13.5\%}{\sqrt{E}} + 1.7\%$	$\frac{80\%}{\sqrt{E}} + 3\%$	$\frac{80\%}{\sqrt{E}} + 3\%$

Table 3.3: Central and Endwall Calorimeter Specifications

greater detail in Chapter 5. The central (CHA) and endwall (WHA) hadronic calorimeters are placed behind the CEM in the same tower configuration (see figure 3.2) as the CEM. The CHA covered the angular region in $45° < \theta < 135°$ and the WHA from $30°$ to $45°$ and $135°$ to $150°$ in θ. The CHA consisted of 32 layers of iron and scintillator sandwiched together while the WHA consisted of 15 layers, but each layer was double the sampling thickness of the CHA. See Table 3.3 for relevant parameters of the CEM, CES, CHA and WHA and figure 3.6 for a schematic view of a wedge.

The CEM, CHA and WHA were all calibrated with test beam electrons and pions at various energies sent into a sample wedge. In the case of the CEM each wedge in the detector was measured in the test beam and a detailed response map of tower to tower corrections was constructed (see figure 3.7).

40
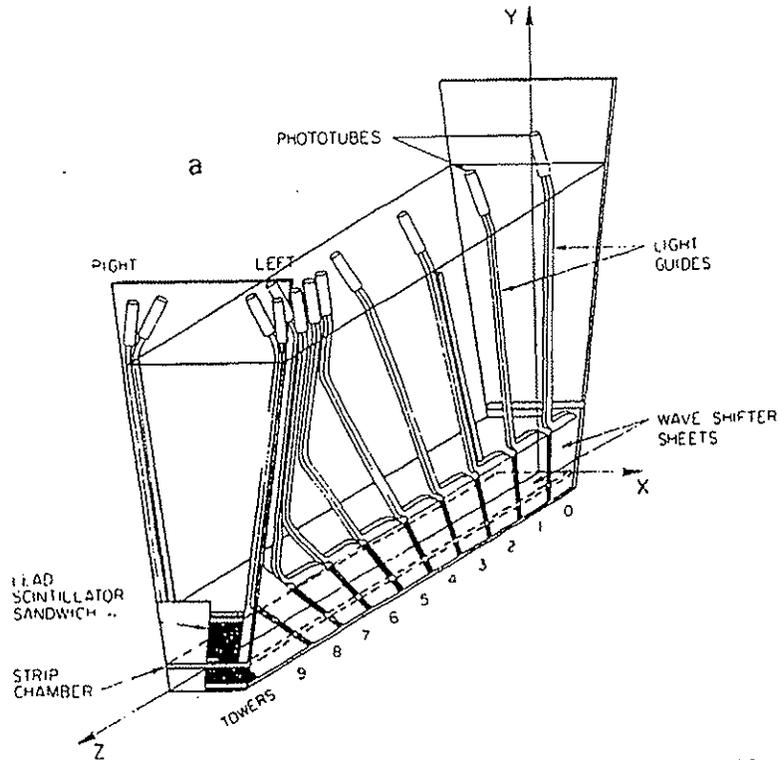
Figure 3.6: A Wedge of the CDF Central Calorimeter. Showing the segmentation into towers in η (along the beam direction z), projective geometry and the phototube layout for the CEM.

41
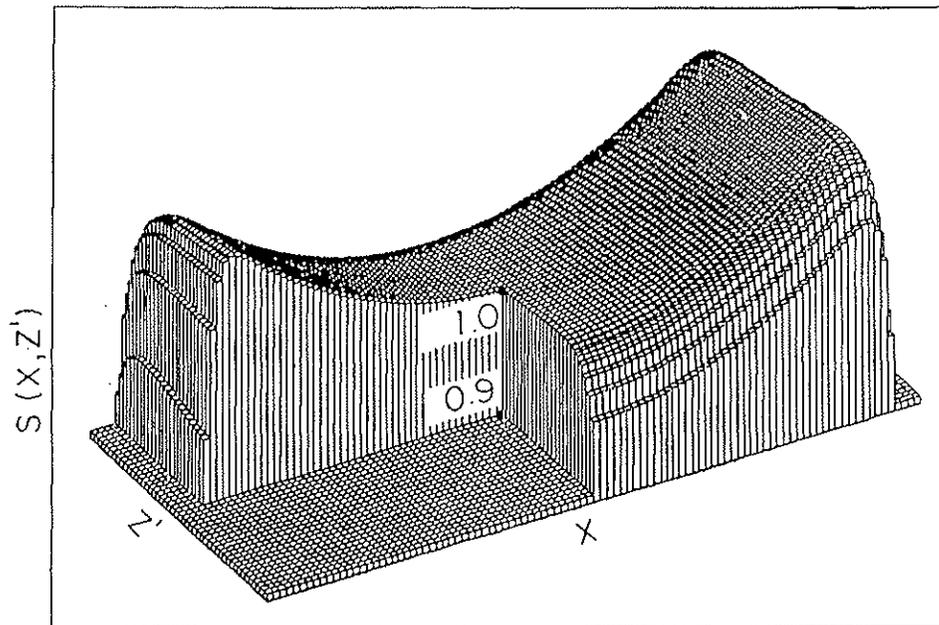
Figure 3.7: The CEM Tower Response Map shows the response of a single tower to an EM shower as a function of position over the face the tower. Each tower was mapped separately and was slightly different.

42

Additionally the variation of signal response over a single tower face was corrected using a measured response function and the position on the tower face determined by using the CES position. The calibration was maintained during the run by the use of *in situ* cesium sources that could be moved remotely in front of each tower face and by a system of flashers and green LED's that could check the operation of the wave-shifters and photo-tubes respectively. Tests showed that the calibration could be maintained to ~0.5%.

3.4   Plug and Forward Calorimeters

The plug and forward components of the CDF detector all utilize gas proportional wire chambers (PWC's) due to their relatively low cost and the ease of maintaining the projective tower geometry. The lack of low angle tracking in the 1988-1989 run prevented the identification of photons in plug and forward calorimeters so in this analysis they are used solely for the measurement of the recoiling jets. The gas calorimeters all used the same gas, nominally a 50/50 mixture of Ar/Ethane with a trace of alcohol to act as a quench. All of the gas calorimeters also take advantage of the relative ease of finer segmentation and used tower sizes of $5°$ in ϕ and 0.09 in η. The gas calorimeters are layed out in two halves on either side of the central calorimeters. (See figure 3.8)

The actual chamber stacks form a quadrant on one side in the PEM, FEM and FHA and a $30°$ slice in the PHA. The gas calorimeters are constructed with anode wires surrounded by tubes of resistive plastic in the plug (aluminum in the forward) that split the chambers into cells and copper cathode planes laminated to G-10 plastic that were segmented to maintain the projective tower geometry.

43
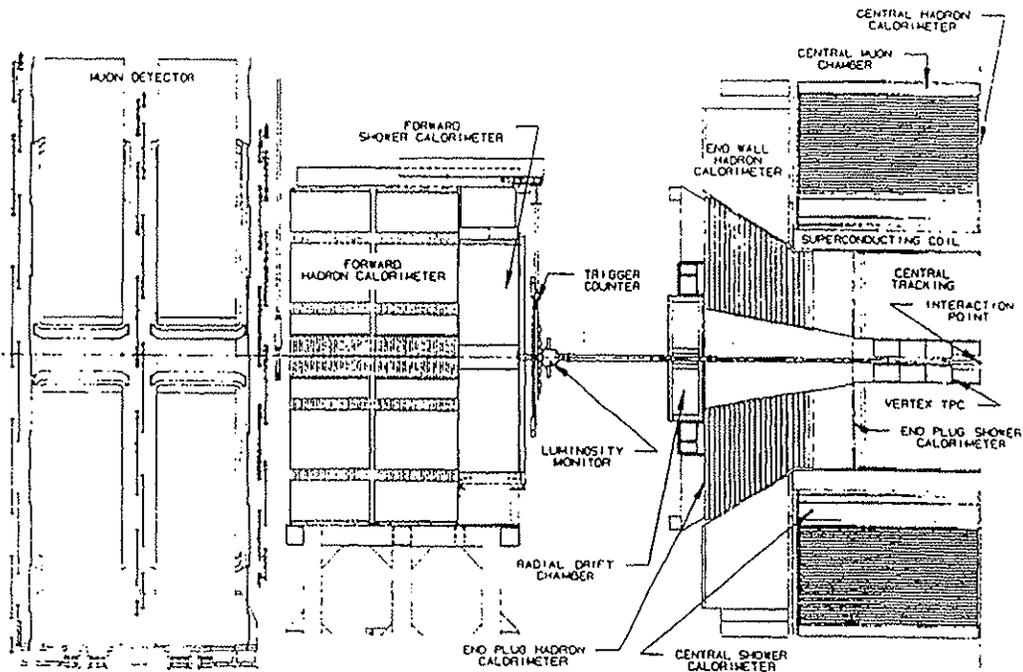
Figure 3.8: CDF Detector Side View (half). The plug fits inside the barrel of the central calorimeter as an endcap on each side. The forward calorimeters are fixed in the collision hall on either side (east-west).

44

The plug sections of the detector fill in the endcap on either side of the central barrel. The plug electromagnetic calorimeter (PEM) covers the angular region from 10° to 36° and 144° to 170° in θ. Each PEM plug (one on each side of the central) has four quadrants. Each quadrant, 90° wide in ϕ, consists of a stack of 34 layers of wire chambers interspersed with thin lead sheet absorbers. The plug hadronic calorimeter (PHA) covers the angular region from 10° to 30° and 150° to 170° in θ. Each PHA plug consists of 12-30° (in ϕ) sections; each section contains 20 layers of chambers sandwiched between 21 layers of steel.

The forward detectors are not placed in the movable cylindrical section of the detector but are fixed in position within the interaction region and are used to extend the coverage to even shallower angles than the plug region. The forward electromagnetic calorimeter covers the angular region from 2° to 10° and 170° to 178° degrees in θ. Each forward region contains four quadrants each consisting of 30 layers of proportional wire chambers and thin lead sheet absorbers. The forward hadronic calorimeter (FHA) covers the same angular region as the FEM and was also broken into the four quadrant stacks of chambers. The FHA has 27 layers of PWC's and steel absorbers. See Table 3.4 for the relevant parameters for the PEM, PHA, FEM and FHA.

Maintaining the calibration of the gas calorimeters was laborious due to the exact nature of signal gathering in PWC's. The gas calorimeters maintain a volume of an electrically neutral noble gas that ionizes with the passage of charged particles. The resulting ionizing electrons are accelerated through an electric field where they ionize more and more electrons that eventually are collected and measured as a charge on a capacitor after amplification. The charge collected is proportional to the initial energy of the original particles before the shower and is dependent upon the composition and density of the gas as well as the high

45

	Plug EM	Plug Had	Forward Em	Forward Had
Angular ($|\eta|$):	1.1-2.4	1.3-2.4	2.3-4.2	2.3-4.2
Coverage (θ):	$10 - 36°$ and	$10 - 30°$ and	$2 - 10°$ and	$2 - 10°$ and
	$144 - 170°$	$150 - 170°$	$170 - 178°$	$170 - 178°$
Tower Size($\Delta\eta \times \Delta\phi$)	$0.09\times5°$	$0.09\times5°$	$0.1\times5°$	$0.1\times5°$
Active Media:	Proportional Wire Chambers and Cathode Pads			
Gas	50/50 Ar/Ethane			
Alcohol Quench	Isopropyl	Ethyl	Isopropyl	Isopropyl
Voltage	1700 V	2120 V	1900 V	2100 V
Tube Size	7.0×7.0 mm	14×8.0 mm	10×7.0 mm	15×10 mm
Thickness	0.94 cm	1.0 cm	1.6 cm	2.5 cm
Number of Chambers	34	21	30	27
Absorber:	Pb	Fe	94%Pb,6%Sb	Fe
Thickness	2.7 mm	5.1 cm	4.8 mm	5.1 cm
Layers	33	20	30	27
Energy Resolution $\left(\frac{\sigma}{E(GeV)}\right)$	$\frac{28\%}{\sqrt{E}} + 2\%$	$\frac{130\%}{\sqrt{E}} + 4\%$	$\frac{25\%}{\sqrt{E}} + 2\%$	$\frac{130\%}{\sqrt{E}} + 4\%$

Table 3.4: Plug and Forward Calorimeter Specifications

voltage (HV) applied to the chambers. The calorimeters were monitored on line to ensure that the calorimeter response was roughly constant throughout the duration of the run. This was done by placing gas monitor tubes, which were tubes of various designs (denoted BRD, LBL and KEK for their places of origin), but basically small single cell proportional wire tubes, with a known source (Fe^{55}) mounted on them. The tubes were placed at various key positions and inline with the gas flowing to the wire chambers. Their source readings were then read continuously by an online program (GASDAQ) [22] in order to determine the current calorimeter response due to gas density changes. The data were recorded in the gas gain data base and also continuously displayed on a visual monitor. A special flag was sent to the Alarms and Limits program [23] if the response changed by more than 3% from some nominal gain (see figure 3.9). When the nominal gain changed by more than 5%, the run was paused and new calibration constants were downloaded to the system to

compensate for the changes in gas density.

The HV was calibrated before the run and monitored by a computerized readout system (GHV) and a constant gas mixture was maintained by measuring a sample of the gas before flow into the calorimeters at a controlled standard temperature and pressure with gas monitor tubes held at a constant voltage. If the gain of the tubes was not constant to a half percent then corrections were made to the gas mixture to compensate. In this fashion the resolution of the gas calorimeters was maintained roughly constant despite not being insulated from the outside weather. The absolute energy scale of the gas calorimeters was determined by use of dijet and γ-jet balancing which is described in more detail in Appendix C.
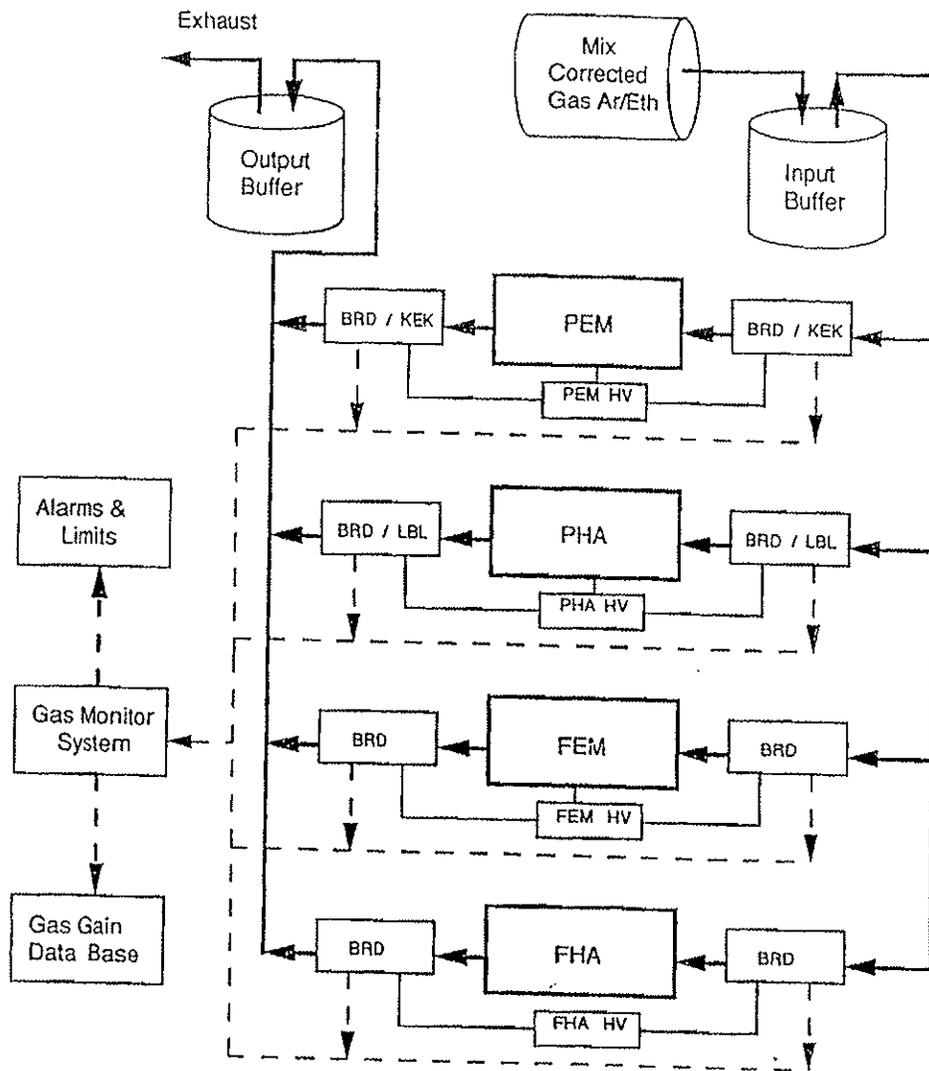
Figure 3.9: Schematic View of the Gas Calorimeter System. Carefully mixed Ar/Ethane (nominally 50/50) from the same source flowed to all the CDF calorimeters (heavy outline) through input and output monitor tubes placed inline with the gas flow. The tubes were readout by the gas monitor system and the data recorded into the gas gain data base. Heavy solid lines denote gas flow, thin lines the high voltage connections, and dashed lines the data flow from the monitor tubes.

48

Chapter 4

Data Acquisition and Event

Selection

4.1 Data Acquisition in the 1988-1989 Run

The 1988-1989 run of the Tevatron was enormously successful. The total integrated luminosity delivered to B0 was 8.5 pb^{-1} reaching a peak luminosity of 2×10^{-30}cm^{-2}sec^{-1}. CDF with a grand total of nearly 100,000 electronic channels could only be read out to tape at a rate of 1 or 2 Hz in the 1989 configuration. With beam crossings at a rate of 100,000 Hz at peak luminosity, an intricate multi level trigger system was employed to cut the event sample down to a manageable size and reduce 'dead' time in the detector. Each level of the trigger, except level 0, had different possible means of passage; for example, there were in level 1, a jet trigger, electron trigger, a dielectron trigger and a photon trigger, amoung others. Passage of any of the possible level 1 triggers constituted a level 1 pass. Each successive level required passage of at least one of the previous level triggers of the same type

(*e.g.* a level 2 photon pass implied a level 1 photon pass not a level 1 electron pass). Each level took progressively more time and a trigger failure at any level vetoed the event and allowed the trigger to immediately reset and prepare for the next event with as little loss of luminosity as possible. The first three levels of the trigger (0-2) made decisions based on partial detector information available to them and only after a level 2 pass was the entire detector read out. The last trigger, level 3 was intended to closely mimic selection cuts from the various physics groups to rid oneself of events that would be discarded offline in any case and only after a successful level 3 pass was an event written to tape. As was explained in Chapter 2 most of the interactions are 'soft' events with very little momentum transfer not applicable to our current theories and were not of particular interest. For this reason most of the mid-level triggers rely on the presence of suitable energy transverse (E_T) to the beam direction. Even the events that were of interest occurred at such disproportionate rates that it was necessary to prescale many triggers to prevent all recorded events from being of one particular type. A small fraction of the 'soft' events, ('Minimum Bias') were kept for further study and were very heavily prescaled.[1] What follows is a brief description of the triggers used in this study and the clustering algorithms used to group together energy from an event. See figure4.1 for a schematic of the data acquisition (DAQ) pipeline and Table 4.1 for a summary of direct photon trigger cuts by level.

---

[1] A trigger with a prescale of 1000 means that only 1 of 1000 events passing that trigger is kept.
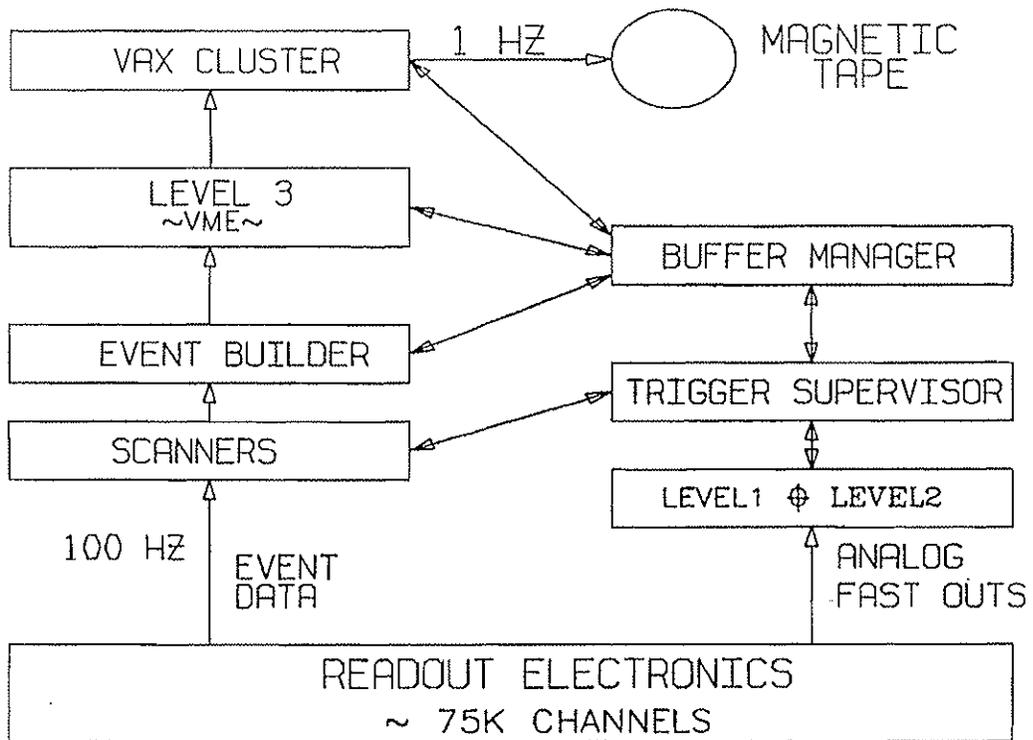
Figure 4.1: Schematic View of the Data Acquisition System [24].

51

4.2   The Photon Triggers

A direct photon event should leave a very distinctive signal in the detector. Since the direct photon is produced in a distinct hard process as opposed to emergence from a jet or *via* bremstrahlung radiation from a charged particle, the photon should be isolated from other energetic activity. The signature for a direct photon then becomes an isolated primarily EM energy cluster without a track; all photon cuts were designed with this signature in mind. The exact cuts utilized are elaborated upon in the next chapter. The complexity of the tracking algorithms prevented full three dimensional online tracking from being performed so no track cuts were placed on events online. For the purposes of this study there were only two photon triggers. One was an unprescaled high $P_T > 23$ GeV (P23) photon trigger online for 3.2 pb^{-1} of luminosity and the other was a prescaled lower $P_T > 10$ GeV trigger (P10) with an effective luminosity of 74 nb^{-1}. The difference in P_T thresholds between the two triggers occurred in level 2. The results of the P23 data are reported on in the body of the thesis; the P10 data are reported on in Appendix D. In actuality there were four photon triggers as each of the two aforementioned triggers had two possible level 3 passes which are discussed in greater detail in the section 4.4, but only one level 3 pass was used in this analysis.

4.2.1   Trigger Level 0

The first level of the trigger system was level 0 which was meant to ensure that there was some minimum inelastic activity in the event as well as actual beam in the collision area so as not to include data from non-accounted sources (*e.g.* cosmic rays). A level 0 trigger

52

required coincidence from a pair of beam-beam counters, which consisted of scintillator placed on opposite sides of the beam pipe at very shallow angles, to be within 100 ns of a known beam coincidence in the interaction region. The beam-beam counters were the main source of luminosity monitoring and were used to trigger minimum bias events. The decision making time of the level 0 trigger was less than the 4.5 μsec between beam crossings so there was no deadtime incurred from this trigger.

4.2.2 Trigger Level 1

The level 1 trigger used gross detector topologies to identify events of interest. After a level 0 pass analog signals were read from the calorimeters with the RABBIT based front end electronics system [26] and passed to the FASTBUS analog crates [27] via specially designed cable fastouts. Here the calorimeter data was processed with hardware boards and the calorimeter energies summed into towers 0.2 in η by 15° in ϕ. The level 1 photon trigger required that there was at least one central tower with 4.0 GeV E_T and the total EM E_T was greater than 6.0 GeV. For this purpose E_T was defined to be the energy of the tower times $\sin\theta$ of the tower where θ was defined from the center of the detector (Z=0) to tower center. Pass/reject of the event in level 1 was based on comparison of the event topology to that of a lookup table. The level 1 decision was made in 7 μsec which meant that on average one beam crossing per level 1 decision was lost, which represented about 15% deadtime. The output of level 1 into level 2 was on the order of 1 or 2 KHz.

53

4.2.3 Trigger Level 2

Each level 2 trigger was designed by the various physics groups interested in specific physics processes. The requirements of level 2 were to reduce the selected output to a rate of about 100 Hz as 10 msec was the time required for full detector readout. A slightly more sophisticated and more time consuming hardware clustering algorithm was performed in level 2 to help further identify the topologies of interest before making the decision for full detector readout. Clusters are found by searching for seed towers which are required to have total E_T EM plus hadronic 4.0 GeV, E_T defined as in level 1. Four nearest neighbors are then included in the cluster if they have $E_T > 3.6$ GeV. This continues until the cluster can no longer be extended. The photon level 2 triggers required that there be an EM cluster with $\frac{E_T^{EM+Had}}{E_T^{EM}} < 1.125$ (highly electromagnetic) and E_T 10 GeV in the low threshold trigger and 23 GeV in the high threshold trigger.

4.2.4 Trigger Level 3

The level 3 trigger was the only trigger to have all detector information available to it for its decision making. If the event passed level 2 the MX scanners through FASTBUS then polled the RABBIT electronics to collect the signals from the calorimeters that were digitized while the level 1 and 2 decision making was taking place. Concurrently SSP scanners polled the tracking detectors. The data were then all collected in the Event Builder (EVB) where it was assembled, buffered and formatted for use by the level 3 processors. A farm of 60 Motorola 68020 processors were each sent a formatted event where offline clustering and calculations could be performed and events selected accordingly. Corrections to the data were performed here as well for cable and detector noise and bad events were discarded [28].

54

The level 3 clustering and cuts are discussed in detail below in the section on online cuts. It required about 20 seconds for each event to be fully processed by a node but the rejection rate was adequate to reduce the output rate from level 3 to the 1-2 Hz level needed for writing to tape.

4.3 Direct Photons and Background

This section will discuss how direct photon candidates are selected from the data. It is important to realize that it is strictly impossible to remove all the background from the DP signal. This is because ultimately the background are events with photons, but not originating from the direct photon process. The strategy is to apply cuts that increase the signal to background ratio as much as possible and then use a statistical method to perform the final subtraction. The actual subtraction method will be discussed in the next chapter.

Direct photons have a very distinct signature in the detector. As previously mentioned DP's appear as isolated electromagnetic clusters in the calorimeter with no tracks pointing at the cluster. Photons look like trackless electrons in the CDF detector. Figure 4.2 shows schematically the signatures of the signal and the background in the detector.

Clusters that deposit all or nearly all of their energy in the EM calorimeters are almost certainly electrons or photons. Charged pions can shower early but it is not very likely; to mimic a photon it must shower early and have lost its track, the probability of which is less than 1 in 10^4 [29]. The source of charged pions would have to be rare fragmentation which is the same source as the neutral pion background. The total neutral background cross section is roughly equal to the signal before the stringent isolation cuts (after the cone=0.7
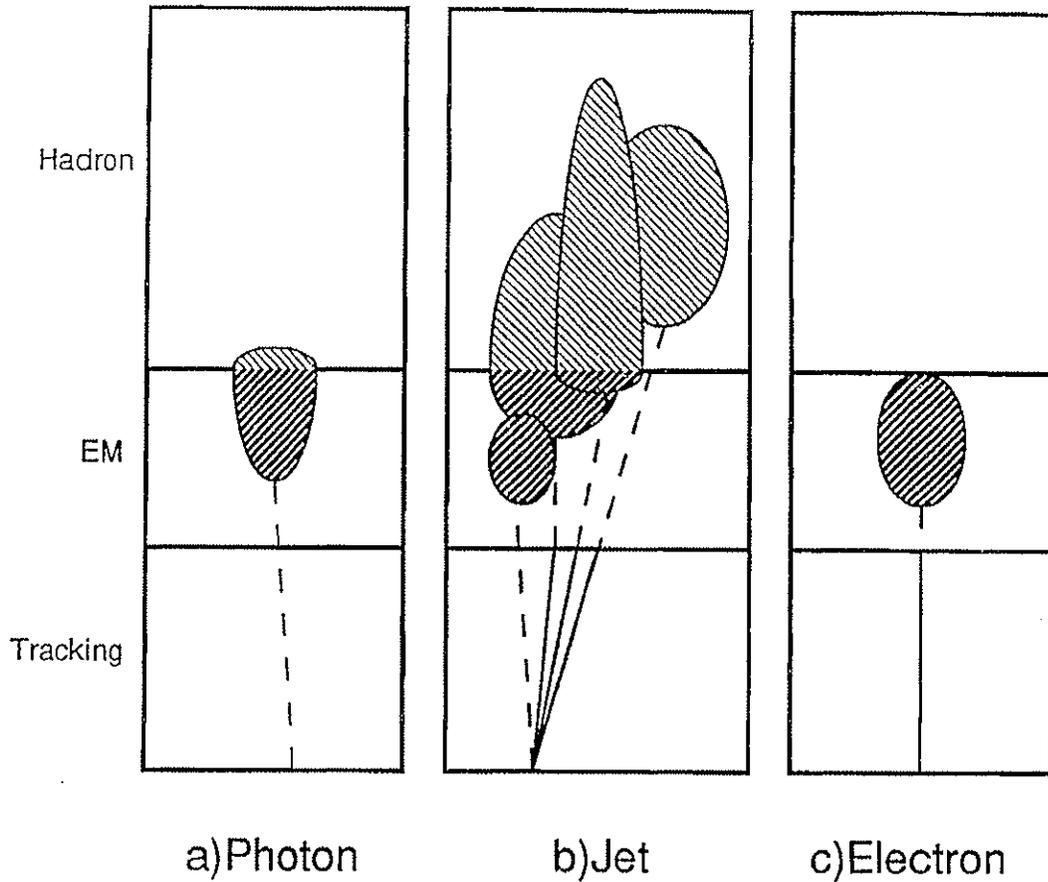
Figure 4.2: Schematic View of Typical Event Topologies. (a) Signature of a photon candidate event, (b) is a jet event, (c) is a electron event. Dark hashes represent energy deposited in EM calorimeters, light hashes in the hadronic calorimeters. The solid lines represent tracks from charged particles left in tracking chambers, dashes the extrapolated tracks. The small amount of hadronic energy in the photon event represents leakage from the EM calorimeters, which was on the 1-2% level for EM events.

isolation) so the total isolated charged pion cross section is roughly twice the signal cross section and therefore the isolated charged pion background would have to be less than 1 in 500th of the signal, which is completely negligible (three or four events in the sample). The CTC is very efficient in identifying charged particle tracks and their directions (eff measured to be 96%) [30]. The only likely source of electrons are Drell-Yan ($q\bar{q} \rightarrow e^+e^-$) pairs or rare fragmentations but both cases mean that one electron must be lost and the other's track must be lost. The only likely other possible source of isolated primary electrons are from W and Z decays and the former should have a large missing transverse energy ($\not{E}_T$) while the latter should have a pair of unlike sign electrons. We know from simulation of Z decays that less than 2% of electrons can be lost in the detector [30]; this coupled with the track finding efficiency implies that there is less than 0.1% chance of a Drell-Yan or Z event to resemble a direct photon event. The missing E_T significance cut (see below) excludes 90% of all W events [31] and this coupled with the track finding efficiency implies that there is only a 0.4% chance that a W event could resemble a photon event. Since all these production cross sections are lower than DP's [30] [24] ($\frac{\sigma(W)}{\sigma(\gamma)} =\sim 0.5$, $\frac{\sigma(Z)}{\sigma(\gamma)} =\sim 0.05$, $\frac{\sigma(D-Y)}{\sigma(\gamma)} =\sim 0.1$), the probability of a photon candidate really being a misidentified electron is less than 0.1% (less than 2 events in the sample). Therefore it is not worth considering non-neutral background any further.

The only other possible background for direct photons are photons from other sources such as from bremstrahlung radiation or decaying neutral particles. Photons emerging as bremstrahlung radiation are highly collinear with their charged particle source. The source of possible neutral particles is fragmentation of a QCD jet and therefore in both cases other energetic particles should be near the photon candidate. Demanding that the photons are

Meson	Mass (MeV)	Decay Channel	Branching Ratio (%)
π^0	134.97	$\rightarrow 2\gamma$	98.8*
		$\rightarrow \gamma\, e^+ e^-$	1.2
η	548.8	$\rightarrow 2\gamma$	38.9*
		$\rightarrow 3\pi^0$	31.9*
		$\rightarrow \pi^+\pi^-\pi^0$	23.6
		$\rightarrow \pi^+\pi^-\gamma$	4.9
		$\rightarrow e^+ e^-\gamma$	0.5
		$\rightarrow \pi^0 2\gamma$	< 0.1
		others	0.1
K^0_s	497.67	$\rightarrow \pi^+\pi^-$	68.6
		$\rightarrow 2\pi^0$	31.4*

Table 4.1: Background: Neutral Meson Decay Modes (1990 PDG Booklet).
* Indicates Dominant DP Background

isolated (requiring little or no excess energy around the candidate cluster) removes most of the bremstrahlung and QCD background.

The major source of background for DP events is what is left, which are jets that fragment into single isolated neutral pseudoscalar mesons with most of the jet momentum, that themselves decay into two or more photons. This is of course a rare event for jets but the jet production cross section is about four orders of magnitude higher [32] [33] than it is for direct photons so their production probability is roughly equal. The most probable neutral backgrounds are in descending likelyhood, π^0's, η's and K^0_s 's. The possible neutral meson and their decay modes are listed in Table 4.1.

This poses an interesting problem because while there have been studies and models of jet fragmentation [34], fragmentation into a single isolated neutral particle is way down on the tail of the probability distribution and is certainly not modeled correctly. Therefore predicting the actual background rate from Monte Carlo is not feasible and it must be measured from the data. If the momentum of the neutral is low then it is likely that the

58

multiple photons will be separately clustered and can be distinguished accordingly and the candidate photon clusters will fail the isolation cuts. However, if the momentum is high enough, depending on the exact decay axis relative to the boost direction, the photons will merge into a single tower and will look outwardly like a single photon in the CEM (figure 4.3). A tower size in the CEM is roughly 20 cm at $\eta = 0.0$ which means that in the worst case, when the boost is perpendicular to the decay axis, the two photons from a π^0 will be within the same tower with a $P_T = 1.0$ GeV. The CES chambers, imbedded at shower max (184 cm from the origin) within the CEM, have a finer resolution than the CEM, which permits the measurement of EM shower profiles in Z with the strips (cathode pads) and along X with the anode wires.

The CES resolution is $\sim$ 3mm at $\eta = 0.0$ which implies measurable separation of a pair of photons from a decaying π^0 up to $\sim$ 55 GeV. In practice the real separable resolution is somewhat less, partly due to the presence of asymmetric decays where the particle momentum is along the decay axis of the neutral, so it appears in the lab frame as though one of the decay photons has nearly all the energy and the other tends to be lost. The photon shower profile along 11-channels (strip and wire), centered around the maximum pulse, is compared to sample electron profiles taken from a test beam and a χ^2 test is performed over the 11-channels. Shower profiles from single photons will very closely match the sample profile and have a low χ^2 while two or more photon events will not, on average, fit as well and will give a high χ^2. A statistical comparison of signal and background χ^2's is performed offline on the data to determine the level of background contamination (see Chapter 5). Keeping the above in mind, it is evident why the following cuts are used.

59
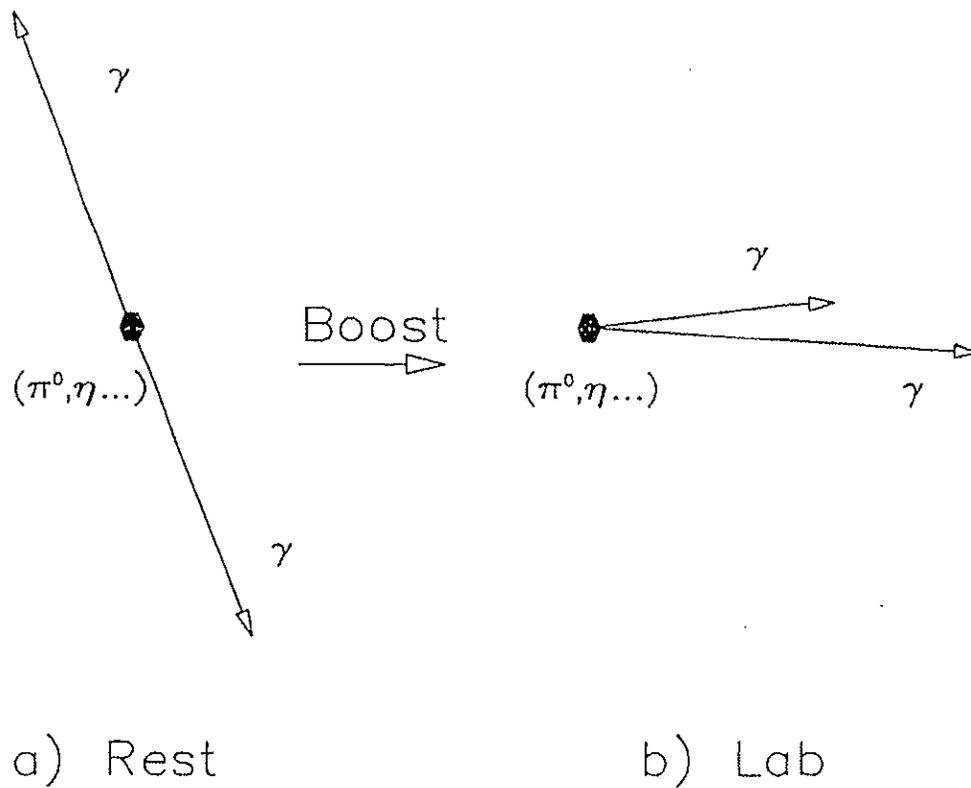
Figure 4.3: Decay of a Neutral Meson into Two Photons. (a) In the rest system of the meson the photons decay back-to-back, but in (b) the lab system when the meson is boosted with sufficient momentum p, the decaying photons can merge within a single tower of the CEM or within the possible resolution of the CES. This occurs at roughly ~ 1 and ~ 55 GeV respectively.

4.4 Online Cuts

Implicit cuts were made in level 2 on the threshold P_T's of the photons of 10 and 23 GeV for the two triggers and for Had/EM to ensure that the event had a highly electromagnetic cluster in the calorimeters (Cut was $\frac{E_T^{Had+EM}}{E_T^{EM}} < 1.125$).

The 1988-1989 experimental run began with no level 3 trigger installed. However due to the increase in luminosity of the Tevatron, level 3 cuts, which required full detector readout, had to be performed online to prevent substantial deadtime due to the backup at writing to tape. Some level 3 cuts were essentially noise cleanup, used to discard poor events, and were discussed in the previous chapter, but the physics cuts, used to identify good photon candidates, will be discussed here even though they were technically performed in the online trigger.

Level 3 clustering used a more sophisticated algorithm than level 2 clustering. The algorithm for EM clusters (photons and electrons) was slightly different than for jets due to the difference in their expected sizes.

4.4.1 Photon Clustering

EM clustering was designed to locate all the energy that came from a single photon or electron shower. Level 3 EM clustering searched for possible seed towers from a list of towers with $E_T > 0.3$ GeV and added the two adjacent towers in η if their $E_T > 0.1$ GeV and less than the seed tower. If the adjacent tower has more E_T than the seed tower, then it became the seed tower and the process was repeated. EM clusters should be spatially about the size of a single tower in the central, so allowing for the exact position of the shower

61

center within the tower, two or at most three towers should contain a single EM shower. The cluster was contained to be one tower width in ϕ because the ϕ tower segmentation is from central wedge to wedge and there was sufficient structural material in the wedge walls to prevent EM showers from crossing the wedge boundaries. The EM clusters were then saved only if the total $E_T > 5$ GeV. Here EM clustering E_T was defined to be the sum of each individual tower E_T in the cluster where $E_T = E_{Tot} \sin\theta$ where θ was the angle drawn to tower center and corrected in z by the event vertex and E_{Tot} is the total energy in the tower.

4.4.2 Jet Clustering

The recoiling Jets were clustered using the Jet Clustering algorithm which differed some from the EM clustering algorithm due to the expected size of the QCD jets. The Jet clustering was designed to gather together the energy from all the individual particles that presumably came from the fragmentation of the particle in order to determine the total energy of the initial parton [35]. The Jet Clustering algorithm again began by searching for seed towers, here with $E_T > 0.2$ GeV. A cone in $\eta - \phi$ space of radius r=0.7 ($\sqrt{\Delta\eta + \Delta\phi}$) was drawn around the center of the seed tower and all towers inside of the cone were added to the cluster. Towers in the gas calorimeters were summed together over ϕ to correspond to the same tower size as the central. The centroid of this cluster was then calculated considering the E_T of each tower weighted by the tower center and a new cone r=0.7 was drawn and all the included towers E_T's summed up. The process was then iterated until the list of towers remained stable. Special care was taken to handle possible overlapping jets and other pathological topologies that could lead to nonconvergence of the algorithm [28].

62

It was determined through various MC and detector simulation studies [35] that while the jet algorithm could reliably find jets with an uncorrected P_T as low as 5 GeV, it also could cluster 'false jets' that came from underlying event or spurious tower energies. Therefore it was necessary to require a candidate event to have a jet with some minimum P_T in order to ensure that angle between the photon and the recoiling jet was meaningful.

4.4.3 Online Level 3 Cuts

The most important of the level 3 cuts was the isolation cut which was used to reject photons from bremstrahlung radiation and other QCD background. The cut was performed by drawing an imaginary cone r=0.7 (η-ϕ) space, about the centroid of the photon cluster and comparing the total energy (EM+Had) to the energy within the cluster. If there was too much non-clustered energy within the cone the event was rejected. The actual cut used online was $\frac{E_T^{cone=0.7} - E_T^{EMclus}}{E_T^{EMclus}} < 0.15$.

There also was a loose χ^2 cut performed on the data to ensure that the strip and wire shower profiles were consistent with those from testbeam electrons. The online cut was set to $\chi^2 < 20$ which rejected a substantial amount of the background but permitted enough background in order to allow the statistical subtraction to be performed.

4.5   Offline Corrections and Cuts

The most basic cut that must be performed offline is the track cut. The tracking code is the most intricate of all of the reconstruction codes and, in order to use all the best information available to assemble hits and timing as well as vertex information, it takes more CPU time per event than could be allotted in level 3. The track cut vetoed any event that had

a full 3-D track reconstruction pointed at the same tower as the EM cluster no matter what the P_T of the track was. This cut was to eliminate electron events but it also was effectively a tracked particle isolation cut to eliminate possible low energy charged pions that could be nearby from a jet fragmentation and to eliminate photons that had emerged as bremstrahlung radiation from an electron.

Before the data were reduced offline, the data were processed to correct for known energy losses in the detector due to cracks and known non-linear response of the detector. Corrections were made to the photon P_T both on a tower to tower basis and based on the position of the event over the tower face. The tower to tower correction was performed with a CEM response map measured from the data using Z-decays and E/P (energy to momentum) measurements. The tower to tower correction was based on the measured CES position of the event was obtained from TB electrons where the beam was focused on different positions within a single tower [36]. The photon candidate P_T's were also recalculated using the strip position and the actual event vertex to calculate $\sin \theta$ rather than the centroid cluster position, and assuming that the event occurred in the center of the detector. Most electromagnetic clusters consisted of only a single tower so the maximum deviation in $\sin \theta$ from strip position is the difference in angle between tower center and the outside edge. This effect is largest at tower 9 (the tower with shallowest angle) which corresponds to a maximum correction of 1 GeV in P_T for a 30 GeV photon. The correction for event vertex could be quite large as vertices with z positions up to 50 cm away from detector center were used.

Corrections to the jet P_T were made with the routine QDJSCO [35] based on losses from parts of the jets in detector η cracks and to detector nonlinearities. QDJSCO scales

64

jet energies only and does not presume to change their positions. Since CM energies are determined from soley the photon and jet positions and photon P_T, jet energy resolution is only important for the minimum jet P_T cut and perhaps to second order in jet position if two or more jets are present. The minimum jet P_T cut discussed above was placed on the P_T of lead Jet to be greater than 10 GeV after QDJSCO corrections.

Other cuts were performed on the events in an attempt to further eliminate QCD background. Offline CES clustering over 11 strips and wires was also performed after corrections were made to their energies and cuts applied to ensure matching energies in both profiles (strips and wires). Offline the cone isolation cut was stiffened to be a fixed energy cut of 2.0 GeV within the cone of r=0.7, that is, it was required there be no more than 2.0 GeV of unclustered energy (electromagnetic only) within the cone of r=0.7. This is a much more restrictive cut than the 15% cut (15% of 30 GeV is 4.5 GeV) and even though it costs us some signal, it greatly enhances the signal to background ratio which greatly reduces the statistical errors. For the purposes of measuring the unclustered energy, the hadronic energy in the tower(s) directly behind the EM cluster was subtracted from the total. This is because there was on average 1-2% leakage of the EM energy into the hadronic calorimeters which is significant (0.5 GeV) on the scale of the 2.0 GeV cut. A cut was also made on second strip cluster energies within the tower to help eliminate more neutral background. No events were allowed with a second strip cluster >1.0 GeV of energy [37].

The other basic cuts applied offline were fiducial cuts designed to eliminate events that occurred in dead spots in the detector and cosmic rays. Cosmic ray events that missed the tracking chambers and the hadronic calorimeters and might mimic a direct photon signal. These events would typically have no balancing jet and therefore have a large transverse

65

energy imbalance in the calorimeters. The cosmic ray veto was performed with a cut on the significance of the transverse energy imbalance in the detector. Missing transverse energy ($\not{E}_T$) is defined to be the net E_T, $\not{E}_T = \sum(E\sin\theta)$. Missing E_T Significance (MEtSig) is defined to be $\frac{\not{E}_T}{\sqrt{\sum E_T}}$. If MEtSig=1, the events have $\not{E}_T$ significant to a standard deviation; the cut was placed at 3 (three standard deviations). For low P_T events this cut is not very effective at all, but requiring a minimum $P_T >10$ GeV for a recoiling jet all but eliminates this type of cosmic ray background. The final cuts were fiducial cuts made to ensure that the data used were all in good parts of the detector. The cuts were made based on the photon candidate CES positions in both Z and X to keep away from the wedge boundaries. All jets used in the study were also required to be in the opposite hemisphere from the photon candidate cluster in ϕ. This was meant to reduce the possibility of erroneously calculating $\cos\theta^*$ between a photon and a phantom jet cluster (from underlying event). There was also a cut on the extrapolated Z Vertex position to ensure that the interaction occurred well centered in the detector. This was primarily to ensure that there was flat acceptance in the event η of the photon candidate. A summary of all the cuts used to identify good candidates can be seen in Table 4.2.

4.6   Direct Photon Data

As mentioned in the previous chapter there were two photon triggers used in this study, an unprescaled high $P_T > 23$ trigger (P23) an a prescaled low $P_T > 10$ (P10) trigger. Each of these triggers had two possible level 3 passes; one (LSHR) had all of the level 3 cuts used by the Electron group to identify good electrons. These cuts included a loose isolation cut

Variable	Cut	Where Applied
P_T	22 GeV	Offline
$\dfrac{E_T^{Had+EM}}{E_T^{EM}}$	<1.125	Level 2
Isolation(cone=0.7)	<0.15	Level 3
χ^2_{ave}	<20	Level 3
# 3D tracks	<1	Offline
P_T Lead Jet	>10 GeV	Offline
E_T 2nd CES Clus	<1.0 GeV	Offline
MEtSig	<3.0	Offline
|ZVert| Pos	<50.0 cm	Offline
|StripX| Pos	<17.5 cm	Offline
StripZ Pos	217.0> StripZ >14.0 cm	Offline

Table 4.2: Cuts Required for Good Direct Photon Candidates

(isolation (cone r= 0.4)< 0.15), a cut on lateral tower energy sharing (LSHR) and border tower energy. It was determined from study that this trigger slightly biased the χ^2's of the passed events, so it was not used. All events quoted in this study passed the other level 3 trigger (NOLSHR) which applied directly the tight isolation cut (cone r=0.7) and not the adjacent tower energy cuts. Henceforth all references to P10 and P23 triggers will implicitly imply passing the NOLSHR level 3 trigger.

4.6.1 Trigger Efficiency

The imperfect resolution of the calorimeters results in the triggers having an effective threshold somewhat higher than the value set in level 2. This is caused by the corrections to the energy and position of the photon candidate that are made offline which slightly change the P_T of each event. In short, the values of the threshold variables used to select the events in the trigger are not the best measurements ultimately available. Therefore an event with a photon originally clustered below the level 2 threshold in P_T may have been discarded

before it could be corrected to its proper place where ideally it would have been saved. Conversely events that passed the trigger may ultimately be found to have a P_T that is below the threshold. It is a simple matter to determine where this real effective threshold is for the P23 sample, since it was unprescaled, by looking at a lower threshold trigger, for example the P10 sample, and checking the number of times a P23 trigger is found as a function of P_T. However the P10 sample was very heavily prescaled; therefore the statistics around the P23 trigger threshold were not as great as desired in the P10 sample thus we chose to use the unprescaled 12 GeV electron trigger (E12) as well. As mentioned previously, photon and electron shower development are exactly the same except for the one radiation length delay it takes for the average photon to convert to two electrons. Therefore as long as the photon and electron showers are fully contained within the EM calorimeters, clustering and trigger efficiency should be identical. The lack of an online track cut meant that isolated electrons were also triggered in the photon sample and therefore the P23 trigger efficiency could be determined using good electrons from the E12 sample, taking care to apply the same fiducial and isolation cuts on the electrons as were used on photons. The trigger efficiency as determined from the P10 and E12 data were completely consistent and were therefore combined. The P23 trigger efficiency was determined from the E12 and P10 triggers [38] and the P23 trigger was found to be 100% efficient at 35 GeV and 95% efficient at 28 GeV. In figure 4.4 the fraction of E12 electron and P10 photon candidates also passing the P23 trigger are shown. All photon events in the figure passed fiducial cuts and a cone r=0.7 15isolation cut.

The data were fit to a curve of the form $(A + B \exp C(D - X))^{-1}$ which is essentially a $(1 + \sinh)$ function. The fit parameters for the curve were A=1.0156 ± 0.0488, B=1.0482 ±

68
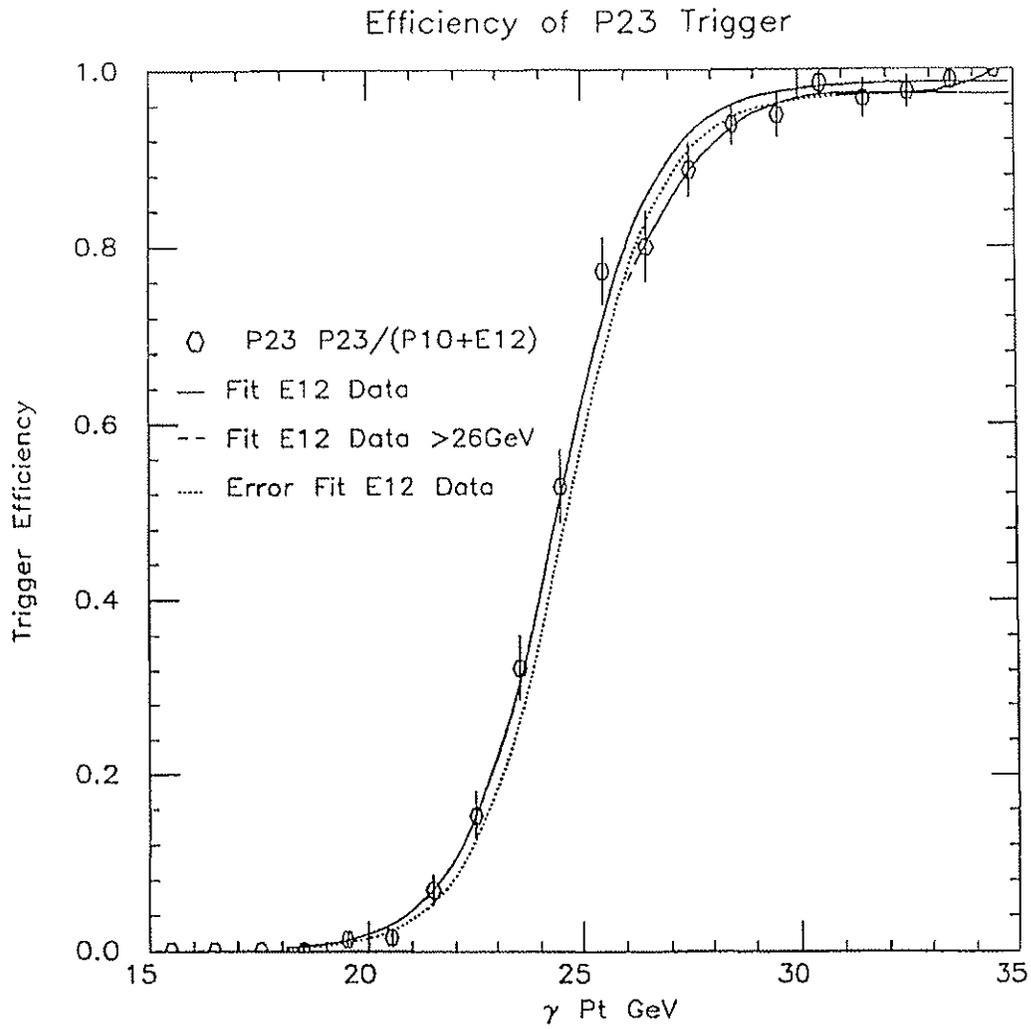
Figure 4.4: Trigger Efficiency of the P23 Data from P10 and E12 Triggers. Solid curve is a parameterized fit to the data.

Variable	Cut	# Passing P23
# 3D tracks	< 1	
P_T Photon	>22 GeV	
P_T Lead Jet	>10 GeV	
Isolation(cone=0.7)	<2.0 GeV (EM Only)	
E_T 2nd CES Clus	<1.0 GeV	
MEtSig	<3.0	
|ZVert| Pos	<50.0 cm	
|StripX| Pos	<17.5 cm	
StripZ Pos	217.0> StripZ >14.0 cm	
Total Passing Level 3		
Total Passing All Cuts		

Table 4.3: Events Passing Offline Cuts

0.0778, C=0.9610 ± 0.0173, D=24.241 ± 0.120. The inverse of the curve fit to the data

points is used to correct the data for the inefficiency of the trigger. Note that the offline

corrections to the P_T give us events with P_T below the theoretical threshold. The rapidly

falling P_T spectrum and the desperate need for statistics compelled us to use the data down

to 22 GeV and correct for the inefficiency of the trigger.

The statistics for the photon candidates passing each individual offline cut are tabulated

in Table 4.3.

70

Chapter 5

Background Subtraction

This chapter describes how the background is subtracted from the data. First the CES chambers are described in greater detail as is the χ^2 calculation. This is followed by a discussion of the determination of the background and signal χ^2 distributions from simulation that are used to fit the data. The details of the simulation can be found in Appendix B. Finally the subtraction is applied to the data as a whole to get an idea of the relative background contamination before the specific cuts for the $\cos \theta^*$ measurement are applied.

5.1 The CES Chambers and the Calculation of CES positions and χ^2's

The proportional wire chambers of the CES are imbedded approximately 6 radiation lengths (184.13 cm) deep into the lead-scintillator sandwich of the CEM. The anode wires and the cathode pads are arranged orthogonally so they can deliver R-θ (X) and Z information respectively (figure 5.1).

Strip Spacing =   1.67 cm in Towers 0-4
                  2.01 cm in Towers 5-9

Wire Spacing =   1.45 cm Throughout
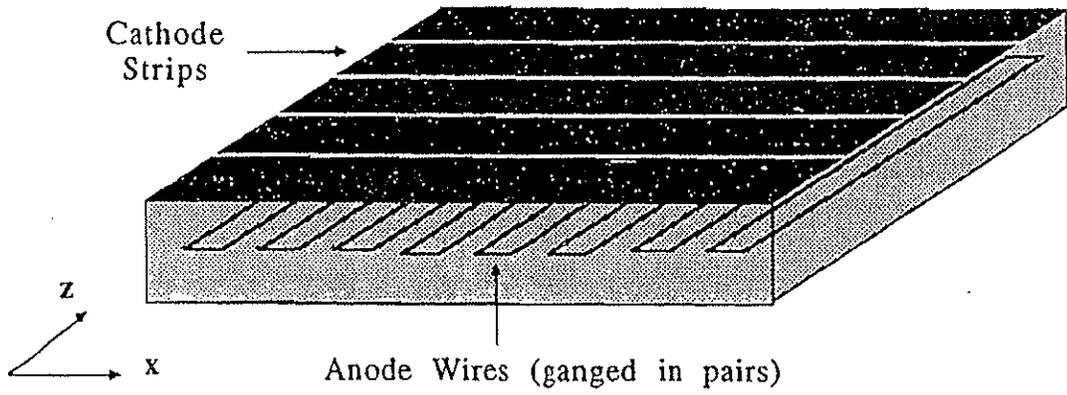
Figure 5.1: Schematic of the Central Strip and Wire Chambers

The CES chambers have much finer spacial resolution than the width of the single CEM towers and are used to extract the position of the center of the EM shower as well as to provide shower profile information necessary to distinguish single from multiple particle showers.

CES data are clustered in 11-channel clusters, centered around the highest seed channel above a 0.4 GeV threshold. The process is then iterated for the next highest seed that is outside a previous cluster until no unclustered seeds remain. Overlapping clusters share the energy in proportion to their seed energies.

The χ^2's for the data are obtained by comparing sample test beam (TB) shower profiles in both views to the profiles measured in the CES for the current event. The sample profile used in the 1988-1989 experimental run was a functional fit obtained from the average of 7-channel profiles taken from 50 GeV electrons in the 1985 TB. The profiles are scaled so that the area under the shower profiles is unity. The continuous functional fit of the sample profile is turned into a discreet profile by taking the area of the function within the boundaries of each channel. The midpoint of the sample profile within the center channel is allowed to float and is taken to be the point where the difference between the sample profile and the data profile are minimized in a least squares sense. The best center position of the sample profile in the wire and strip views are the CES cluster positions [39]. The only significant difference between the mechanics of the strip and wire χ^2's are that the continuous function used for the sample wire fit is completely symmetric where the strip function has an asymmetric component due to the geometry of the CES. In the strip view a shower will widen by a factor of $\frac{1}{\sin\theta}$ with increasing $|Z|$ due to a simple geometric effect (figure 5.2). Note that while the continuous functional fit of the wire profile is symmetric

the discreet profile can be made asymmetric to some degree by moving the profile off center within the middle channel.

The CES χ^2's can be then calculated by taking the difference between the data and the sample profile as follows:

$$(5.1) \qquad \chi^2 = \frac{1}{4} \sum_{i=1}^{11} \frac{[y_i - y(x_i)]^2}{\sigma_i^2}$$

where i is the CES channel index, y_i is the measured profile and $y(x_i)$ is the discreet sample profile with best fit center, and σ_i^2 is the estimated variance of the profile (obtained from comparing TB electron data to the sample profile). This is similar to a standard χ^2 per degree of freedom, but instead of dividing by the number of channels used in the comparison, a constant 4 was used.

5.2 The Background Subtraction Method

The background subtraction is performed by exploiting the expected difference in shower profiles between the signal (single photon) and the background (two or more photons from neutral mesons). On average the shower profile from a single photon should match the sample profile more closely than one from a multiple photon shower and give a lower calculated χ^2 (see figure 5.3).

As mentioned in the previous section this difference can not be exploited on an event by event basis, only on a statistical basis, due to the size of shower fluctuations and to the possibility of asymmetrical decays where one of the photons gets nearly all the energy from the decaying neutral meson and therefore closely mimics the shower profile of a single

74
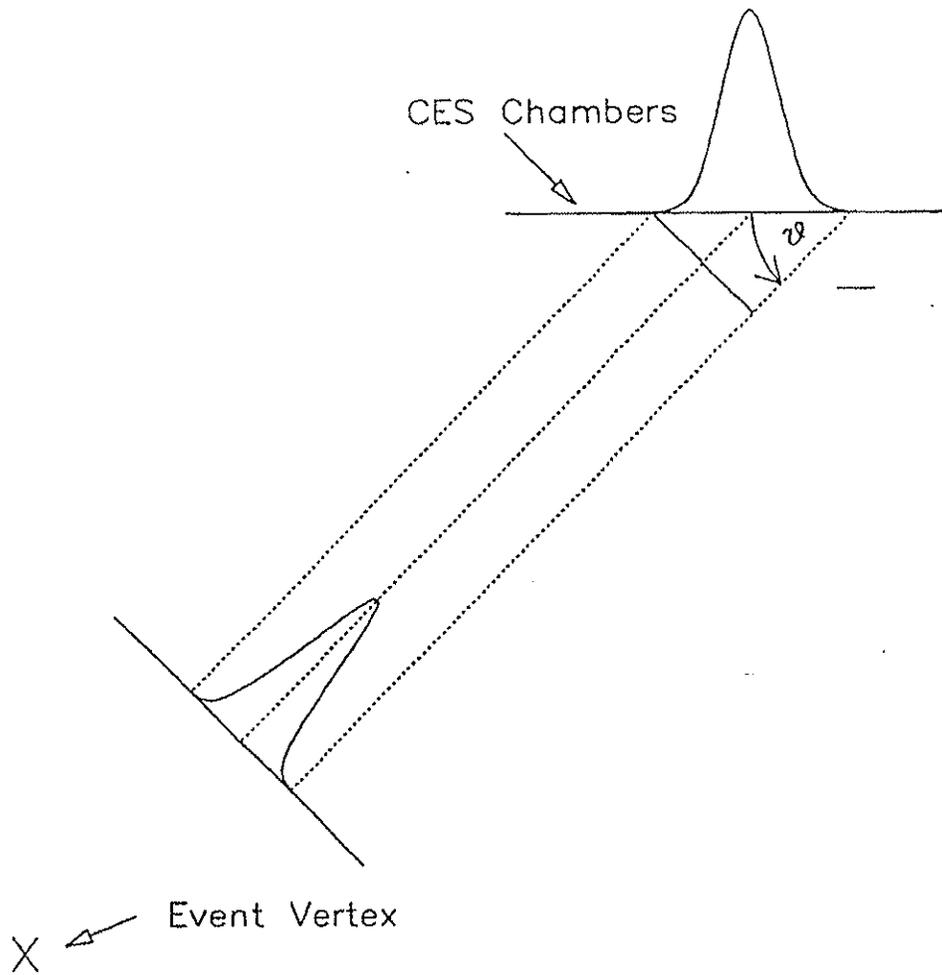
Figure 5.2: Shower Widening of $1/\sin\theta$ Due to Geometric Effects. The geometry of the central detectors causes the shower to be projected onto the axis of the CES chambers which effectively widens the shower.

75
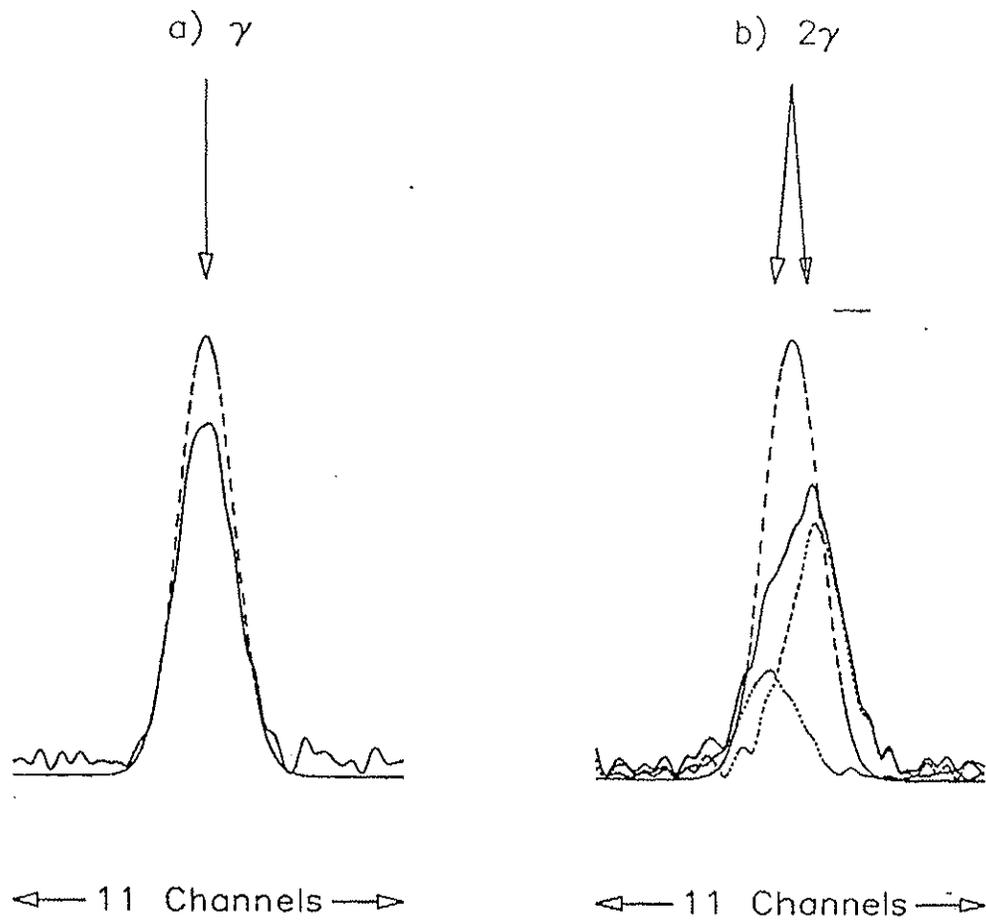
Figure 5.3: Schematic View of CES Shower Profiles for (a) signal and (b) background compared to sample profile. The dashed line represents the sample profile, the solid the incoming signal.

76

photon. Additionally the method breaks down when the resolution of the CES chambers is insufficient to separate spatially a pair of decay photons boosted by a sufficiently large P_T. The resolution of the wire and strip chambers is approximately 3 or 4 mm, which implies that two photons from a decaying π^0 are not resolvable beyond a P_T of $\sim$ 55 GeV (depending on the exact decay axis relative to the boost). In practice the signal and background profiles are too similar to allow subtraction much above 45 GeV.

The subtraction method requires "known" χ^2 distributions for both the signal and the background as functions of P_T. Obtaining correct χ^2 distributions are critical to the success of the subtraction method and details of their derivation from Monte Carlo will be discussed below. Assuming that one has those distributions the method is easily described as follows. The information from both profile views are utilized by considering a χ^2 formed from the average χ^2 of the two views (strip and wire). Figure 5.4 shows the χ^2 distributions of the signal, background, and data over the P_T region.

We reduce the χ^2 distributions of the signal, the background and data to a single number ϵ (efficiency) defined to be the fraction of events in a sample with $\chi^2 < 4$ over the total number of events with a $\chi^2 < 20$. We then can find the fraction of photons in the data as a function of P_T by mixing the efficiencies of the signal and background in the proper proportions to match that of the data. To illustrate this, suppose we had a given number of photons and background and their known efficiencies. We could use the following matrix form to predict the number of observed events with $\chi^2 < 4$ and $4 < \chi^2 < 20$.

77
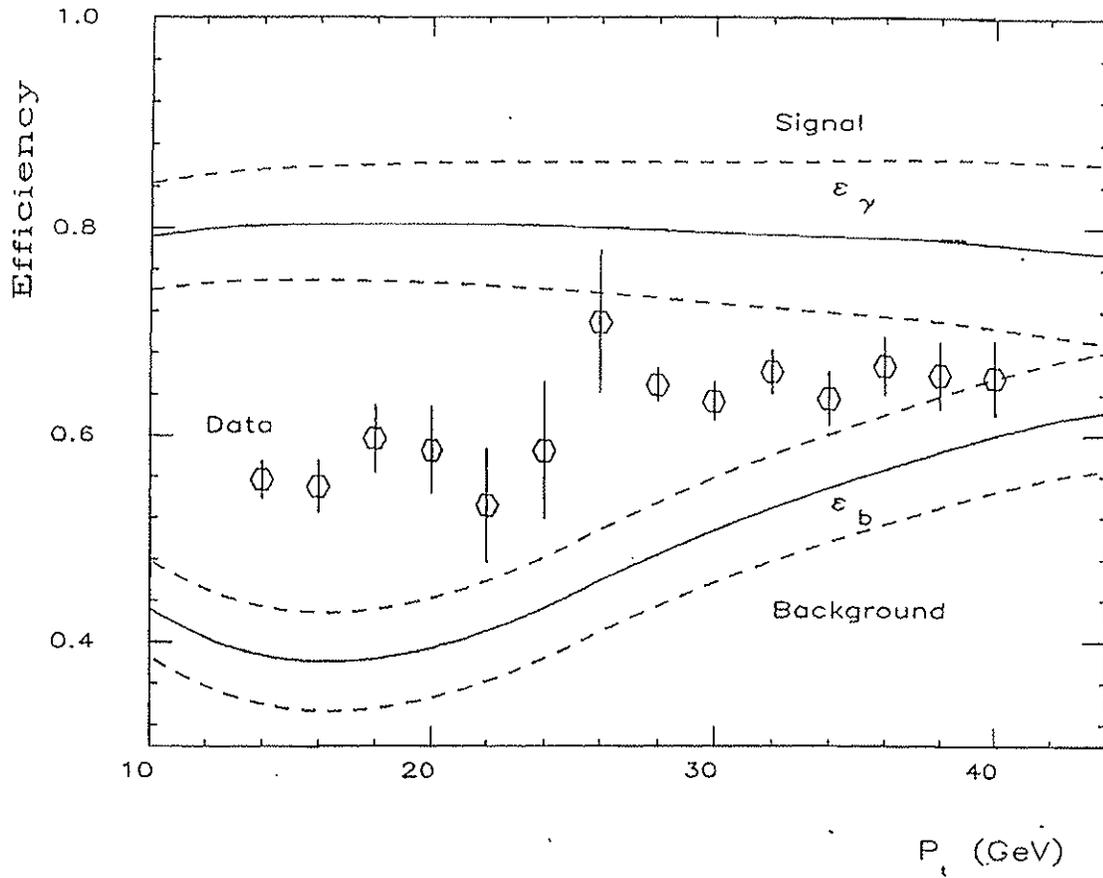
Figure 5.4: χ^2_{ave} Distributions for Signal, Data, and Background. The signal and background curve from a Monte Carlo simulation. Efficiency (ϵ) is the fraction of events with a $\chi^2 < 20$ that are also <4.

$$(5.2) \qquad \begin{pmatrix} N_{\chi^2 < 4} \\ N_{\chi^2 > 4} \end{pmatrix} = \begin{pmatrix} \epsilon_\gamma & \epsilon_B \\ 1 - \epsilon_\gamma & 1 - \epsilon_B \end{pmatrix} \begin{pmatrix} N_\gamma \\ N_B \end{pmatrix}$$

where ϵ_γ and ϵ_B are the χ^2 efficiencies of the signal and background and $N_{\chi^2} < 4$ and $N_{\chi^2} > 4$ are the number of events in the bin with $\chi^2 < 4$ and $4 < \chi^2 < 20$ respectively.

This matrix can be inverted to obtain N_γ and N_B, the number of photons and background events from the number of events with $\chi^2 < 4$ and $4 < \chi^2 < 20$ the efficiencies.

$$(5.3) \qquad \begin{pmatrix} N_\gamma \\ N_B \end{pmatrix} = \frac{1}{\epsilon_\gamma - \epsilon_B} \begin{pmatrix} 1 - \epsilon_B & -\epsilon_B \\ -(1 - \epsilon_\gamma) & \epsilon_\gamma \end{pmatrix} \begin{pmatrix} N_{\chi^2 < 4} \\ N_{\chi^2 > 4} \end{pmatrix}$$

Alternately one can consider each event individually and then obtain a weight for each event for its being signal or background by substituting for $(N_{\chi^2 < 4}, N_{\chi^2 > 4})$ (1,0) or (0,1) depending on its χ^2 and the appropriate ϵ's depending on the P_T of the event. This is what is done here. Each event is plotted with its appropriately calculated photon weight. It is worth noting that the result of this binary system of weighting is a positive photon weight, > 1, if $\chi^2 < 4$, and a negative weight for being background and *vice versa* if the $\chi^2 > 4$. The subtraction therefore has the effect of greatly enlarging the effective statistical error.

5.3   The Signal and Background χ^2 Distributions

Obtaining the proper χ^2 efficiencies for the signal and the background is crucial for performing a proper background subtraction. A fast detector simulation (QFL) was used to obtain the χ^2 distributions of the signal and background [29]. Given an event with a group

79

of final state particles, QFL simulates the response of each individual particle (including decay products) through each detector calorimeter component with test beam data. QFL can be used alone to simulate single particle responses in the detector or used in concert with an input module. If with the latter, the input module provides QFL with a list of particles (and their momenta) that enter the detector from the initial state reaction. The particles entering the detector are allowed to decay in the simulation through use of decay tables [40] and their individual momentum. The calorimeter response of each individual parent and the daughter are superposed to obtain the simulation of the entire event. Vertex position and tracking response are simulated by smearing with measured resolution functions. As mentioned in the previous section the source of the background are multiple-photons from single isolated neutral meson decays. The background events are easily simulated through the use of QFL's ability to decay neutral mesons and simulate the CES profiles by superposition of multiple TB profiles scaled appropriately according to energy and then the event χ^2 calculated as detailed above. The background χ^2 distribution can be obtained from the simulation of many such events.

If the production mixture of isolated neutral mesons were known *a priori* and it were possible to obtain test beam photon data for the CES response, obtaining the signal and background χ^2 distributions would be straightforward from QFL. However, most of the existing literature on direct meson production are not isolated and measured at different P_T's and/or Q^2 values. Therefore our values are obtained from this data set. The ratio of $\frac{\eta}{\pi^0}$ is measured at low P_T (figure 5.5) where the pair of photons can be resolved by the CES as lying in adjacent towers.

This allows a calculation of invariant mass and the distinctive mass peaks at ~ 0.14 and
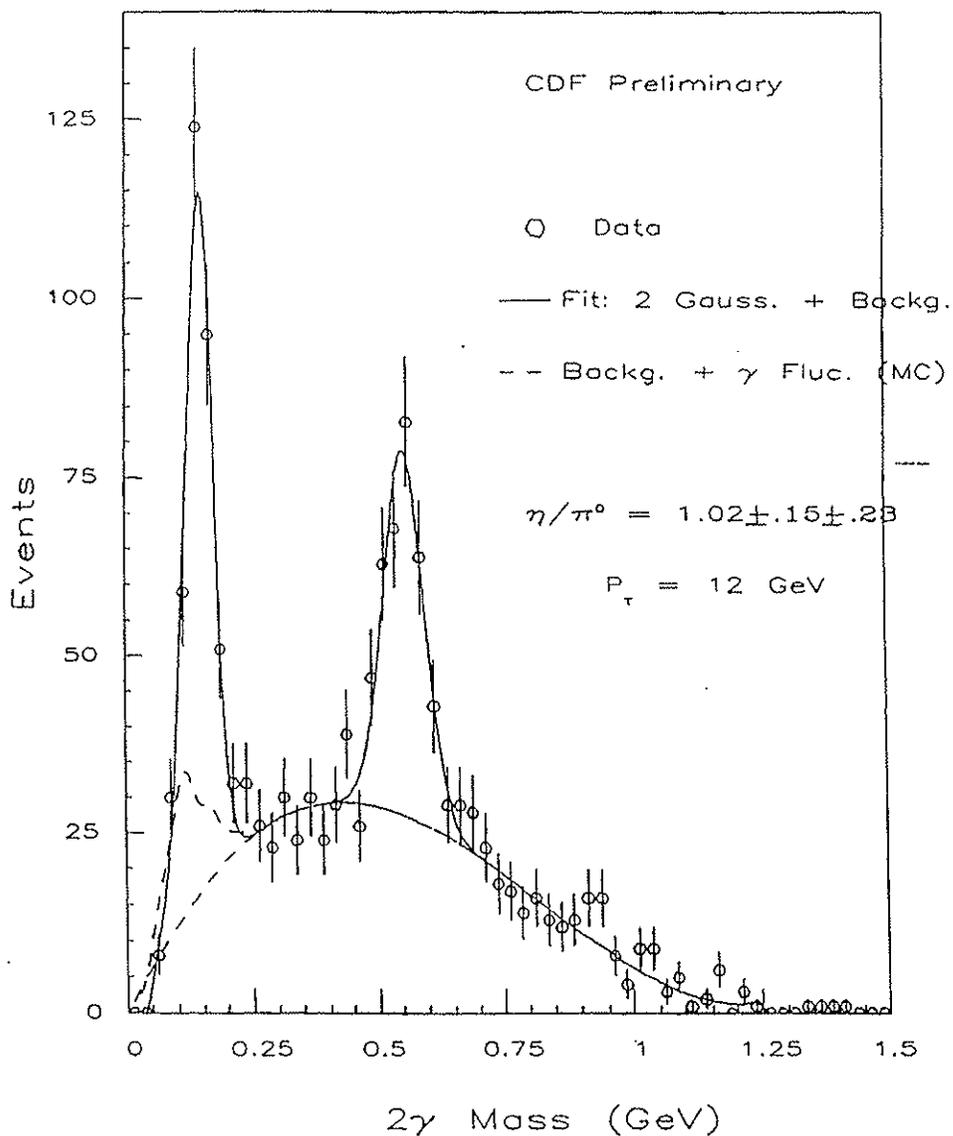
Figure 5.5: π^0 and η Mass Peaks Constructed from the Data with 3-Channel Strip Clusters . The number of events under the mass peaks were used to determine the ratio of isolated $\frac{\eta}{\pi^0}$ production. The points are the data with statistical error bars. The solid curve is formed from a fit to the data. The form of the fit assumed a gaussian signal plus a lorentzian background (dashed) plus an additional correction under the π^0 peak for fluctuations from single photons (from a Monte Carlo simulation)[41].

0.50 GeV deliver the ratio [37]. The $\frac{K^0_s}{\pi^0}$ ratio is not as critical as very few K^0_s's pass the isolation cut and is obtained from a direct production measurement [42]. The final mix of isolated mesons used in the the simulation was $(\pi^0 : \eta : K^0_s) \to (1.00 : 1.02 : 0.25)$, with errors $(0.0 : \pm 0.27 : \pm 0.2)$

Test beam electron shower profiles are used for photon showers in the CES simulation of QFL. This would be satisfactory if the shower response of photons and electrons were the same in the calorimeters (specifically the CES), but there are subtle differences that require some additional consideration. In a simple shower model, as seen in figure 5.6, once every radiation length λ a photon pair-produces into an electron-positron pair[1] and every electron radiates off a photon through bremstrahlung radiation and all daughters are half the energy of the parent particle. The calorimeters are only sensitive to the charged electrons in the shower. Therefore a photon shower really looks like the superposition of two electrons, each with approximately half of the photon energy and more importantly the photon shower development is *delayed* by the one radiation length it takes to pair-produce the electron pair. For determining the energy in the CEM only the nonlinearity is important between half and full energy as long as the EM showers are fully contained within the calorimeters.

However in determining CES energies and more importantly the shower profile χ^2's, there is a much greater difference because the CES was placed at showermax for electrons in order to obtain maximum statistics (and minimum fluctuations) from the secondary electrons in the shower. This means that the statistical fluctuations in the shower should be greater for photon showers than electron showers and as a result the χ^2's should be worse

---

[1]We are sloppy in the use of 'electron' usually meaning electron and/or positron, as for most purposes, the sign difference is of no practical consequence in our discussion.
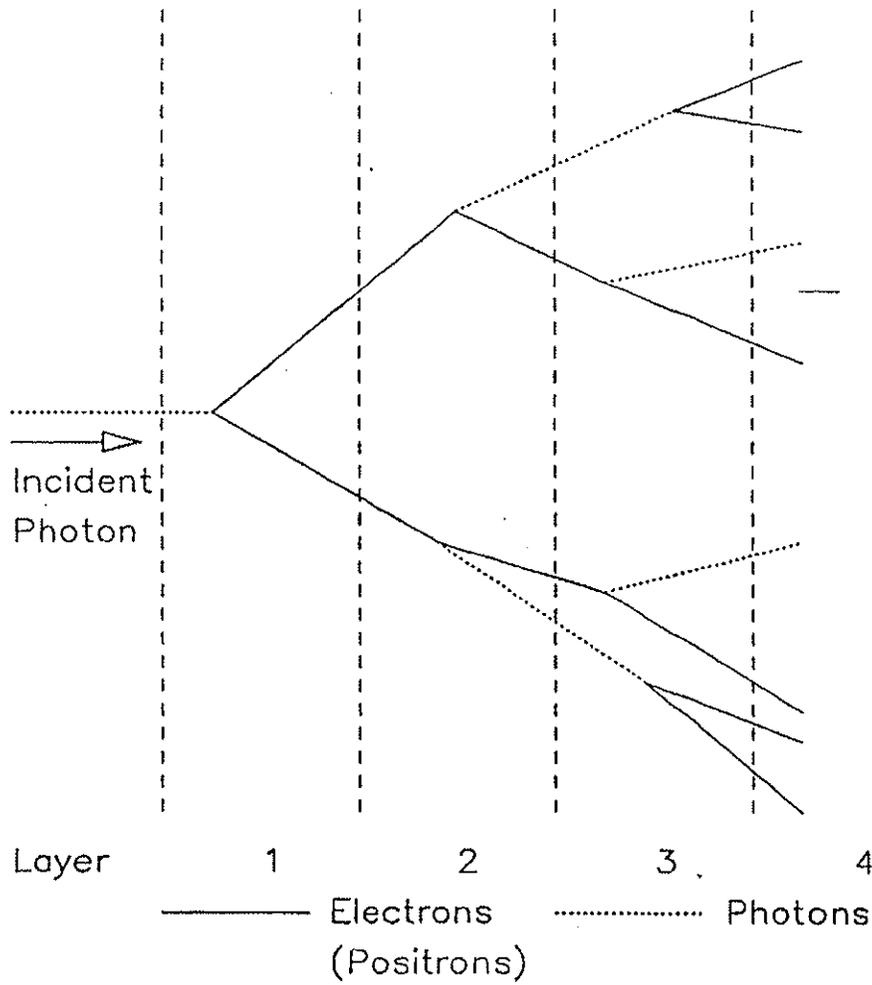
Figure 5.6: Simple Model of Electromagnetic Shower Development. Once every radiation length λ, every photon pair-produces an e^+e^- pair and every electron (e^+ or e^-) produces an extra photon through bremstrahlung radiation

than those predicted from electron showers which are used in the simulation. A correction to the simulation photon χ^2's was derived for this effect from shower theory and resulted in a P_T dependent correction to the σ's used in the determination of the simulation χ^2's (see equation 5.2). The exact form of the correction can be found in Appendix B along with a detailed discussion of the estimation of systematic errors for the simulation.

With the measured isolated production ratios for the neutral meson background and the correction for photon showers in the χ^2, the simulation was run sending single particles into the detector and the χ^2 distributions for the signal and background were extracted. Uncertainties in the simulation were incorporated into the error for the χ^2 efficiencies and included possible differences in background meson mix, effects of CES saturation in the data run, uncertainties in the photon shower correction and the inclusion of additional jet fragment energy [37]. The final simulation χ^2 distributions for signal and background are shown in figure 5.4, along with the data, before $\cos\theta^*$ cuts as a function of P_T.

Chapter 6

Direct Photon Cos Θ^*

In this section the actual photon CM angular distribution is presented. The data used

in this section is from the P23 sample only. The data from the P10 sample has larger

associated errors both from more limited statistics and from the larger uncertainty in the

effect of the minimum jet P_T cut. For completeness the results from the P10 data can be

found in Appendix D.

6.1 Transformations to Center of Mass and Acceptance

The data of the hard scattering processes of interest are measured in the lab frame which in

general is not the center of mass (CM) reference frame. There is an arbitrary lorentz boost to

the system which is not always directly measurable due to particle losses down the beamline

and confusion between what belongs to the hard scattering and what is underlying event.

However if the hard interaction of interest is a $2 \rightarrow 2$ process, the boost can be inferred

from the Z components of the two outgoing legs of the interaction which are identified as

energy clusters in the calorimeters.

For direct photon data one of the outgoing particles of the hard interaction is a photon and the other is a QCD jet. In figure 6.1 we define the angle θ^* to be the angle in CM between the outgoing photon candidate and the proton beam direction.

We choose to ignore the sign and implicitly plot $0.0 < |\cos\theta^*| < 1.0$.[1] The transformation to CM is easily performed taking advantage of the additive properties of the variable pseudorapidity (η). η^* (CM pseudorapidity), η_B (boost angle from CM to lab), P^* (CM momentum), and θ^* are obtained from Lab P_T, and the η's of the photon and jet *via* the following relationships:

$$(6.1) \qquad \eta^* = |\frac{\eta_\gamma - \eta_J}{2}|$$

$$(6.2) \qquad \eta_B = |\frac{\eta_\gamma + \eta_J}{2}|$$

$$(6.3) \qquad P^* = P_T \cdot \cosh\eta^*$$

$$(6.4) \qquad \tanh\eta^* = \cos\theta^*$$

When measuring a differential angular distribution special care must be taken ensure that the angular acceptance is uniform in the other variables or correctable in an acceptable fashion. For $\frac{dN}{d\cos\theta^*}$ this means having a uniform acceptance in P^* and η_B over the measured range of η^*. Since the direct photon momentum spectra is not precisely known we have elected not to make any angular corrections and cut the data to be uniformly accepted

---

[1] The angular distribution of direct photons should be symmetric with respect to the beam directions (photons do not care if they come from a quark or an antiquark) so we fold the angular distribution about $\cos\theta^* = 0$.
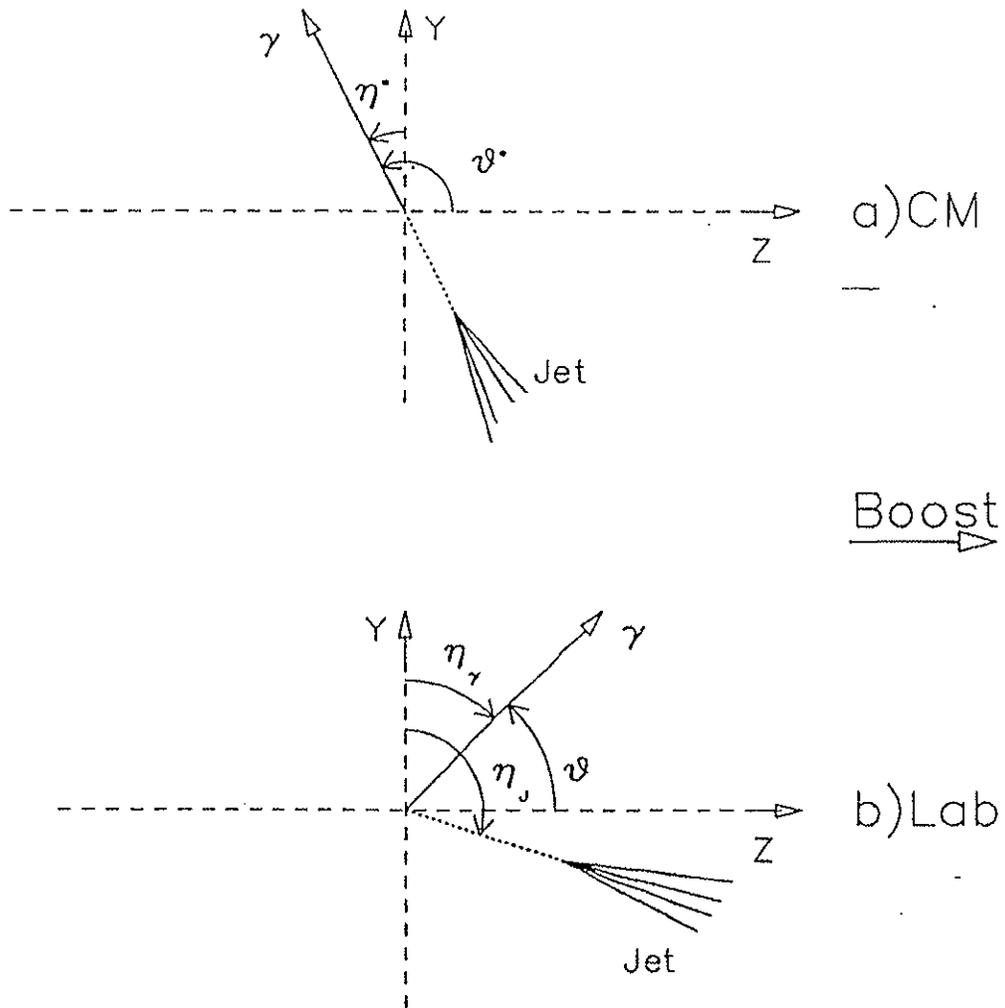
Figure 6.1: Definition of $\text{Cos}\theta^*$ Variables. (a)CM variables (b) Lab variables.

in η and make P_T corrections only to a region of phase space where we have measured data. Photons were only triggered in the central to a maximum η of 0.9. This means that the maximum single region of uniform acceptance one could reach was an η^* of 0.9 which corresponds to $\cos\theta^*$ of 0.7. In order to reach out a bit further in $\cos\theta^*$ two overlapping regions each of uniform acceptance are chosen and the areas of overlap used to normalize between them as in figure 6.2.

The data are shown in figure 6.3 plotted η_{jet} vs η_γ. The diagonals at 45° are the η_B and η^* axes.

The boxes show the regions of uniform acceptance in η_B and η^*. Photons are accepted from $-0.9 < \eta_\gamma < 0.9$ and $\eta_\gamma = \eta_B + \eta^*$ so we can choose any rectangle in η^*-η_B space to be an area of uniform acceptance just as long as $-0.9 < (\eta^* + \eta_B) < 0.9$. The regions chosen are:

(6.5)   Region1 : $|\cos\theta^*| < 0.6$

$$0.0 < \eta^* < 0.7 \text{ and } -0.9 < \eta_B < 0.2 \text{ or}$$

$$-0.7 < \eta^* < 0.0 \text{ and } -0.2 < \eta_B < 0.9$$

(6.6)   Region2 : $0.3 < |\cos\theta^*| < 0.8$

$$0.3 < \eta^* < 1.1 \text{ and } -1.2 < \eta_B < -0.2 \text{ or}$$

$$-1.1 < \eta^* < -0.3 \text{ and } 0.2 < \eta_B < 1.2$$

The complication stems from trying to obtain a uniform acceptance in P^* and the fact

88
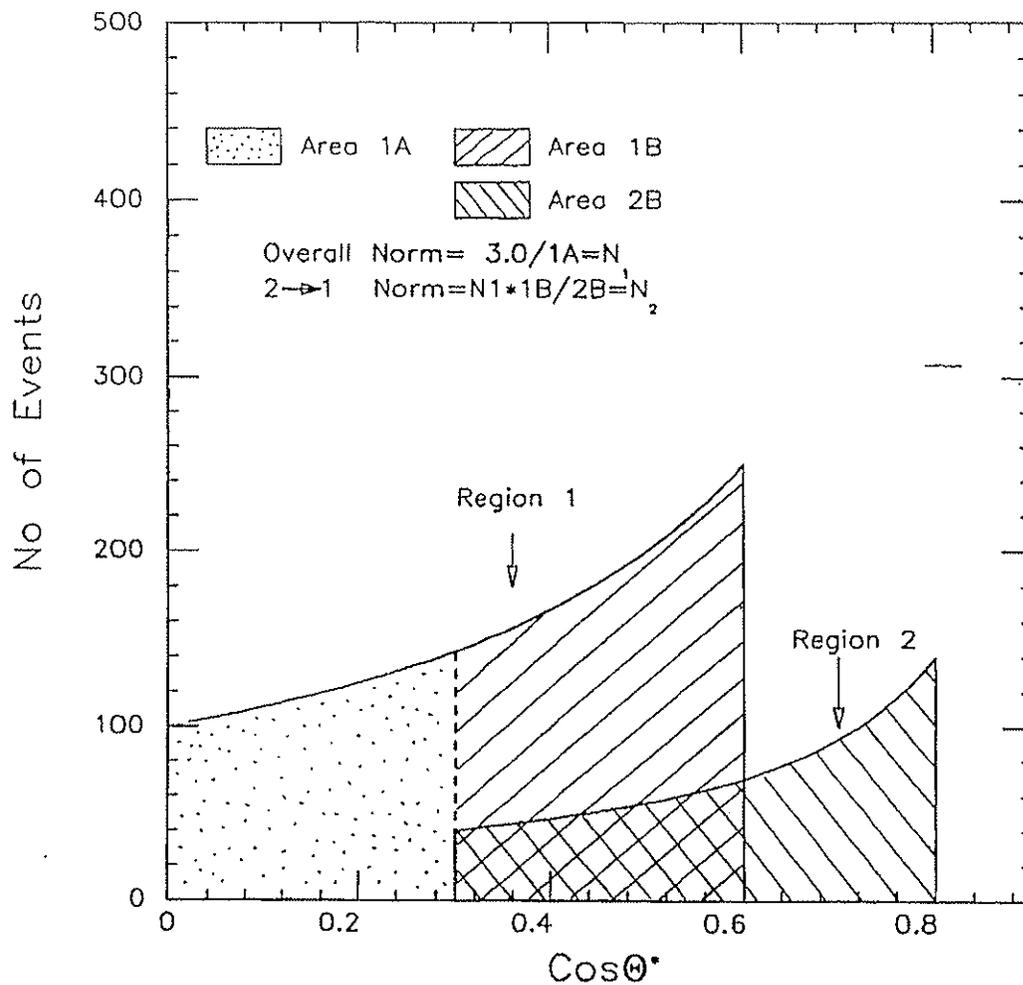
Figure 6.2: A schematic view of the analytical method. Two regions each flat in acceptance are selected from the data. The regions are in $| \cos \theta^* |$ 0.0-0.6 and 0.3 -0.8. The area of overlap from 0.3-0.6 is used for relative normalization and the area in region 1 from 0.0-0.3 where the curve is relatively flat is used for an overall normalization so the data can be compared to dijet data and theory that have a much higher total cross-section. The largest systematic error is driven by the number of events in the overlap area of region 2.
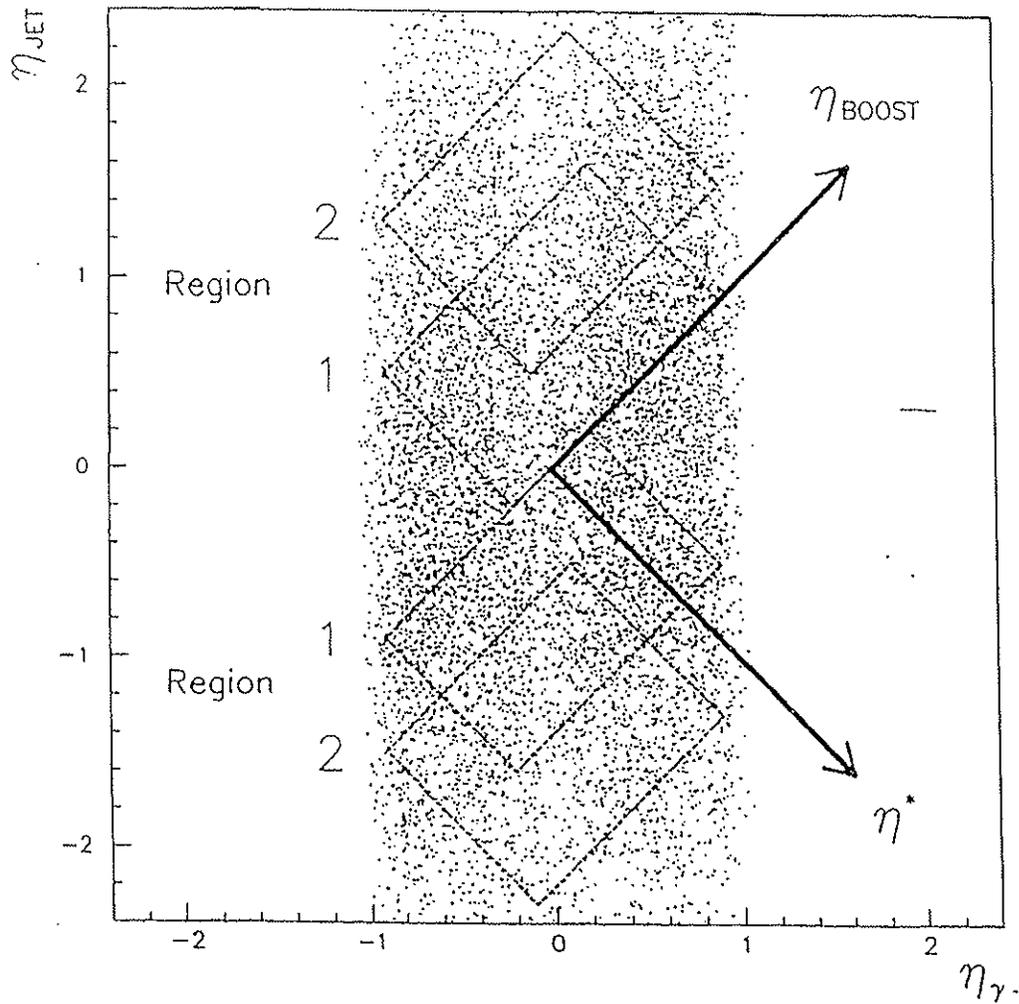
Figure 6.3: Data Plotted η_{jet} vs η_γ. The diagonal axes are the sum (η_{Boost}) and difference (η^*) axes. The rectangular regions represent regions of flat acceptance in η^*-η_B space. The overlapping regions are used for normalization. Note that not all the points within a given box are used because there is an additional acceptance cut in P^*. Some, but not all, points in the overlap area are common to both regions after all acceptance cuts are made.

90

that the data were measured in lab, not in CM so the trigger threshold was in transverse momentum (P_T) and not P^*. The minimum P^* comes from a combination of both the threshold P_T and the maximum η^* and the maximum P^* comes from the minimum η^* and the maximum P_T, which is the point where photons can no longer reliably be separated from background.

$$(6.7) \qquad\qquad P^*_{\min} = P_{T\min} \cdot \cosh \eta^*_{\max}$$

$$(6.8) \qquad\qquad P^*_{\max} = P_{T\max} \cdot \cosh \eta^*_{\min}$$

The rapidly falling momentum spectrum implies that most of the data is piled up at the lower boundary of P^*. This, coupled with the exponential nature of the function hyperbolic cosine, means that raising the upper limit of η^* will greatly reduce the available statistics. It turns out that even if there were photons triggered outside the central it would not necessarily be desirable to use a single uniform region in order to take full advantage of all the triggered data. It is also advantageous to push the lower limit in P^* below the point where the trigger is efficiently triggering in P_T and correct for the inefficiency. Figure 6.4 is a plot of P_T vs. η^* and the curves are lines of constant P^* illustrating the limits of the two regions.

We have chosen $P_{T\min} = 22$ GeV and $P_{T\max} = 45$ GeV (even though the trigger is only about 15% efficient at 22 GeV). The P^* limits chosen are:

$$(6.9) \qquad\qquad \text{Region1} : |\cos\theta^*| < 0.6 : 27.6 < P^* < 45\text{GeV}$$
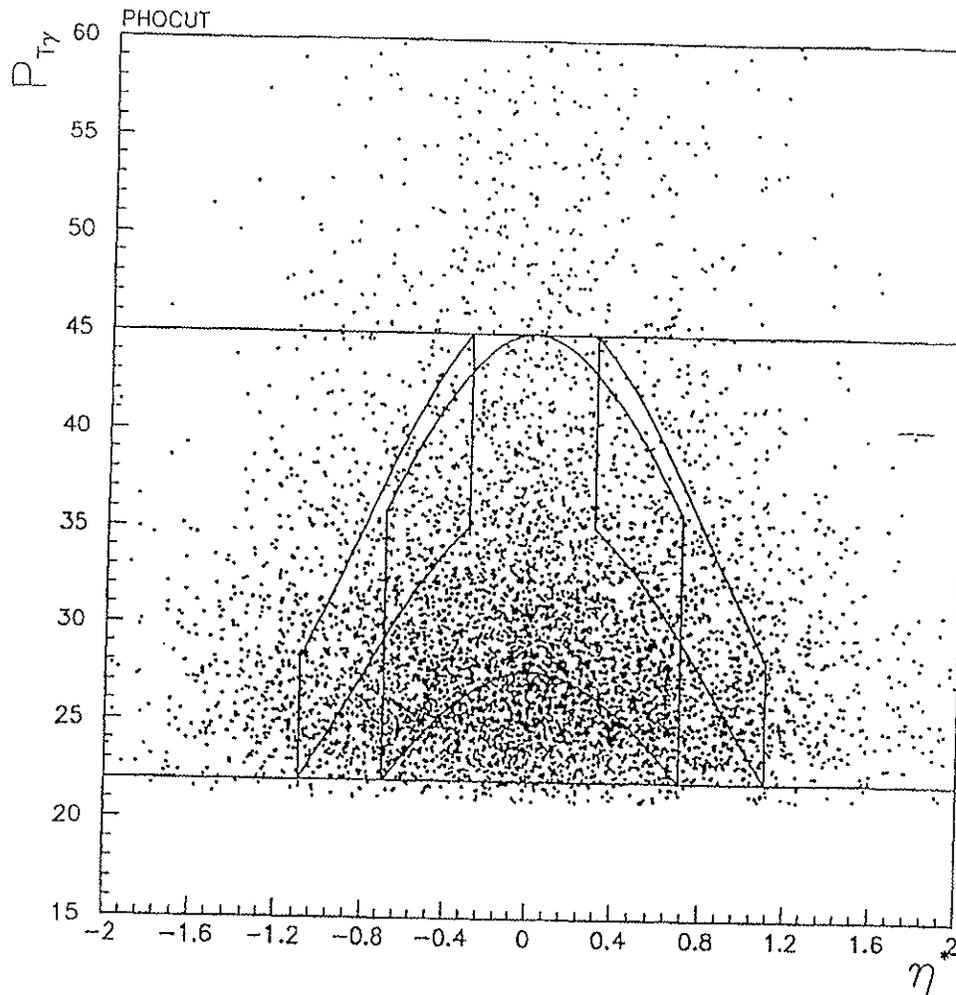
Figure 6.4: Plot of Data P_T vs η^*. This demonstrates the cuts designed to make each region uniform in P^* acceptance. The curves are lines of constant P^*. The area between the cuts are regions of uniform acceptance in P^* and η^*; this projection of the data does not show η_B.

$$(6.10) \qquad \text{Region2} : 0.3 < |\cos\theta^*| < 0.8 : 36.7 < P^* < 47\,\text{GeV}$$

Figure 6.5 is a plot of $\cos\theta^*$ for our above cuts where the events have been weighted to account for trigger efficiency but background has not been subtracted.

The exponential rise of the function cosh means that when the P^* threshold is lowered by lowering the acceptable P_T from 22 to 25 GeV only the last bins in each region will contain events with $P_T < 25$ GeV. The other bins all add events of the same P^* range but with $P_T > 25$ GeV that are efficiently triggered. This is an important point because the largest systematic error in the data is the normalization between regions which is almost solely driven by the statistics in the overlap area of region 2 and the extra events in the overlap region are all efficiently triggered. The drawback comes from the addition of the inefficient events which have a large uncertainty, but this is not of great concern as long as the trigger efficiencies are known to sufficient accuracy and these events do not make up too large a fraction of the total events in that bin.

6.2 Lead Jet vs. Multiple Jets

Gluon radiation is highly probable at Tevatron energies and comparison to recent NLO calculations is desirable so it is necessary to consider the treatment of events with more than one identified jet cluster. The method for calculating η^* and ultimately $\cos\theta^*$ explicitly assumes a $2\rightarrow2$ system. When there are more than one identified jet cluster the boost can be calculated in two different ways and still retain the simplicity of the $2\rightarrow2$ system.

First the calculation of $\cos\theta^*$ can be done by considering only the η's of the photon candidate and the lead jet. The lead jet is defined by the jet in the event that had the

UnSub Direct Photon dN/dCosΘ*

CDF Preliminary

$\quad$ O $\quad$ γCand+Jet $\quad$ 27.6<P*<47GeV

$\quad$ ·········· LO QCD Jet+Jet

$\quad$ ——— NLO QCD γ+Jet (Owens)

$\quad$ ---- LO QCD γ+Jet
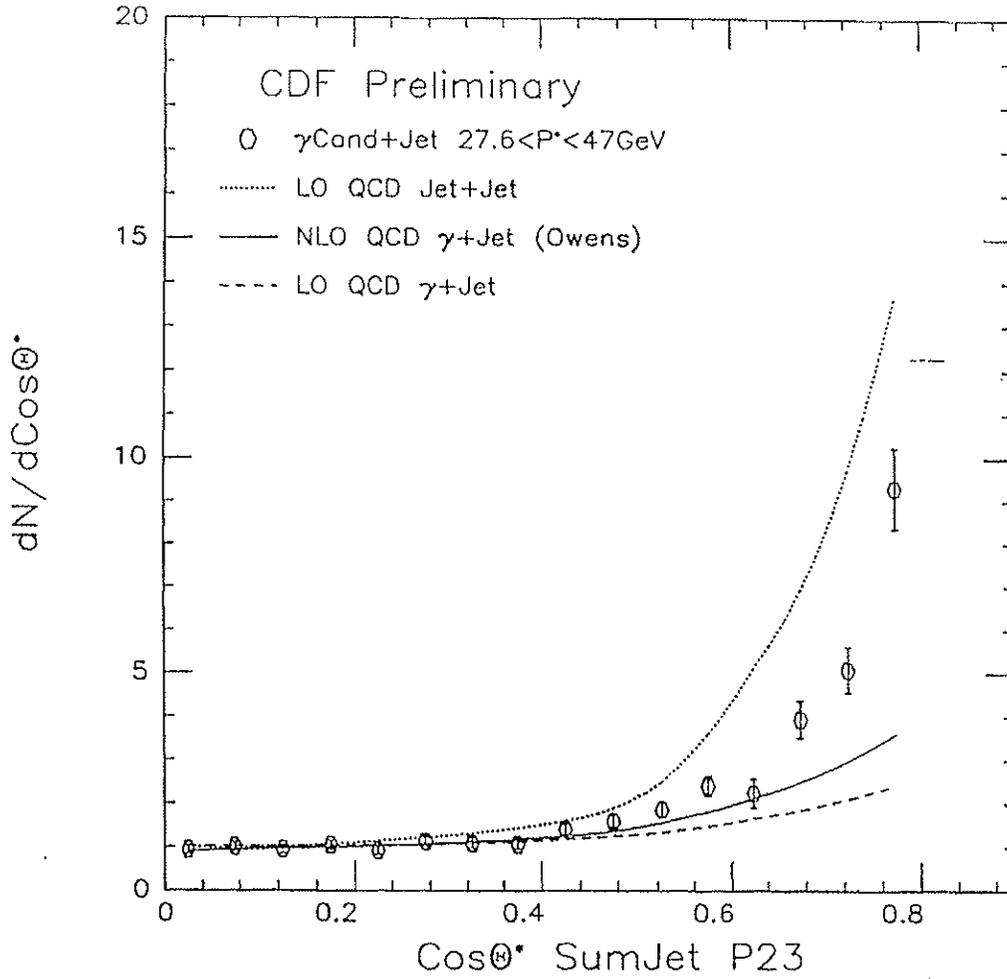
Figure 6.5: Cosθ* of Data Before Background Subtraction. All cuts in η*, η_B and P* are made to ensure flat acceptance. The data from 0.0-0.6 are from region 1, the data from 0.6-0.8 are from region 2 after normalization from the overlap. Error bars are statistical only and corrections have been made for trigger inefficiencies.

94

highest P_T after all corrections. Clearly in this case the system boosted to will not be the actual CM system if there is gluon radiation and therefore will not be the actual θ^* of the system. However, if the gluon radiation is small (*i.e.* if the lead jet has most of the recoil momentum) then it should be very close. Alternately in order to find the best value of CM and to preserve the the simplicity of the $2 \to 2$ system, the boost can be obtained from the η's of the photon and a summed jet where the summed jet η is taken to be the direction of the vector momentum sum of the leading three jets (defined again by corrected P_T) that pass all jet cuts. This includes a minimum jet $P_T > 10$ GeV and a requirement that a jet lie in the opposite hemisphere in ϕ from the photon candidate (back to back cut). If the lead jet fails the opposite hemisphere cut in ϕ or the P_T cut, the event is discarded. If a second or third jet fails the cut, it is not included in the sum. Both methods (dubbed Sumjet and Leadjet respectively) are used here and the results compared.

6.3 Direct Photon Cos θ^*

After all the above definitions and cuts we are ready to present the angular distributions. Figure 6.6 is a plot of $\cos \theta^*$ for the P23 data sample after subtraction for the Sumjet method.

The open circles are the P23 data with the inner error bars reflecting the statistical error after subtraction and the outer error bars reflecting the estimated systematic and statistical errors added in quadrature. All data and MC curves are normalized so the flat part of the curve (from $0.0 < |\cos \theta^*| < 0.3$) averages 1.0 along the Y-axis. The choice of normalization was selected in order to accentuate the difference in rise between the dijet curves and those
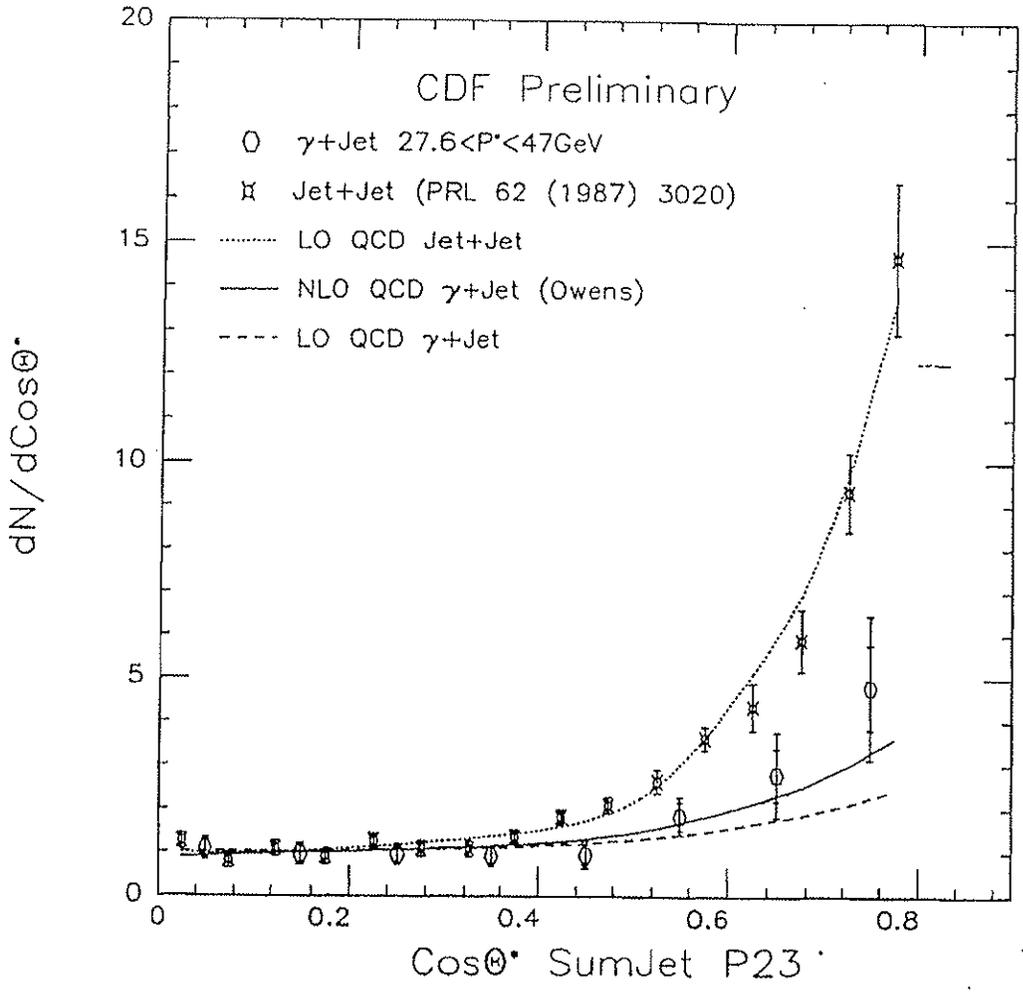
Figure 6.6: Direct Photon $\text{Cos}\theta^*$ After Subtraction for the Sumjet Method. Here all identified jets in the hemisphere opposite the photon candidate are summed to make a single jet to perform the boost from lab to CM. Inner error bars are statistical errors only; the outer are statistical and systematic errors added in quadrature.

from direct photon production at shallow angles. The points are dijet data from the CDF 1987 run [43] which is from an invariant mass region $(2 \cdot P^*)$ above 148 GeV compared to an average of around 50 GeV for the direct photon data presented here.[2] The curves are from QCD theory predictions, the dijet curve (dots) is a tree-level LO order QCD calculation as is the LO direct photon curve (dashes) [19]. The NLO curve is from a full NLO calculation including all bremsstrahlung and tree-level diagrams [17]. The two leading order theory curves were obtained from parton level calculations with the effects of underlying event (K_T Kick). The NLO curve was also obtained from the parton level but contains no such K_T correction; neither curve contains detector effects. Full detector simulations were run with LO calculations used as a MC generator to determine the effects of detector cracks and detector angular smearing on the data. The effects were small and are included in the systematic error. An in depth discussion of the estimation of the systematic errors and their breakdown can be found in the next section. Figure 6.7 is for the same data with $\cos\theta^*$ calculated with the lead jet method.

The LO dijet data and theory curves are of course unchanged; the NLO direct photon curve has $\cos\theta^*$ calculated in the same lead jet fashion. Interestingly enough the NLO direct photon curve now resembles the LO. However the Leadjet data, considering the size of the error bars, reflect the same curve as the one measured using the Sumjet method.

The Sumjet (Leadjet) data are shown in Table 6.1(2) after subtraction but unnormalized. The number of events is the raw number of events and is not corrected for trigger efficiency but the signal photons and errors contain all weights and corrections.

---

[2]Even though the invariant mass regions for the dijet and direct photon data presented in figure 6.7 are not identical it is the best comparison available with CDF data as the dijet data taken in the 1988-1989 data run is from a much higher invariant mass range.

Direct Photon dN/dCosΘ*
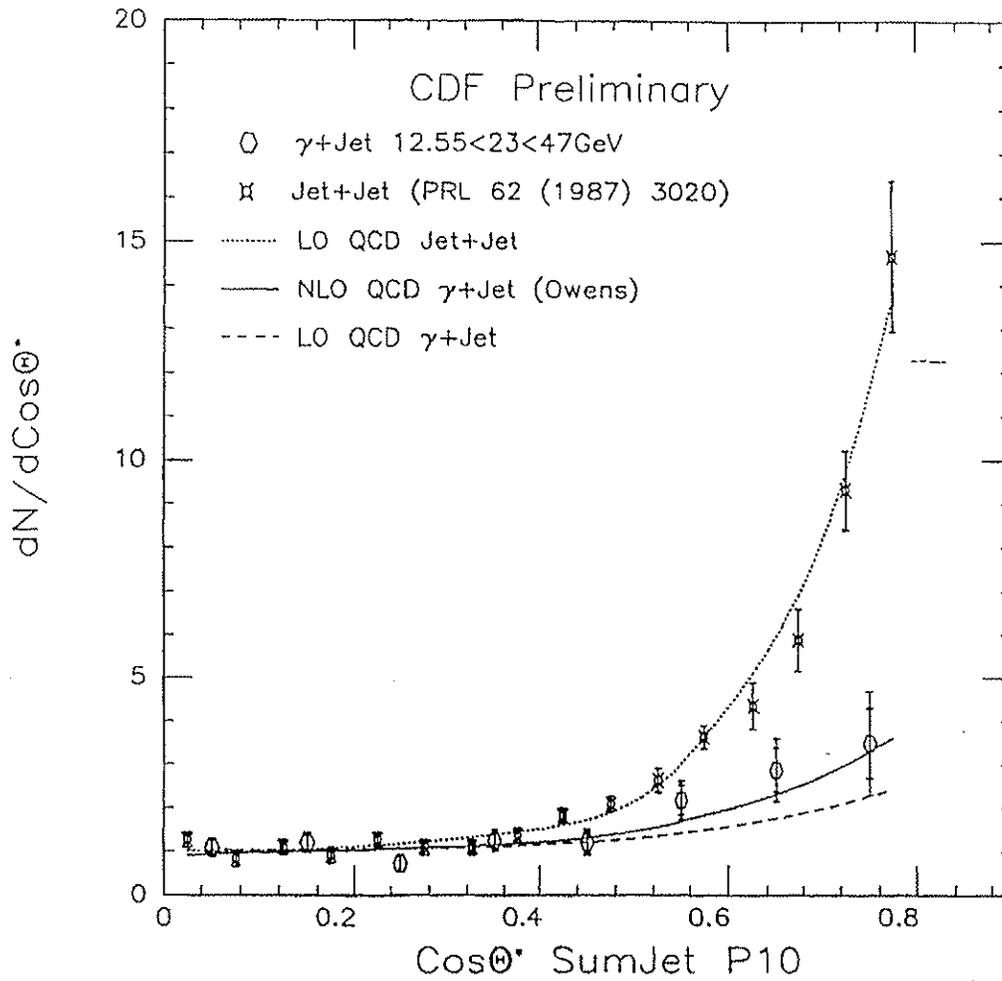
Figure 6.7: Direct Photon Cosθ^* for the Leadjet Method. Here the boost from lab to CM is found from only the photon and the lead jet (jet with highest corrected P_T).

$\cos\theta^*$	#Events	Sub γ	StatErr	SysErr	TotErr
0.0-0.1	199	148.47	28.26	20.07	34.67
0.1-0.2	204	132.79	29.48	17.42	34.24
0.2-0.3	208	129.07	28.16	16.78	32.78
0.3-0.4	213	125.31	27.65	17.05	32.48
0.4-0.5	280	127.65	32.26	26.89	42.00
0.5-0.6	316	242.42	42.19	39.36	57.68
0.6-0.7	128	95.74	20.76	26.05	33.32
0.7-0.8	219	158.00	32.23	44.76	55.17

Table 6.1: Unnormalized Sumjet P23 Data.

$\cos\theta^*$	#Events	Sub γ	StatErr	SysErr	TotErr
0.0-0.1	240	127.51	31.91	22.08	38.80
0.1-0.2	208	180.94	28.43	28.52	40.27
0.2-0.3	224	141.69	29.35	17.46	34.15
0.3-0.4	237	145.90	29.57	18.15	34.70
0.4-0.5	288	125.34	32.65	25.42	41.38
0.5-0.6	360	256.54	46.08	38.99	60.36
0.6-0.7	121	94.65	20.15	34.64	40.07
0.7-0.8	185	114.72	29.22	46.89	55.25

Table 6.2: Unnormalized Leadjet P23 Data.

6.4 Systematic Errors

The following is a discussion of the uncertainties in the measurement. The uncertainties in descending order of importance are the normalization, the values of the χ^2 efficiency, trigger efficiency, and acceptance considerations, the latter includes detector cracks, detector resolution, and jet identification. The systematic errors are broken down by bins of $\cos\theta^*$ in Table 3 at the end of this section.

The largest systematic error by far is the choice of normalization. In some sense this is not a true systematic error because it is dependent directly upon the statistical errors of the regions of phase space used to normalize. It also does not effect all points equally as there are two different regions of phase space used to form the final $\cos\theta^*$ curve. However the last two points have the same normalization, as do the first six points, so within these two sets of points the normalization error is completely correlated and is regarded as systematic error. In the first region $0.0 <| \cos\theta^* |< 0.6$, the normalization error was estimated from the total statistical error of the entire region used for that region's normalization ($0.0 <| \cos\theta^* |< 0.3$).

Mathematically, the normalization (figure 6.2) can be written as:

(6.11)
$$N1 = \frac{3.0}{\sum_{1A} Wt_i}$$

(6.12)
$$N2 = \frac{N1 \cdot \sum_{1B} Wt_i}{\sum_{2B} Wt_i}$$

where N1(2) is the normalization in region 1(2),and 1A is the area of phase space

$0.0 < |\cos\theta^*| < 0.3$ in region 1 and 1(2)B is the area from $0.3 < |\cos\theta^*| < 0.6$ in region 1(2) and the Wt_i's are the data event by event after subtraction. The factor of 3.0 comes from the normalization over three bins.

The % error on the normalization of region 1 is given by:

$$(6.13) \qquad \frac{\Delta N1}{N1} = \frac{\sum_{1A}(Wt_i)^2}{(\sum_{1A} Wt_i)^2}$$

The normalization for the last two points is a little bit more complicated. It is the estimated error in normalization in region 1 (first six points) summed in quadrature with the additional error from normalizing between regions 1 and 2. In calculating the uncertainty of the normalization from the two regions one has to be careful, as some of the data points are common to both regions. Taking this into account we find that the total % error for the last two points from taking partial derivatives to be:

$$(6.14) \qquad \frac{\Delta N2}{N1} = \sqrt{\left(\frac{\Delta N1}{N1}\right)^2 + \left(\frac{\Delta\alpha}{\alpha+\beta}\right)^2 + \left(\frac{\Delta\beta\cdot(\alpha-\gamma)}{(\alpha+\beta)(\beta+\gamma)}\right)^2 + \left(\frac{\Delta\gamma}{\beta+\gamma}\right)^2}$$

where $\alpha = \sum_{1B}(Wt_i)$ for the events unique to region 1, $\gamma = \sum_{2B}(Wt_i)$ for the events unique to region 2, $\beta = \sum_{B}(Wt_i)$ for the events common to regions 1 and 2 and the $\Delta\alpha\beta\gamma$'s$=\sum(Wt_i)^2$ over the points in the appropriate regions.

This error is dominated by the relative size of the last term which is essentially the statistical error of the points in the overlap area of region 2. This is because this region has

101

the lowest statistics of any of the areas. The relative size of $\frac{\Delta N1}{N1}$ was found to be about

12% while $\frac{\Delta N2}{N1}$ was about 26% for the data in the P23 sample.

The systematic error due to the uncertainty in the χ^2 efficiencies was found by varying

the efficiencies by the maximum uncertainty for the MC photon and background χ^2's,

in a correlated fashion, and repeating the analysis. The resulting new curves were then

normalized in the same fashion and the largest deviation ($+$ or $-$) from the original curve

was taken to be the error. No attempt was made to keep asymmetrical errors. The error

was variable from point to point but was almost always less and usually much less than

the normalization error. Note that the seemingly large error (see Table 6.3) for the point

$0.4 \, |< \cos\theta^* \,|< 0.5$ is caused by an unusually large number of $\chi^2 > 4$ events that populate

that bin which also causes its signal to be slightly low. This effect and the anomalously high

value for the second point in the Leadjet curve are probably just statistical fluctuations.

Most of the bins have $\chi^2 < 4$ for 67% of the events but the high bin has 74% and the low bin

has 61%. Even small deviations in the χ^2 efficiencies have a large effect upon the relative

amount of signal resulting from the subtraction but once normalized, the resulting change

in the angular distribution is small. That is to say the χ^2 efficiencies have a large effect on

the direct photon cross section but not so much on $\cos\theta^*$.

The systematic error from the uncertainty in the trigger efficiency is found by redoing

the analysis with the 1σ error trigger efficiency curve shown in the previous chapter. The

uncertainty varies from bin to bin depending upon the exact P_T distribution within a bin

of $\cos\theta^*$ but is largest in the last bin where the most inefficient triggers with the largest

corrections occur. However even there it is only at worst a 7% error.

The method adopted here was chosen specifically to ensure as uniform an acceptance in

102

η as possible; however there still is the possibility that η cracks in the detector may cause difficulties in jet identification and overall acceptance. All real direct photon events should have a least one jet recoiling opposite in ϕ with roughly the same transverse momentum (modulo underlying event). The energy resolution for jets is much worse than that for photons and so often the jet P_T's will be quite different from that of the photon. It is also possible for the jet clustering algorithm to cluster non-jet energy (underlying event) erroneously and because of fluctuations or real jets degraded by the detector cracks, to have the false jet appear to be the dominant one. In that case, the Leadjet method will find an incorrect CM for the event. This would have the effect of lessening the shallow angle peaking of the angular distribution as the CM angle found from the photon and a randomly positioned jet should be flat. This effect would be slightly lessened when you go to the Sumjet method as the real jets will tend to pull the incorrect lead jet back toward the proper position. Raising the minimum jet P_T reduces the possibility of interference from clustered underlying event and the jet clustering algorithm has been found to be completely efficient at corrected energies of 15 GeV [35]. However a higher threshold also increases the chance of losing a jet in cracks. A full detector simulation (QFL) was run using papageno (γ + 1Jet) as the event input generator to test η acceptance over the range of the P23 sample. The simulation included vertex smearing, 'K_T kick', and an underlying event simulation. Figure 6.8 is the ratio of $\cos \theta^*$ for the detector simulation over the generated signal after all cuts and corrections, with the jet P_T cut paced at 10 GeV corrected.

While there is some overall acceptance loss (ratio < 1), it is relatively flat. Figure 6.9 is the same for a Jetcut $P_T > 15$ GeV and shows the acceptance falling off by 15% in the last bin ($0.7 <| \cos \theta^* |< 0.8$) which corresponds to the the 30° crack (the central-plug

103
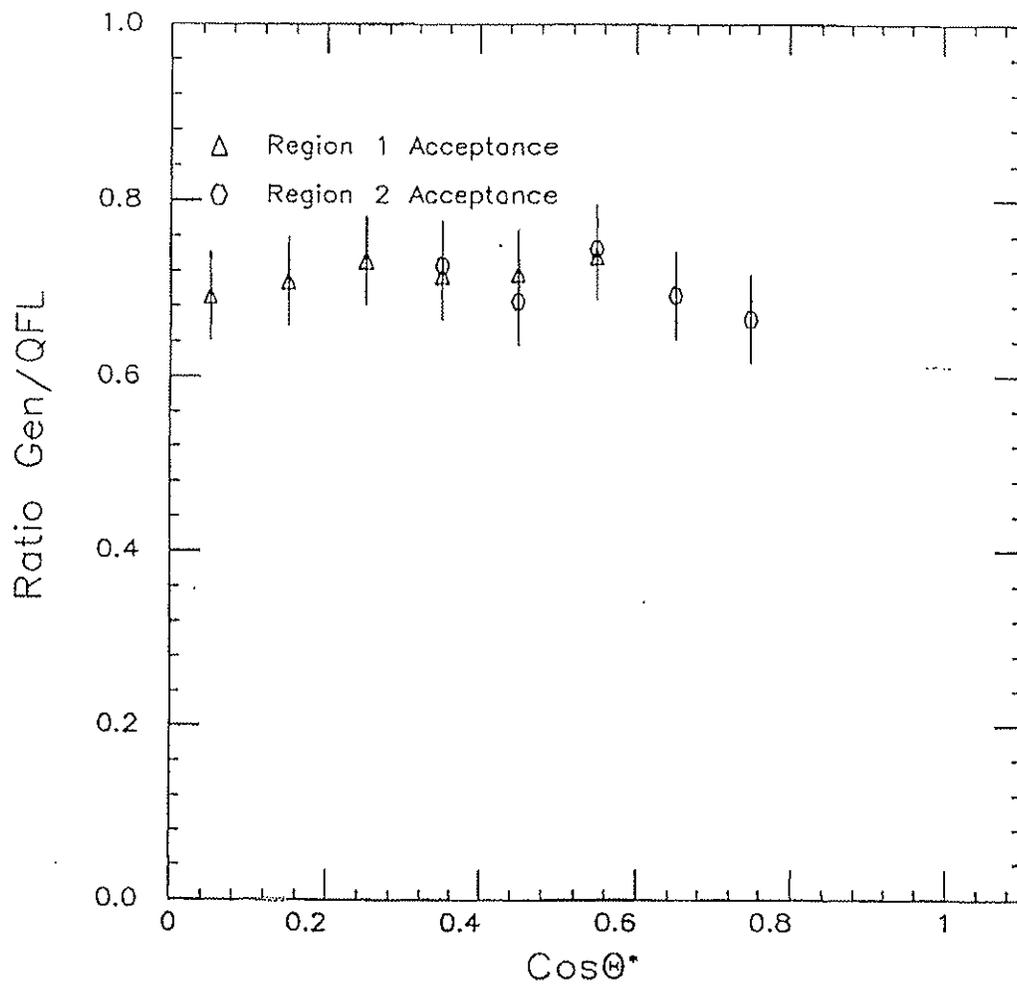
Figure 6.8: η Acceptance from MC Simulation. Jet P_T >10 GeV. Acceptance is flat. Each bin is the ratio of the MC generated cross section over the MC 'measured' cross section after simulation with QFL.

Sample	$\cos\theta^*$	γ's	Stat	Trig	Acc	Eff	Norm	Tot
P23 SUMJ	.05	147.9	28.23	1.43	5.92	6.57	17.93	34.73
	.15	131.2	29.40	1.55	5.25	3.88	15.90	34.09
	.25	129.2	28.08	1.49	5.17	2.69	15.66	32.71
	.35	124.6	27.59	1.45	4.98	5.65	15.10	32.37
	.45	129.0	32.60	2.90	5.16	21.04	15.63	42.25
	.55	250.2	43.73	15.66	10.01	17.94	30.33	59.16
	.65	95.6	20.73	1.13	4.30	3.29	25.51	33.33
	.75	164.4	33.52	9.67	7.41	6.80	43.91	56.98
P23 LeadJ	.05	126.9	31.83	1.23	5.08	15.65	14.64	38.73
	.15	179.6	28.33	1.64	7.18	17.56	20.70	39.93
	.25	142.1	29.31	1.46	5.69	1.91	16.38	34.14
	.35	145.2	29.53	2.23	5.80	1.65	16.74	34.55
	.45	127.5	33.09	4.26	5.10	19.25	14.70	41.55
	.55	264.6	47.76	16.81	10.58	13.33	30.50	61.52
	.65	94.8	20.11	1.15	4.27	16.61	30.35	40.26
	.75	118.5	30.25	4.39	5.33	29.06	37.92	56.96

Table 6.3: Sources of P23 Error. Stat are statistical errors only, Trig, χ^2 Eff, and Norm are the systematic errors due to uncertainties in the trigger efficiency, χ^2 efficiency and normalization respectively. The Total is the uncertainty of all errors added in quadrature.

boundary).

The data reflected the same falloff in the last bin and with the same 15% correction as predicted by the MC; the normalized $\cos\theta^*$ distributions were identical from the 10 GeV and 15 GeV cuts. From this we conclude that the jets from $10 < P_T < 15$ GeV are mostly real and we suffer no ill effects from falsely clustered events in this range. This is not a surprising result for the P23 sample as the lead jets should mostly be considerably above 15 GeV; however this is a much larger effect in the P10 sample where you expect jets with P_T's around 10 GeV. This causes us to regulate the P10 sample to an appendix. Since the acceptance in the P23 sample is flat we assign a flat uncertainty of 4.5% which is roughly the largest excursion with the jet cut set at $P_T > 10$ GeV.

Detector Acceptance
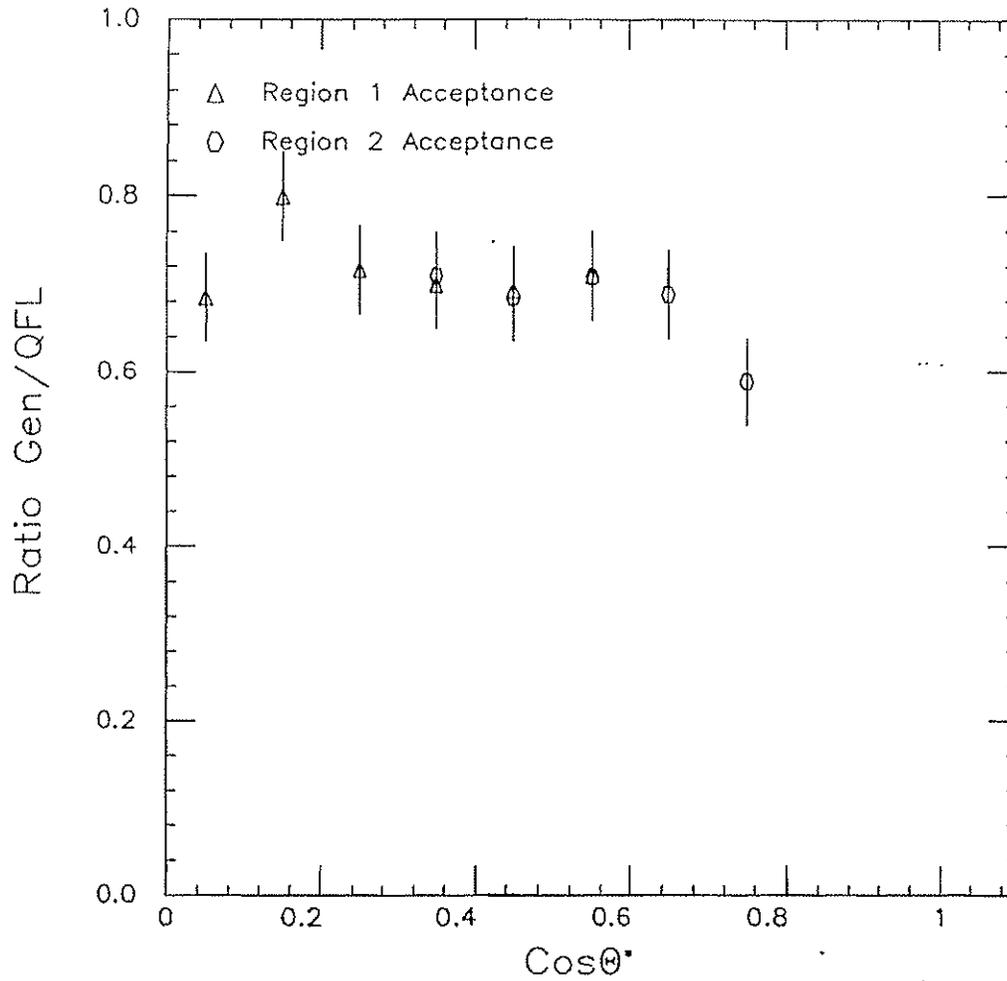
Figure 6.9: η Acceptance from MC Simulation. Jet $P_T > 15\text{GeV}$. Acceptance falls off by 15% in the last bin due to effects from the 30° crack. This is also reflected in the data when the 15GeV cut is used.

106

Chapter 7

Summary of Results and

Conclusions

The center-of-mass angular distribution for direct photon events has been measured for hadronic collisions at $\sqrt{1.8}$ TeV by the CDF detector at FNAL for photons with $26.7 < P^* < 47.0$ GeV. The CM angle was measured two different ways, first by considering the photon and only the lead jet of an event and secondly by considering the photon and a summed jet, formed by the vector sum of all jets with a $P_T > 10$GeV of corrected energy found in the opposite hemisphere from the photon. The angular distributions from both methods were not found to be statistically different and were compared to LO and NLO QCD calculations. The data were found to compare quite favorably with the direct photon predictions and not at all favorably to the dijet angular distribution which was more peaked at shallow angles ($\sin^{-4}\theta^*$ compared to $\sin^{-2}\theta^*$) than the direct photon prediction. The NLO prediction compares slightly more favorably to the data than the LO prediction

107

(especially without the addition of a K_T kick); however they are not separable at the 2σ level with the data and so the LO prediction is not excluded.

The application of cuts on the data designed to make the acceptance flat in η and momentum, necessitated by a trigger selection performed in lab variables, further reduced a statistically limited sample. The method for background subtraction (utilizing EM shower profiles) requires a fairly statistically robust data sample and so the measurement is limited by the statistics of the current data set. A new data run with a better trigger and more luminosity should greatly enhance the statistics available for such a measurement allowing more precise comparisons to LO and NLO QCD calculations. The current measurement demonstrates that the CM angular distribution between direct photon and dijet events are quite different, allowing the angular distribution to be exploited as a means of distinguishing between the two different QCD subprocesses.

Appendix A

Angular Dependence of the

Matrix Elements

In this appendix we demonstrate the angular dependence of the matrix elements discussed in Chapter 1 and show that the predominant center of mass angular distribution is $\sim \sin^{-4}\left(\frac{\theta^*}{2}\right)$ and $\sim \sin^{-2}\left(\frac{\theta^*}{2}\right)$ for the leading order jet and direct photon subprocesses respectively.

A.1   The Matrix Elements

The individual subprocess cross sections $\left(\frac{d\hat{\sigma}_{ij}}{d\Omega}\text{'s}\right)$ referred to in equation 2.1 are related to the matrix elements M via:

$$(A.1) \qquad\qquad \frac{d\hat{\sigma}_{ij}}{d\Omega} = C \mid M_{ij} \mid^2$$

where C is some constant.

Direct Photon		DiJets	
Process	$\mid M \mid^2$	Process	$\mid M \mid^2$
$gq \to \gamma q$	$-\frac{e^2}{3}\left(\frac{\hat{u}}{\hat{s}} + \frac{\hat{s}}{\hat{u}}\right)$	$qg \to qg$	$-\frac{4}{9}\left(\frac{\hat{u}}{\hat{s}} + \frac{\hat{s}}{\hat{u}}\right) + \left(\frac{\hat{s}^2+\hat{u}^2}{\hat{t}^2}\right)$
$q\bar{q} \to \gamma g$	$\frac{8}{9}e^2\left(\frac{\hat{u}}{\hat{t}} + \frac{\hat{t}}{\hat{u}}\right)$	$gg \to q\bar{q}$	$\frac{1}{6}\left(\frac{\hat{u}}{\hat{t}} + \frac{\hat{t}}{\hat{u}}\right) - \frac{3}{8}\left(\frac{\hat{t}^2+\hat{u}^2}{\hat{s}^2}\right)$
		$gg \to gg$	$\frac{9}{2}\left(3 - \frac{\hat{t}\hat{u}}{\hat{s}^2} - \frac{\hat{s}\hat{u}}{\hat{t}^2} - \frac{\hat{s}\hat{t}}{\hat{u}^2}\right)$

Table A.1: Leading Order Direct Photon and Selected Dijet Matrix Elements. All matrix elements have the quantity $\pi\alpha\alpha_s$ for photons and $\pi\alpha\alpha$ for dijets, factored out.

At sufficiently large Q^2's the matrix elements are directly calculable from perturbative QCD and wholly contain the angular dependence of the cross section is contained within the matrix elements [16]. Subprocesses identified with the aid of Feynman diagrams are grouped by sets of incoming and outgoing partons and summed before squaring to account for interference between indistinguishable subprocesses. The leading order direct photon processes and their matrix elements are listed in Table A.1 in terms of the Mandelstam Variables $\hat{s}$, $\hat{t}$ and $\hat{u}$, which are defined as follows:

$$\hat{s} \equiv (p_1 + p_2)^2 = (p_3 + p_4)^2 = 4p^{*2}$$
$$\hat{t} \equiv (p_1 - p_3)^2 = (p_4 - p_2)^2 = -2p^{*2}\left(1 - \cos\theta^*\right)$$
$$\hat{u} \equiv (p_1 - p_4)^2 = (p_2 - p_3)^2 = -2p^{*2}\left(1 + \cos\theta^*\right)$$

(A.2)

where the p_i's are the four-vector momenta of the incoming(1,2) and outgoing(3,4) particles and p^* is the absolute value of the center of mass three-vector momenta and θ^* the center of mass angle between incoming and outgoing particles.

Also listed are a few selected dijet subprocesses. At Tevatron energies most of the hard scattering occurs between gluons and not quarks, so for simplicity we show only subprocesses

that contain initial state gluons as these processes dominate the cross section. The first and the third processes have terms with $\hat{t}^{-2}$ which corresponds to $(1 - \cos\theta^*)^{-2}$ which through the half angle formula equals $\sin^{-4}\left(\frac{\theta^*}{2}\right)$ as claimed. The direct photon matrix elements only contain terms with $\hat{t}^{-1}$ which go as $\sin^{-2}\left(\frac{\theta^*}{2}\right)$. The terms with the $\hat{t}$ to the inverse second power come from the spin 1 gluon propagator present in the Feynman diagrams from which those terms originate. The single inverse power in $\hat{t}$ come from diagrams with the spin $\frac{1}{2}$ quark propagators. There are no LO direct photon diagrams with gluon propagators as can be see in figure 2.1. The second order diagrams do have terms with gluon propagators particularly in the terms that involve gluon bremstrahlung radiation which is a qualitative explanation for the NLO calculation being more sharply peaked at shallow angles.

It can be seen on closer inspection that the $\sin^{-1}\left(\frac{\theta^*}{2}\right)$ term is singular only at 0 and not at π, however the $\hat{u}^{-1}$ $\left(= \cos^{-2}\left(\frac{\theta^*}{2}\right)\right)$ is singular at π. On even closer inspection it is evident that the total expression for the direct photon and dijet cross sections (if one considers all the matrix elements) are not symmetric in $\hat{t}$ and $\hat{u}$ and therefore the angular distribution is not symmetric. However since there is only one kind of photon that can come either from a quark or an antiquark, it is not possible to tell from whence the photon came and therefore the total angular distribution from both proton and antiproton is symmetric.

Appendix B

Simulation of Photon CES χ^2

The shower profile subtraction method requires an accurate χ^2 distribution for the photons as a function of P_T. Once the photon distribution is known, the background distributions can be obtained by superimposing the multiple photon showers from the physical decay of neutral particles into multiple photons. As shown in Chapter 5, the χ^2's are obtained by comparing 11-channel event profiles to a sample profile, scaled according to P_T. It was originally intended that sample profiles obtained from the test beam electron data would be an adequate representation of the average profile of the photon data taken in B0 and therefore an event photon profile could be simulated by taking a random test beam electron shower from a file and calculating a χ^2. This turned out not to be the case and the frozen test beam electron showers used in the simulation had to be corrected to create a χ^2 distribution more representative of photons.

Here we provide more detail of the strip chamber simulation of photons and a more detailed explanation of the systematic uncertainties. The simulation included differences between electron and photon showers and a correction made for suspected saturation of

the CES wire chambers in the collision hall. Also included at the end of this section are a couple of checks to the simulation available from the data.

B.1 Photon and Electron Shower Differences

As described in Chapters 2 and 5, particle identification and measurement ultimately depend upon the detection of charged particles. The essential difference between photon and electron showers comes from the fact that it is charged particles that are measured in the detectors. Therefore electrons start depositing energy as soon as they enter the calorimeter and photons have to convert to a positron electron pair, at least once, before they start to deposit energy. Hence photon showers are delayed on average by about one radiation length from those of electrons. As long as the shower is fully contained in the CEM, this does not have an effect on the CEM total measured energy since the CEM energy is summed over all of the 30-odd layers of the calorimeter. However the CES is located in a single layer of the CEM, at approximately the position of maximum shower development for electrons. The one radiation length delay for photons does cause a difference in their CES shower profiles. This effect is corrected for using simple shower theory and fits to test beam data with various material thicknesses different from those existing at the detector at B0 [37].

The assumption is made that the delay in shower development for photons causes larger fluctuations in the shower profiles (and consequently higher average χ^2's), since the average number of secondary electrons present at the CES is on average lower from a primary photon than a primary electron. Additionally the shower is not as developed for photons at the CES, and therefore shower shape should be different from the average profile used for

calculating the χ^2 and therefore the average χ^2 should be larger for photons than electrons. This is not corrected for in the simulation but a large systematic uncertainty is added to account for this effect.

B.1.1 Simple Shower Theory

Electromagnetic showers are very well understood and the energy loss at some depth in material can be parameterized reasonably well by the following formulae [40]:

$$(B.1) \qquad\qquad \frac{1}{E_0} \frac{dE}{dt} = \frac{Ab(bt)^{bt_{max}} \exp^{-bt}}{\Gamma(bt_{max})}$$

where E_0 is the energy of the electron or photon, A is an arbitrary normalization, t is depth in radiation lengths (position of the CES), b is a parameter that is dependent on the calorimeter material (lead in CEM) and t_{max} in the position of maximum shower development (shower max) which is given by:

$$(B.2) \qquad\qquad t_{max} = \ln\left(\frac{E_0}{E_c}\right) + C_i$$

where E_c is the critical energy of the material (E_c=9.59 MeV for lead) and C_i is an energy independent shift due to differences in the initiation position of the shower. C_e is -0.5 for electrons. C_γ for photons is derived from the simple argument that on average a photon will travel $\frac{9}{7}$ of a radiation length before converting into two electrons. If each electron has exactly half of the energy of the original photon then t_{max} will be shifted additionally by $\ln\left(\frac{E_0}{2E_c}\right) - \ln\left(\frac{E_0}{E_c}\right) = \ln\left(\frac{1}{2}\right) = -0.69$. Therefore for photons:

114

$$(\text{B.3}) \qquad \Delta t_{\max} = C_\gamma - C_e \approx \frac{9}{7} - 0.69 = 0.60$$

The reference (Particle Data Book) [40] gave a preferred value for $\Delta t_{\max}$ to be 1.0, but this gave a poorer fit to a GEANT simulation between photon and electron showers for the CEM detector [45]. Therefore the calculated value of $\Delta t_{\max}$=0.6 (C_γ=.1) was employed in the simulation and 1.0 (C_γ=0.5) was used as the systematic limit.

The only parameter besides the normalization (A) that was not provided in the reference was the parameter b, which was dependent upon the absorbing material (lead). A parameterization for b however was given and was found from a fit with the normalization (A) using test beam data. Figure B.1 shows the ratio of CES/CEM data for test beam electrons of 5, 10, 25, 50, 100, and 150 GeV and the prediction from equation B.1 allowing the parameterization for b and the normalization to float.

The agreement was found to be quite good. Once the parameterization for energy loss for electrons was obtained the same parameterization can be used for photons with the 0.6 correction for $t_{\max}$.

B.1.2 Correction for Shower Statistics

A parameterization for electron and photon shower differences allows a correction to be made to the calculated χ^2's. On average there is lower energy loss at the CES for photons than electrons so on average there should be fewer secondary electrons depositing the CES signal and therefore the statistical fluctuations should be larger. Therefore on average there should be larger χ^2's for photons than electrons with the same average pulse shape. To put it another way, in order for the χ^2's for photons and electrons to have the same meaningful

CES Response vs. CEM Energy and Shower Theory Fit

⊕ Testbeam Electrons (6.00 X_0)
— Shower Theory Fit with 6.00 X_0
O GEANT Electrons (5.68 X_0)
-- Same Theory with 5.68 X_0
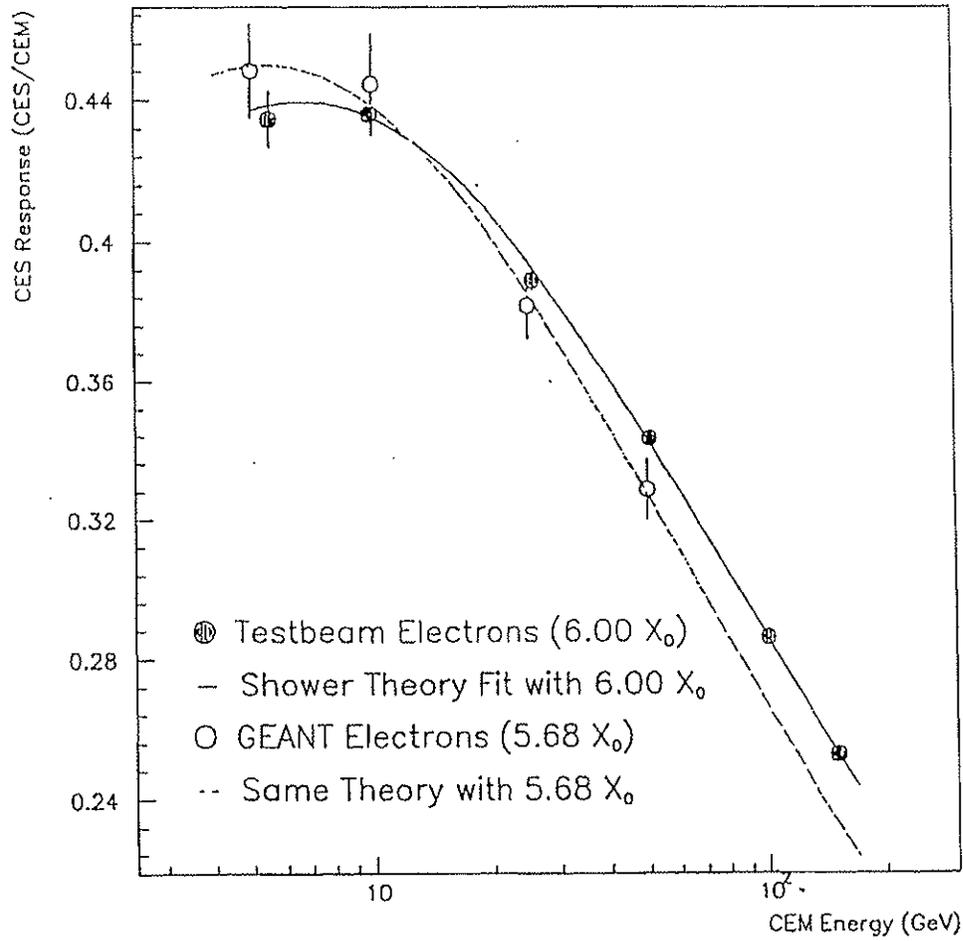
Figure B.1: The CES/CEM Response from Test Beam Data and Predictions from GEANT and Shower Theory. The differences in the GEANT simulation and the test beam data are due to differences in the material thickness in the simulation and the test beam. The Shower theory prediction agrees with both given the material changes.

116

scale (average ~2.5), the σ's in equation 5.1 should be larger for photons than for electrons because of the higher fluctuations for the lower statistic photon showers at the CES depth. Since electron σ's are used in all cases, real photon χ^2's should be correspondingly higher than electrons and a correction was made to the simulation to reflect this.

To make the correction the assumption was made that the fluctuations in an EM shower were directly proportional to the square root of the number of secondary electrons in the shower and that this number was directly proportional to the energy loss (the pulse height) of the shower measured in the CES and predicted by the parameterization shown in B.1 and B.2. Figure B.2 shows this simple model for the number of secondary electrons used above, compared to the actual number of secondary electrons as calculated from a GEANT Monte Carlo simulation. The two models are in good agreement.

B.2 Pulse Height Saturation of the CES

The voltage on the CES PWC's was set higher in B0 during the experimental run than it was during the 1985 test beam where the sample electron profiles were taken. It is believed that the CES voltages were set too high in B0 and there was a problem with pulse heights for both electrons and photons saturating out at high P_T. This would cause the shape of the CES pulses to be distorted and increase the calculated χ^2's for each event. Test beam data was taken in the 1990 test beam at voltages similar to B0. It was observed that the χ^2's got larger with 50 GeV data run at 1470 volts in 1990 test beam data compared with the data taken at 1390 volts with the 1985 data that was used for the χ^2 comparison. There was no change in the χ^2's of 10 GeV data. Since the simulation used 1985 frozen electron

117

CES γ/e Response from GEANT and Shower Theory
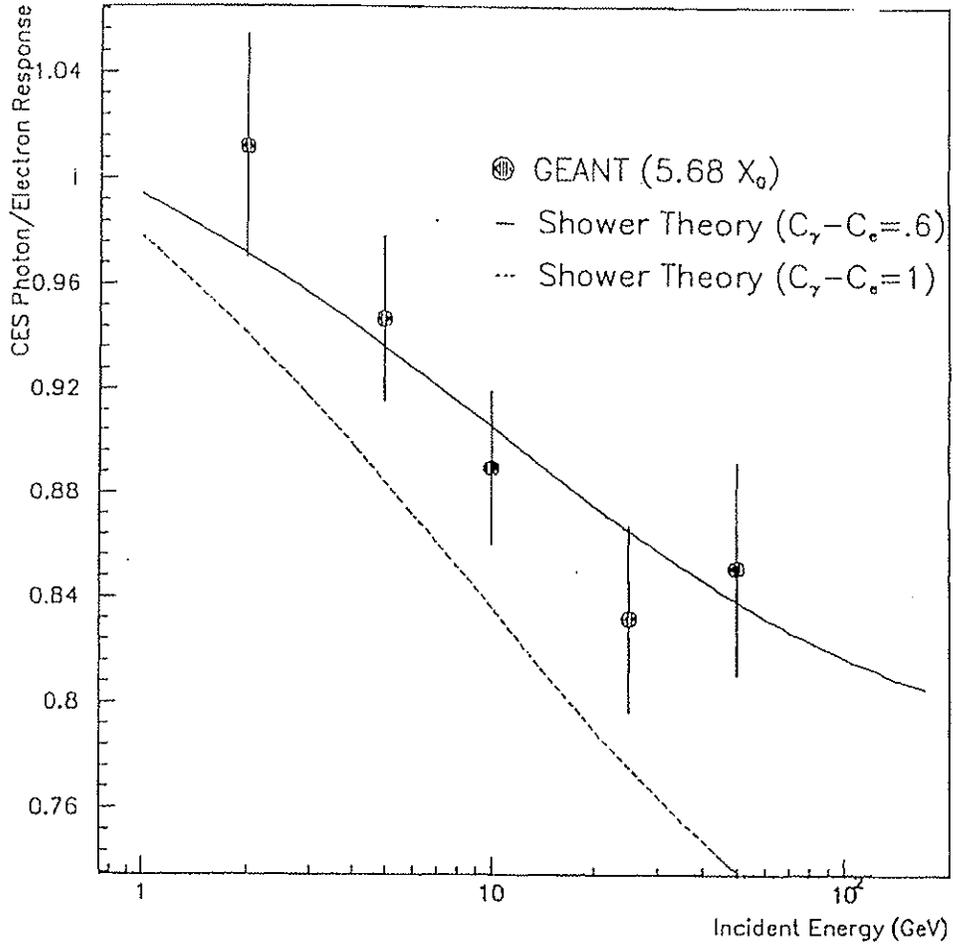
Figure B.2: Number of Shower Electrons from Simple Shower Theory and GEANT. The number of shower electrons at the CES depth as predicted by the simple shower theory model (curves) and with a GEANT simulation (points) for photons divided by the GEANT simulation for electrons. The two shower theory curves show the difference between the value of $\Delta t = 0.6$ and $\Delta t = 1.0$. The 0.6 value was used in the simulation (see text).

showers to simulate electron and photon showers, a correction for this effect was introduced. A multiplier for the χ^2's was introduced to mimic the effect of the χ^2's getting larger from the distortion of the pulse shapes. To obtain the multiplier a variable χ^2_{80} is defined to be the point where 80% of the raw χ^2's are below the cut for test beam electrons (80% efficiency in the language of Chapter 5). The multiplier (K_0), good for 1470 GeV data is given by:

$$(B.4) \qquad K_0 = \frac{\chi^2_{80}(50, 1470)\chi^2_{80}(10, 1390)}{\chi^2_{80}(10, 1470)\chi^2_{80}(50, 1390)}$$

where $\chi^2_{80}(i,j)$ represents data taken at i-GeV and j-CES Voltage. K_0 was measured to be 1.158 ± 0.061 in the strip view and 1.166 ± 0.066 in the wire view. The voltage at B0 for the data was set at 1450 volts $\frac{3}{4}$ of the way from 1390 to 1470 so the multiplier used was for both views was reduced accordingly to K_1 which was:

$$(B.5) \qquad K_1 = 1.12 \pm 0.03$$

This multiplier K_1 is good for 50 GeV data and the effect was assumed linear from zero at 10 GeV so the final multiplier used in the simulation K(E) is given by

$$(B.6) \qquad K = 1 + (K_1 - 1)\frac{E - 10}{E - 50}$$

The net effect of this correction on the efficiency (ϵ) defined in chapter 5 is roughly a linear change of $0.0 - 0.05$ from 10 to 50 GeV. The systematic uncertainty was taken to be the value of the correction.

119

B.3   Systematic Uncertainties

In this section the limits for the systematic uncertainty on the simulation χ^2 efficiencies are reviewed [37]. As mentioned above, the systematic errors taken for the corrections were the value of the correction for CES saturation and the difference between the particle data book value of the difference between electron and photon showers max ($\Delta t_{max} = 1.0$ instead of 0.6). In addition there were a couple of other systematics considered which were added to the total systematic error of the χ^2 efficiencies. The additional effects are detailed below and each of the effects are shown in figure B.3.

B.3.1   Photon Shower Shapes

Since it is believed that the photon shower is not as developed in the CES as an electron shower the CES profiles should be different. Therefore in addition to the effect from strictly shower statistics there should be an additional degradation of the photon χ^2 efficiencies due to the use of an average electron shower profile to calculate the χ^2's instead of an average photon shower profile. Since there was no easy way to obtain a sample photon CES profile (if there were there, would be no need for all this), this effect was not entered in as a correction but rather the systematic error bars were increased instead. The value of the uncertainty was again determined from test beam data where varying amounts of material were placed in front of the CES and χ^2's were calculated for each.

The 1985 test beam data that was used for the standard profile to calculate the χ^2's used 5.68 radiation lengths of material in front of the CES. This was a slight complication because the B0 data were taken with 6.00 radiation lengths. In the 1990 test beam 4

Systematic Uncertainties in Photon χ^2 Efficiency
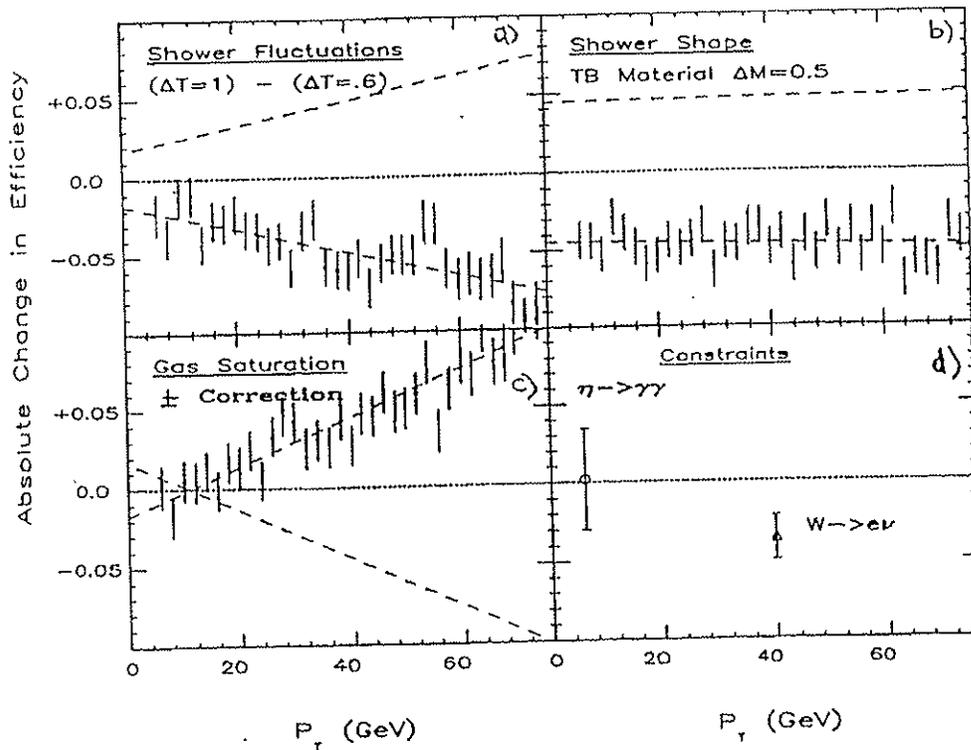
Figure B.3: Systematic Errors in the Background Subtraction as a Function of P_T. The dashed lines are systematic uncertainties, the points are the change in efficiency after the simulation had been varied to account for uncertainties that are discussed in this chapter. The error bars reflect the statistical limits of the simulation.

121

material lengths were tried with 10 GeV electrons and the resulting χ^2 efficiencies can be seen as the open circles in figure B.4.

The efficiencies fall as the material increases and the resulting electron shower profiles differ more and more from the sample profile (labeled STPANA). Unfortunately the test beam was not set up to remove material, only add it, so it was not possible to attempt a replication of a 'photon shower' with 0.6 or 1.0 radiation lengths of material removed. The assumption was made that the effect from shower differences and a sliding CES position in radiation lengths was linear and that the falloff was symmetric in both directions (more or less material). The triangle denotes the position where photons would fall (-0.6 radiation lengths) and the dashed lines delineate where the reasonable systematic uncertainties lie, (no correction or out to -1.0 radiation lengths). The actual uncertainty taken was the point to $+0.6$ away from B0 (6.6 radiation lengths deep). Again, to reiterate, no correction was made in the simulation. The effect was added in as a systematic error only.

B.3.2 Background Mixture

To a first order approximation the background is all from neutral pions and the systematic limits on the χ^2 efficiencies are completely correlated. For example if the signal χ^2's increase (reducing the efficiency) then the background χ^2's will correspondingly increase. However there are backgrounds from neutral η's and K_S^0's so the background efficiency is somewhat dependent upon the exact mixture of isolated neutral particles present in the data. As mentioned in Chapter 5 the most crucial $\frac{\eta}{\pi}$ ratio was measured from the data but was found to be somewhat higher than previous measurements of absolute cross sections (without isolation requirements). In the simulation the value measured from the data were used,

122

Systematic From Photon—Electron Shape Difference
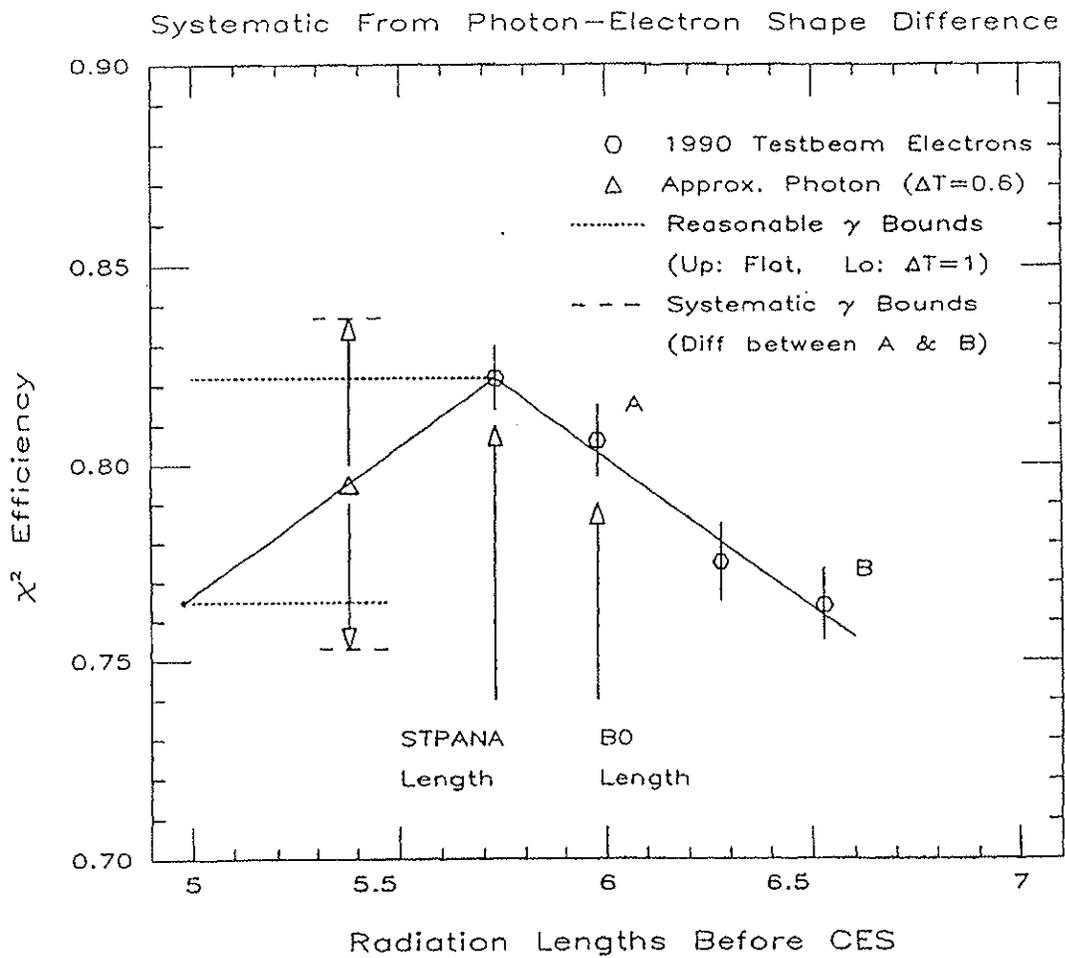
Figure B.4: χ^2 Efficiencies from Test Beam Data for Different Material Thicknesses. The differences between materials was used to obtain systematic limits on the background subtraction.

123

$(\pi^0 : \eta : K_s^0)$=(1.0 : 1.02 : 0.25), and the systematic limit was taken as the production ratios from the literature (1.0 : 0.6 : 0.4).

B.3.3 Jet Fragments in Background

The simulation was performed using single neutral particles sent into the detector simulation (γ's, π^0's, η's, and K_s^0's). In reality while the photons can only emerge from jets in the higher order diagrams, the background are always emerging from a jet and so there is a strong possibility that additional low energy neutral particles may be within the strip cluster and cause a further degradation of the χ^2. This effect was not included in the simulation but was studied using the detector simulation (QFL) and demanding that the fragmentation function generate one stiff neutral particle (>70% of the parton energy); then allowing the remaining energy to fragment normally (using a Feynman-Field model) [44]. The effect was found to be P_T dependent but less than a 0.02 shift in efficiency at worst which is considerably smaller than the other systematics.

B.4 Checks from the Data

The data allowed several checks to the full CES χ^2 simulation. The W sample allowed a check using isolated electrons in the B0 detector. The simulation included radiative corrections to the relatively high P_T electrons ($\sim$ 40 GeV) and allows us a check for the simulation's ability to predict strip and wire χ^2's with both slightly different material (X_0=6.00) and for the saturation effect. The results can be seen in figure B.4 where the points are the data and the histogram the full QFL simulation.

The η meson mass peak shown in Chapter 5 also allowed a direct measurement of photon

124

χ^2's at low P_T. The η's sample was obtained from the direct photon data sample with the isolation cuts on the CEM cluster but by reversing the 2nd strip cluster cut and requiring that there be good CES strip clusters pointing at adjacent towers so the CEM energy from each tower could be used as the measured energy for each photon in constructing the mass. Figure B.5 is the η mass peak reconstructed with 11-channel strip clusters.

The demand of two 11-channel strip clusters suppresses the π^0 mass peak shown in figure 5.5 as the pair of decaying photons from π^0's tend to be within a single 11-channel cluster. The presence of other backgrounds including real photons with two clusters requires a sideband χ^2 subtraction to be performed. The resulting strip χ^2 distribution of now presumed single photons is shown in figure B.7 along with the prediction from simulation. The agreement is quite good. The wire view clusters were not as well separated which prevented a similar plot from being made.

In a similar fashion the decay of $\rho^\pm \to \pi^\pm \pi^0$ could be used to get a sample of known π^0 χ^2's. In this sample the tracking chambers were used to identify the charged pion and its momentum. The CEM energy is used as the energy of the neutral pion. The charged track was required to have $P_T > 0.8$ GeV/c (minimum P_T cut on the charged pion) and the minimum neutral pion energy was limited by the minimum P_T cut (~ 10 GeV). In figure B.6 a clear peak is seen at $\rho^\pm$ mass and after sideband subtraction a χ^2 distribution for presumably pure π^0's can be obtained. The resulting data χ^2 distribution is shown against the simulation curve in figure B.7. Again the agreement is quite good.

It is necessary to point out that the data are able to give only three points of verification for our simulation and only a single background and signal point on the efficiency curves, and then only at low P_T. This is the point where our corrections are the smallest (no CES
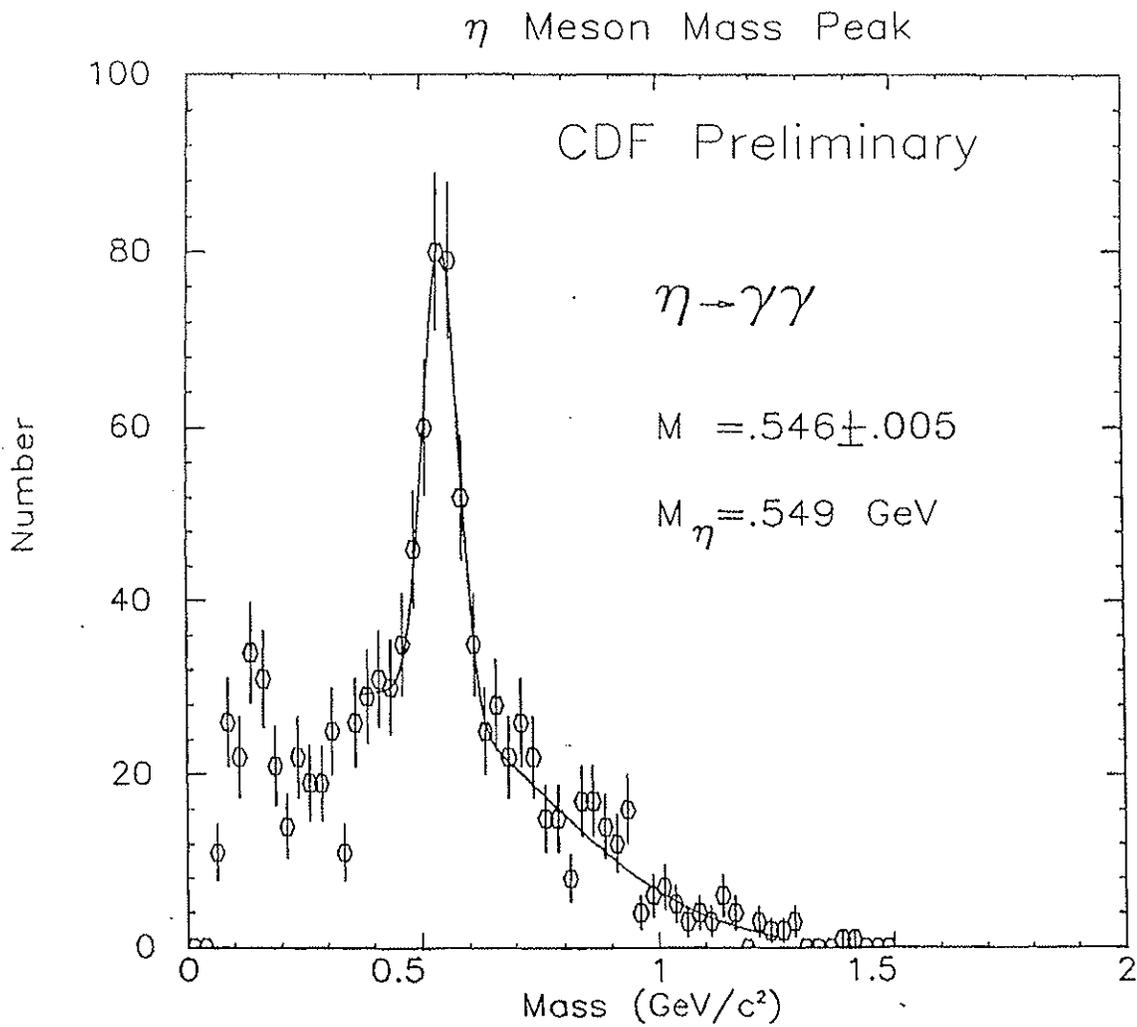
Figure B.5: η Meson Mass Peak Reconstructed from the Data with 11-Channel Strip Clusters. The events within the peak are used to obtain a χ^2 distribution for single isolated photons. M is the mass found from a fit to the peak M_η is the mass given in the PDGB [40].
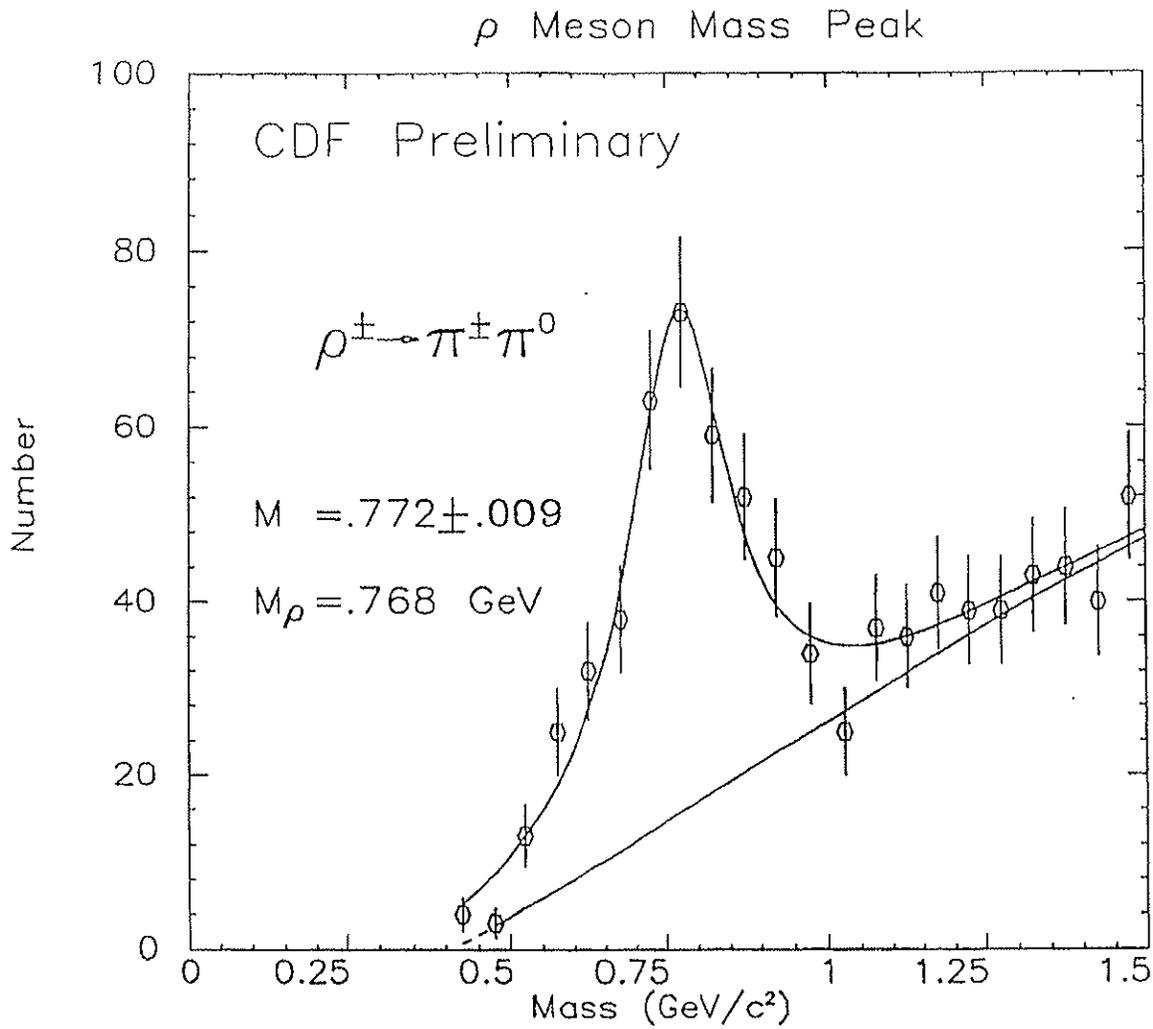
Figure B.6: ρ Meson Mass Peak from Direct Photon Data. Events within the peak are used to obtained a χ^2 distribution for π^0's. M is the mass found from a fit to the peak M_ρ is the mass given in the PDGB [40].

pulse saturation at all) so it is not the best of verifications. The W electrons do however test the overall simulation, including CES saturation, and together the three points do all agree well and indicate that the simulation if not perfect, is at least on the right track.
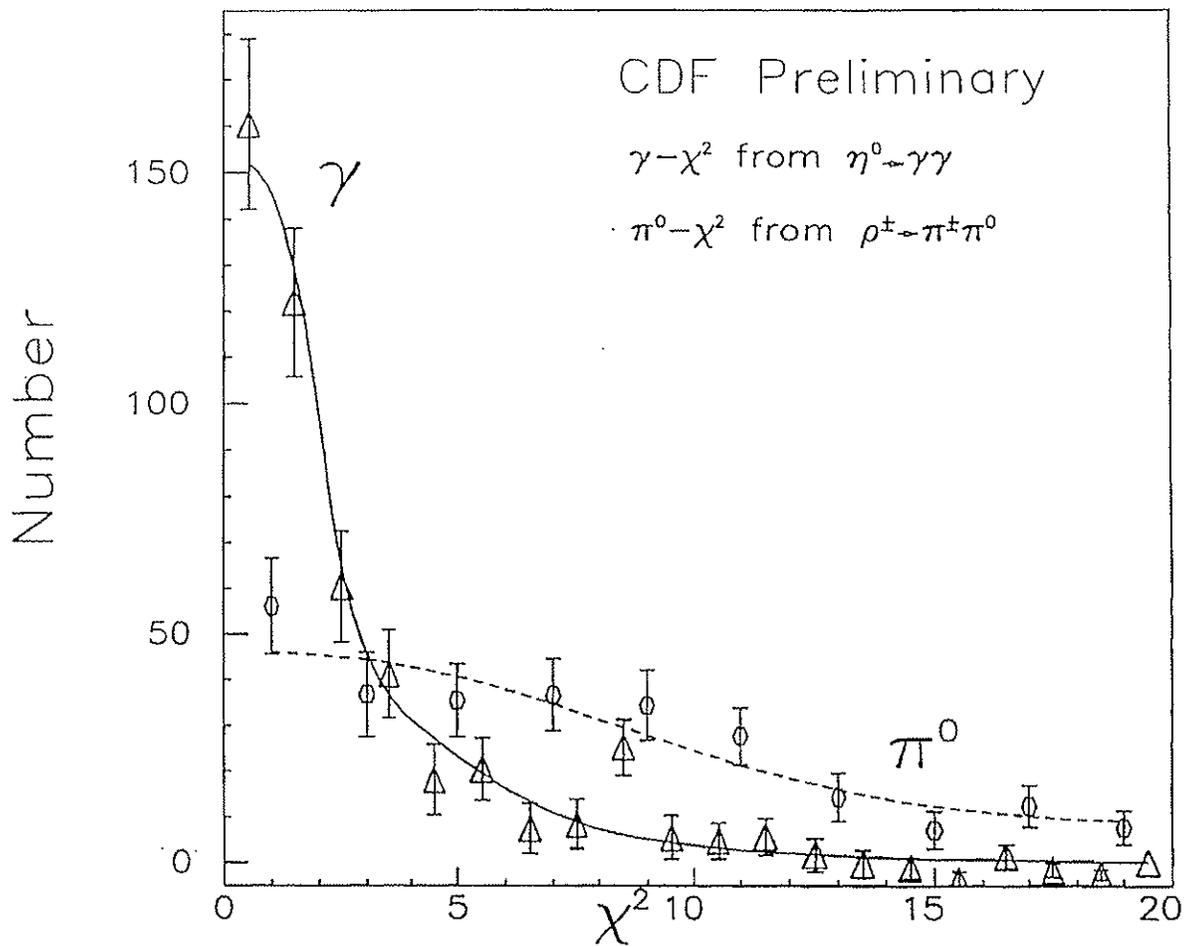
Figure B.7: χ^2 Distribution for γ's and π^0's from the Data. Data distributions are shown against the simulation distributions for each. Note that these events all have low P_T.

Appendix C

Photon-Jet Balancing

As mentioned in Chapter 2, there is usually very little initial momentum transverse to the beamline ($\sim$ 200MeV) so the total energy of an event should sum to zero in the transverse direction. Any imbalance in the total transverse vector momentum of an event (denoted as $\vec{k}_T$ by the UA2 collaboration where it was first introduced)[46] is due to imperfect detector resolution or effects from the underlying event. Here underlying event refers to the effects of the spectator partons and initial state gluon bremstrahlung radiation that are not directly associated with the hard-scattering partons and are not included in current QCD calculations [1].

If there were no initial state radiation and no interacting spectator partons then $\vec{k}_T$ would necessarily be zero for an event (modulo the $\sim$ 200MeV) and a 2 final state particle (photon-jet) system would be back to back (180 degrees apart) in the transverse plane. In

---

[1] There is always a little uncertainty in what is meant by 'underlying event'. The theoretical definition is given here and is usually the definition referred to in most contexts when there is an unambiguous origin for a particle. Experimentally it is not possible to tell with certainty where something came from so usually in the context of a measurement we mean unclustered energy when we say 'underlying event'.

practice some of the transverse momentum of an event can be absorbed by the underlying event and even with a perfect detector the events would not balance in ϕ. Since the K_T 'kick' given to the hard interaction is not associated with it, the resulting system of the hard interaction should be randomly boosted from its transversely balanced state.

Consider the 2 state final system shown in figure C.1, drawn in the transverse plane.

Detector resolution alone affects only the relative measured energies of the two final states, which are the measured lengths of the vectors. Detector resolution will not affect the angle ϕ between them. The component along the perpendicular bisector between the two final state particles ($K_{T\perp}$) is only affected by the kick from the underlying event and the orthogonal component ($K_{T\parallel}$) by both detector resolution and kick. In principle since the underlying event is not associated with the hard scattering event, the parallel component of the underlying event should only add an additional smearing to the energy. Therefore if the average of the measured parallel component in the data is not zero, the offset should be due either to energy lost in the detectors or an energy calibration problem. This is of potentially great use because the photons only shower electromagnetically and are measured with the CEM, the best calorimeter available in the detector. By studying the parallel component of the $\vec{k}_T$ of the central photon against, a central jet, plug jet and forward jet away from known calorimeter cracks, the relative energy scale of all the hadronic calorimeters can be checked. In practice the limited statistics for the jets in the non-central regions limited the studies to the central region. Additionally the perpendicular component of the photon can be used to determine the average contribution of P_T coming from the underlying event.

In principle the method is completely unambiguous and theoretically there are only partons in, partons out, and a $2 \to 2$ system is well defined. Experimentally only energy
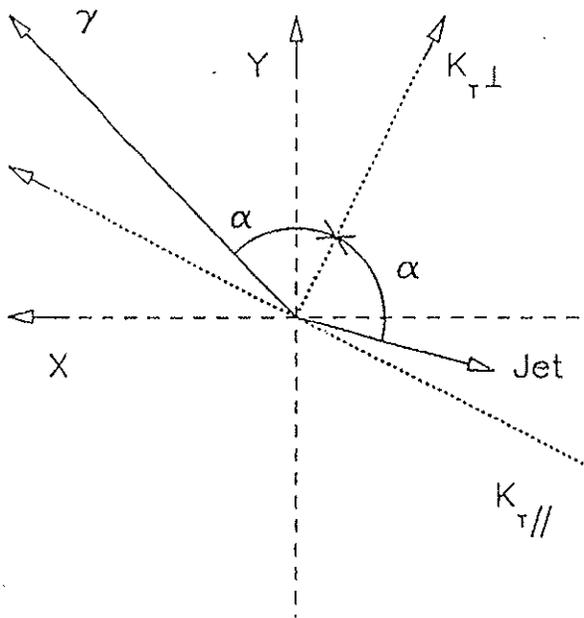
K_T Plane(X−Y)

Figure C.1: The K_T System. The component along the perpendicular bisector $K_{T\perp}$ is affected only by a transverse momentum 'kick' originating from the underlying event or initial state gluon radiation. The orthogonal component $L_{T\parallel}$ is affected by both the 'kick' and detector resolution effects.

deposition from real particles is measured and one cannot tell which particles come from the hard interactions and which are from the so-called underlying event. There are also higher order processes with more than a single outgoing parton and there is always the unresolvable question as to what constitutes a low P_T jet (from an outgoing parton) and what is the underlying event. In practice jets are defined with clusters and minimum P_T cuts. Misidentifying a multijet event as a $2 \rightarrow 2$ process or clustered underlying event energy as the jet could cause an offset even if detector resolution were perfect, so one must take special care.

The trigger threshold and the rapidly falling P_T spectrum add a last complication. The kick from the underlying event should be randomly oriented with respect to the photon-jet axis since there is very little coupling between the two. If the P_T spectrum were flat, this would translate into a gaussian type contribution to the measured P_T from the kick, centered at zero. Within a given *measured* P_T bin, the relative direction of the kick is random, therefore assuming that the magnitude of the kick is adequately described by a gaussian, the 'true' (unkicked) P_T distribution of the photons would also be a gaussian centered on the measured P_T bin. However, a rapidly falling spectrum causes a feeddown effect that distorts the gaussianlike shape and the mean of the inferred 'true' P_T distribution. The resulting measured spectrum is a convolution of a falling spectrum and a gaussian which is itself non-gaussian. This results in a situation where in a given *measured* bin of P_T it is far more likely that the *true* P_T of the photon was lower than the measured P_T. This is because even though the resolution is gaussianlike, there are far more events that can feed up (in P_T) rather than feed down. This means that when considering a given bin of P_T, the K_T kick is not likely to be random to the photon-jet axis but rather preferentially aligned

with the trigger photon direction and therefore the $K_{T\parallel}$ component would not be expected to balance over any P_T range, even with a perfect detector. However all is not lost. One only has to be careful to model the $K_{T\perp}$ component with a falling spectrum and be sure to include the net effect of the resulting kick in the simulation of the parallel component to study detector effects.

C.1 P_T from Underlying Event

Here the projection of the K_T kick along $K_{T\perp}$, which is $\vec{P}_{T\gamma} \cdot \hat{k}_T$, is determined from the data. In order to do this we run a Monte Carlo calorimeter simulation with a rapidly falling spectrum and introduce a gaussian kick with a random direction and attempt to match the $K_{T\perp}$ projection of the data, allowing the σ of the kick to be a free parameter. The program papageno [19] was used as the event generator for the detector simulation QFL [29]. QFL is a fast detector simulation that reproduces single particle response for all the calorimeter systems, including detector cracks, but saves CPU time by employing preprogrammed average responses for tracking simulation. We found a good fit to the data with the use of two gaussians, 75% 3.5 GeV and 25% 5.0 GeV, which was considerably lower than the 75% 9.0 GeV and 25% 4.0 GeV that was measured for dijet data in the 1987 data set. This is not surprising considering that the dijet data were taken from a higher Q^2 region. To get good statistics with a falling spectrum in each data region two samples of MC were generated, one with $P_{T\gamma} > 10$ GeV (for the P10) and a second with $P_{T\gamma} > 20$ GeV (for the P23), both with the 75%-3.5 and 25%-5.0 GeV kick. The uncorrected and unsubtracted P_T spectra for the photon and the lead jet are shown for both the P10 data

134

and the MC simulation in figures C.2 and C.3. The good agreement in the shape of the spectra imply that both the falling P_T spectrum and the detector response for jets is well reproduced by the MC.

The $K_{T\perp}$ is shown in figure C.4 cut for a $16 < P_T < 27$ GeV and with $\mid \eta_{jet} \mid < 0.8$ (central) and with the P_T of the second jet less than 5.0 GeV in order to suppress higher order events.

The uncorrected and unsubtracted P23 data is shown in C.5-C.7 with the same cuts but with $27 < P_T < 60$ GeV and is still adequately reproduced with the MC in the same P_T range as the P23 data and with the same K_T kick as the P10 data.

The $K_{T\perp}$ component of the data is also shown in figures C.8 and C.9 without the cut on the 2nd jet P_T.

The presence of jets with significant P_T (>5.0 GeV uncorrected) manifests itself as a somewhat larger average $K_{T\perp}$ and a wider distribution (*i.e.* a larger offset from zero and a larger standard deviation). Without the second jet cut the simulation is not as good and it appears as if a larger K_T kick may be in order. However we prefer to assign to K_T only the average component that we can not assign to higher order gluon radiation as the latter is not in the simulation. The overall difference between the measured K_T with and without a second jet cut is not that large and most significantly the K_T kick is small in any case, small compared to the jet energy resolution which is roughly 20% at 25 GeV where the K_T kick is only 3.5 GeV or so. The effect of the kick is seen in figure C.10 where the $K_{T\parallel}$ component of the simulation is shown with and without the kick measured from the data above. The means of the two MC distributions, kicked and unkicked, are 7.4 and 6.5 GeV, with RMS's of (4.5 and 3.7) respectively. Therefore the effect of the kick is an offset of

135

Figure C.2: $P_{T\gamma}$ for P10 Data and MC. $16 < P_{T\gamma} < 27$ GeV, MC generated with $P_{T\gamma} > 10$ GeV.

136

γ vs. Lead Jet : P10 Data vs. QFL—V3.10

CDF Preliminary

○ Data P10 16<Ptγ<27GeV

◊ Papageno—QFL—V3.10 16<Ptγ<27GeV

KtKick (.75)3.5GeV (.25)5.0 GeV
Papageno generated Ptγ>10GeV

PtJ1 All Detector $|\eta_\gamma| < 0.8$
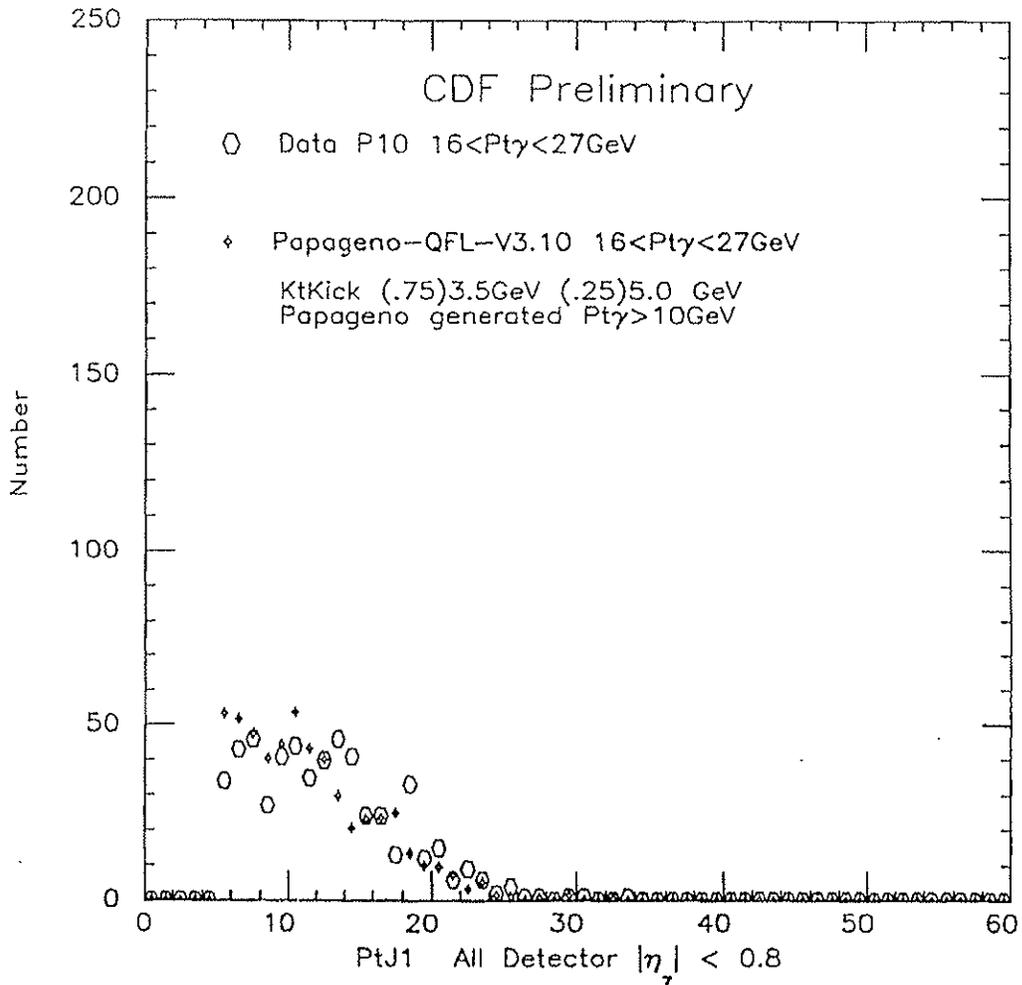
Figure C.3: $P_{T\text{jet}}$ for P10 Data and MC. $16 < P_{T\gamma} < 27$ GeV, MC generated with $P_{T\gamma} > 10$ GeV.

137
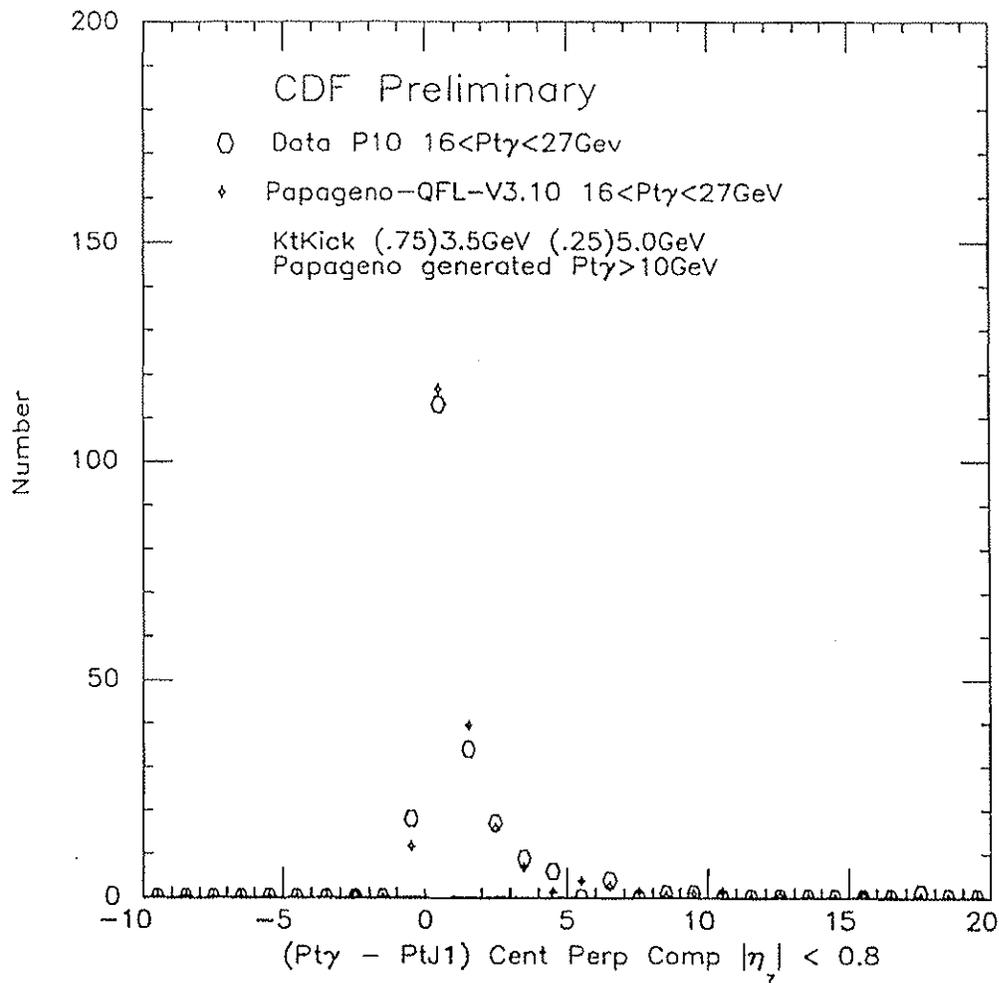
Figure C.4: $K_{T\perp}$ for the P10 Data and as Reproduced from MC. $16 < P_{T\gamma} < 27$ GeV. The second jet $P_{T\text{jet}} < 5$ GeV and $| \eta_{\text{jet}} | < 0.8$.

138

Figure C.5: $P_{T\gamma}$ for P23 Data and MC. $27 < P_{T\gamma} < 60$ GeV. MC generated with $P_{T\gamma} > 20$ GeV.

Figure C.6: P_{Tjet} for P23 Data and MC. $27 < P_{T\gamma} < 60$ GeV. MC generated with $P_{T\gamma} > 20$ GeV.

γ vs. Lead Jet : P23 Data vs. QFL—V3.10

CDF Preliminary

O   Data P23 27<Ptγ<60GeV

◊   Papageno—QFL—V3.10 27<Ptγ<60GeV

KtKick (.75)3.5GeV (.25)5.0GeV
Papageno generated Ptγ>20GeV

(Ptγ — PtJ1) Cent Perp Comp $|\eta_\gamma|$ < 0.8
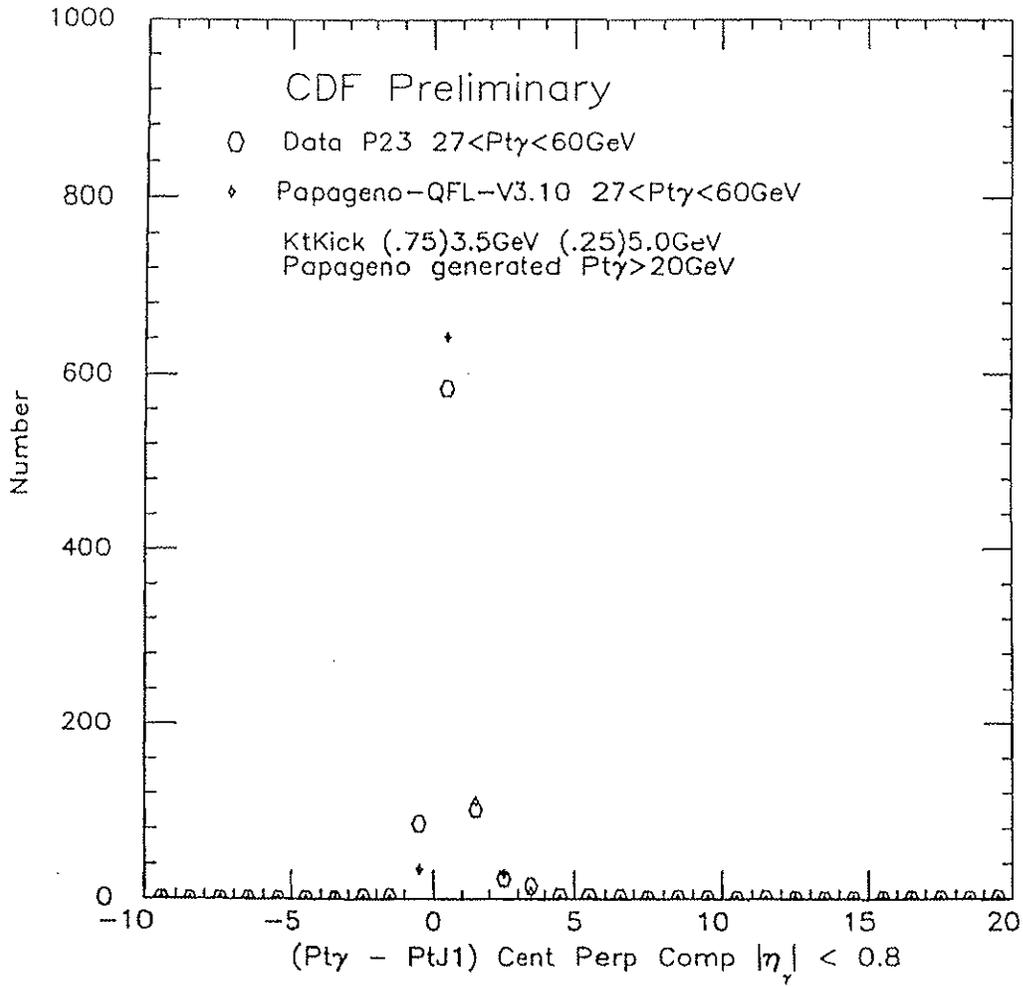
Figure C.7: $K_{T\perp}$ for P23 Data and MC. $27 < P_{T\gamma} < 60$ GeV, The second jet $P_{Tjet} < 5$ GeV and $|\eta_{jet}| < 0.8$.

Figure C.8: $K_{T\perp}$ for P10 Data, No Second Jet Cut.

P23 Data vs. QFL—V3.10, No2JCut

CDF Preliminary

◊ Data P23 27<Ptγ<60GeV

◊ Papageno—QFL—V3.10 27<Ptγ<60GeV

KtKick (.75)3.5GeV (.25)5.0GeV
Papageno generated Ptγ>20GeV

(Ptγ — PtJ1) Cent Perp Comp $|\eta_\gamma| < 0.8$
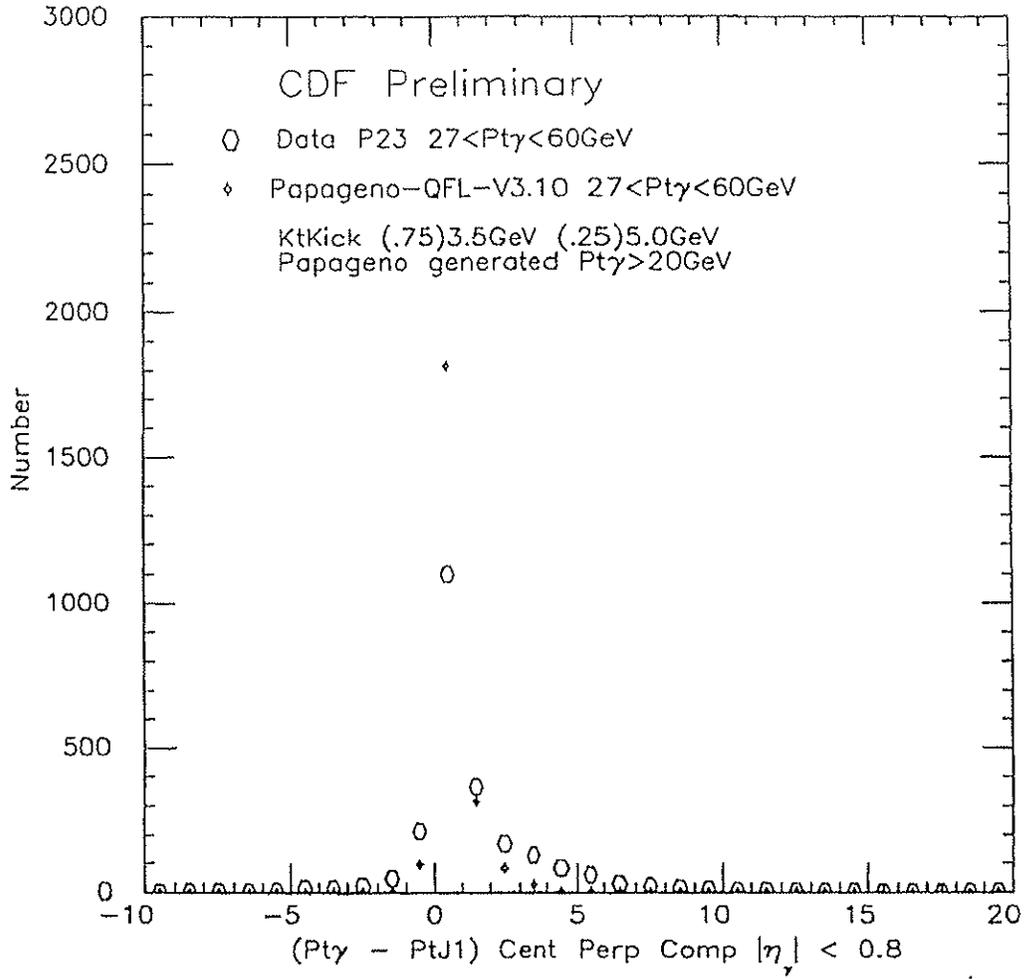
Figure C.9: $K_{T\perp}$ for P23 Data, No Second Jet Cut.

143

about a GeV and a slight widening of the energy resolution smear of ~20%.

This offset is the effect of the K_T kick on the data.

C.2   Jet Energy Measurements

Assuming that the kick of the system provided by the underlying event is represented adequately *via* its $K_{T\perp}$ component we can use the $K_{T\parallel}$ component to check both the simulation and the jet energy corrections. Figure C.11 is a plot of the $K_{T\parallel}$ for the simulation and the P10 data without corrections.

Assuming there is no K_T kick, the offset of the data (from zero) reflects the energy scale of the detector and the width of the distribution is roughly from the effects of detector resolution. The rough agreement between the simulation and the data in the offset and the width of the distribution before corrections is a good indication that the simulation (with K_T) is doing an adequate job of representing the data. The offset of the peak from zero is not perfectly reproduced (data mean is 6.5 to 7.4 GeV for the MC), but it is within about a GeV and the widths are very well reproduced (RMS of 4.4 to 4.5). Figure C.12 is the data shown after corrections to the jet and EM cluster energies have been applied and the offset has properly gone to zero (mean of 0.4 for the data and 1.4 for the MC) [47], [48]. Figures C.13 and C.14 are the same plots for the P23 data. The offset from zero in figure C.13 is not perfectly reproduced by the MC; the MC predicts a slightly larger offset than is seen. The difference is about 2 GeV, but again the widths are reproduced much better. This implies that the energy scale of the detector is slightly off in the MC (or perhaps the simulation of detector cracks). The K_T kick could contribute some of the effect, but as

144
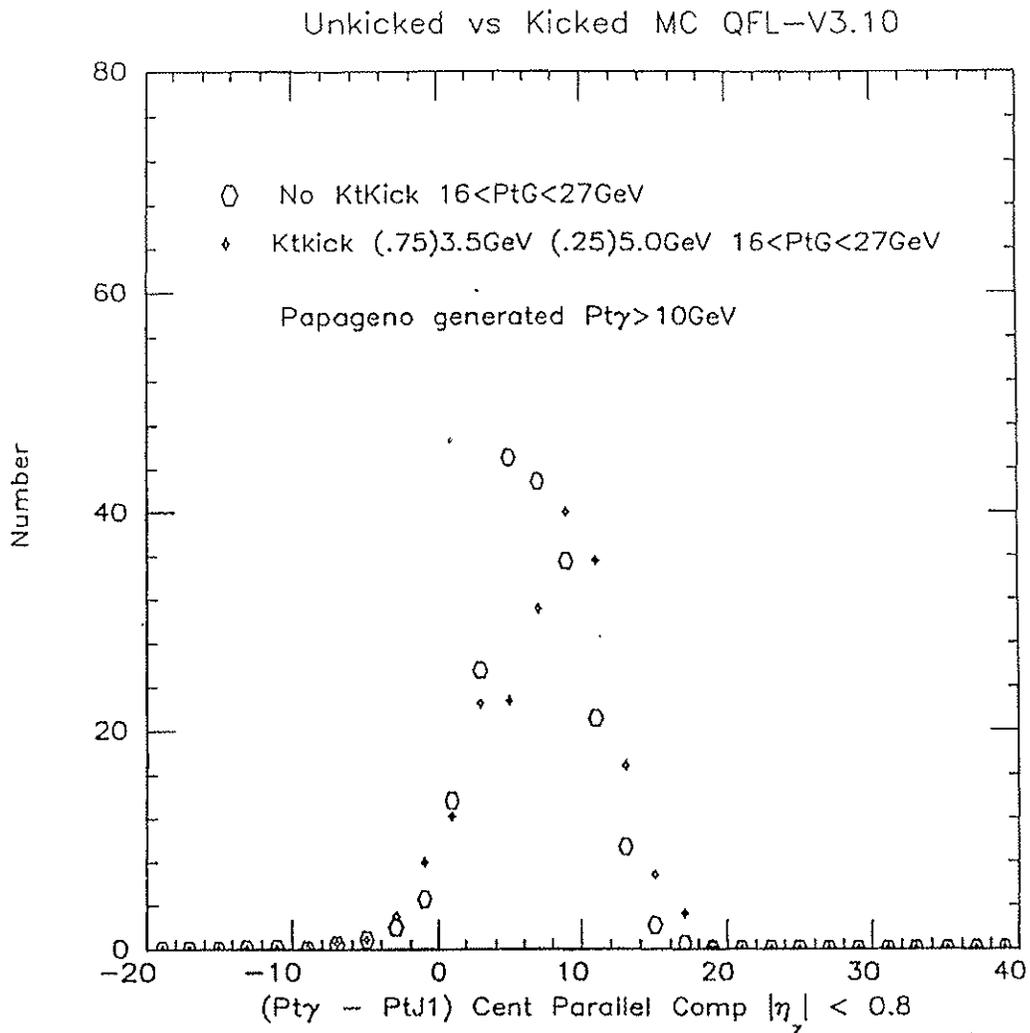
Figure C.10: $K_{T\parallel}$ for the MC Data With and Without the K_T 'kick'. The Mean and RMS's for the distributions are 7.5 and 4.5 GeV for the kicked and 6.4 and 3.7 GeV for the unkicked MC respectively.
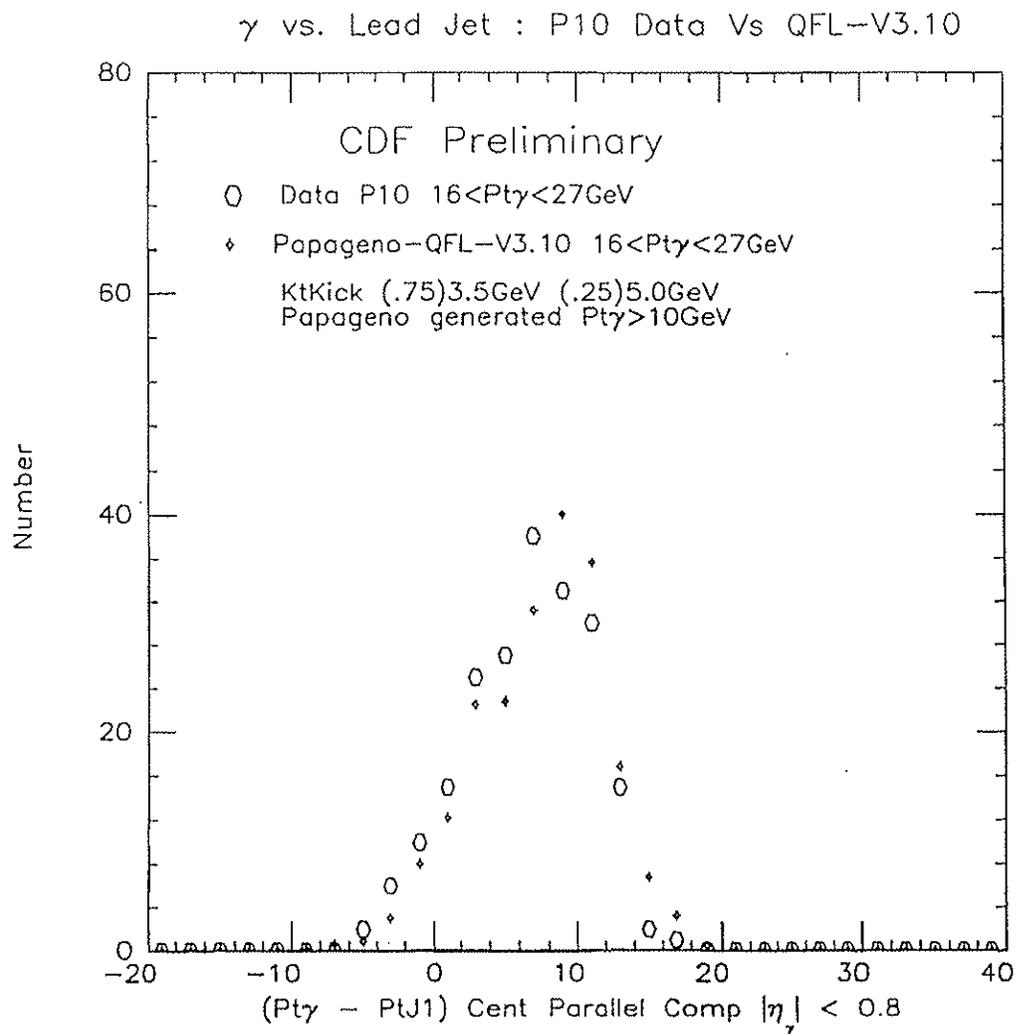
Figure C.11: $K_{T\parallel}$ Component for P10 Data and MC Simulation Without Jet Corrections. $16 < P_{T\gamma} < 27$ GeV and the second jet $P_{T\text{jet}} < 5$ GeV. The mean and RMS's for the distributions are 6.5 and 4.4 GeV for the data and 7.5 and 4.5 GeV for the MC respectively.

146
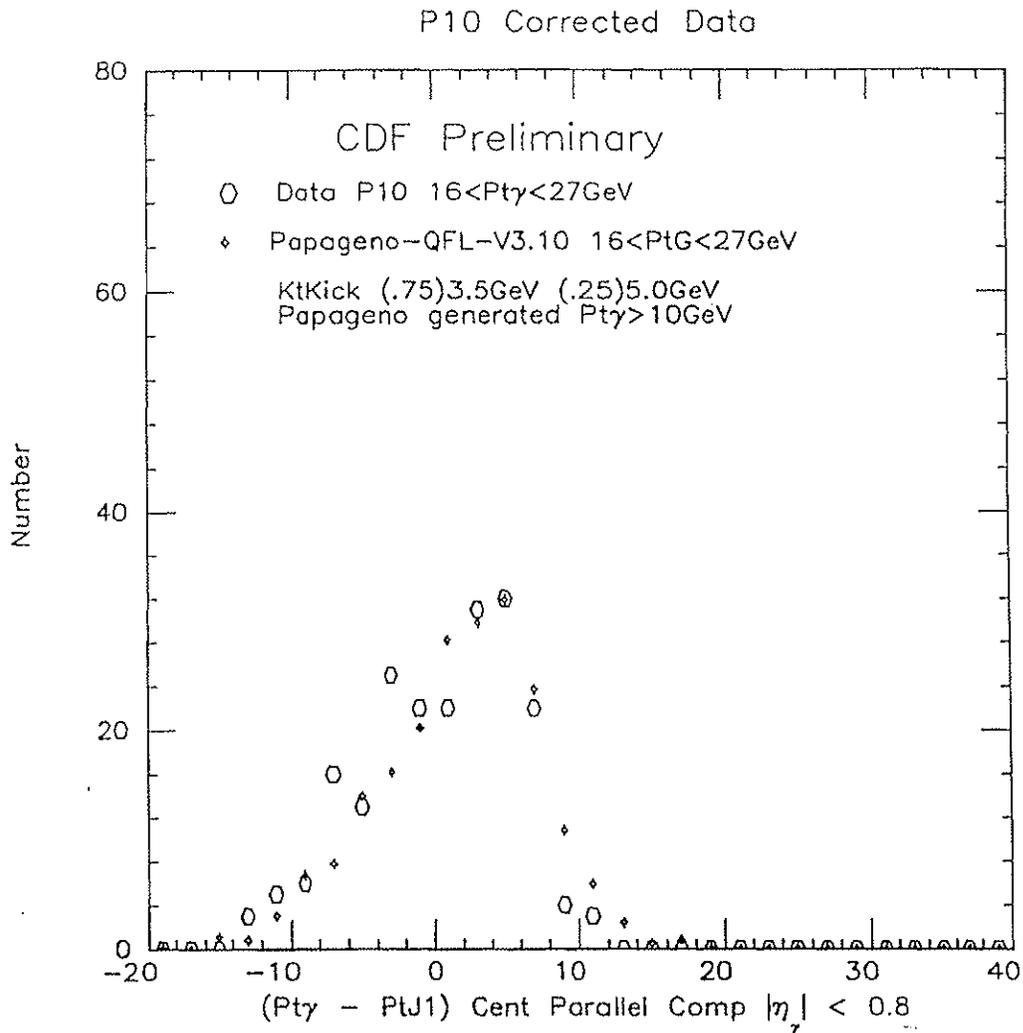
Figure C.12: $K_{T\parallel}$ Component for P10 data and MC Simulation After Jet Corrections. $16 < P_{T\gamma} < 27$ GeV and the second Jet $P_{Tjet} < 5$ GeV. The mean and RMS's for the distributions are 0.4 and 5.3 GeV for the data and 5.5 and 1.6 GeV for the MC respectively.

147

shown above, it could be at most only about a GeV. In any case the difference is not too large (less than 2 GeV) which at 27 GeV is $\sim$7% effect and the energy resolution of the central hadron detector is well reproduced by the MC.
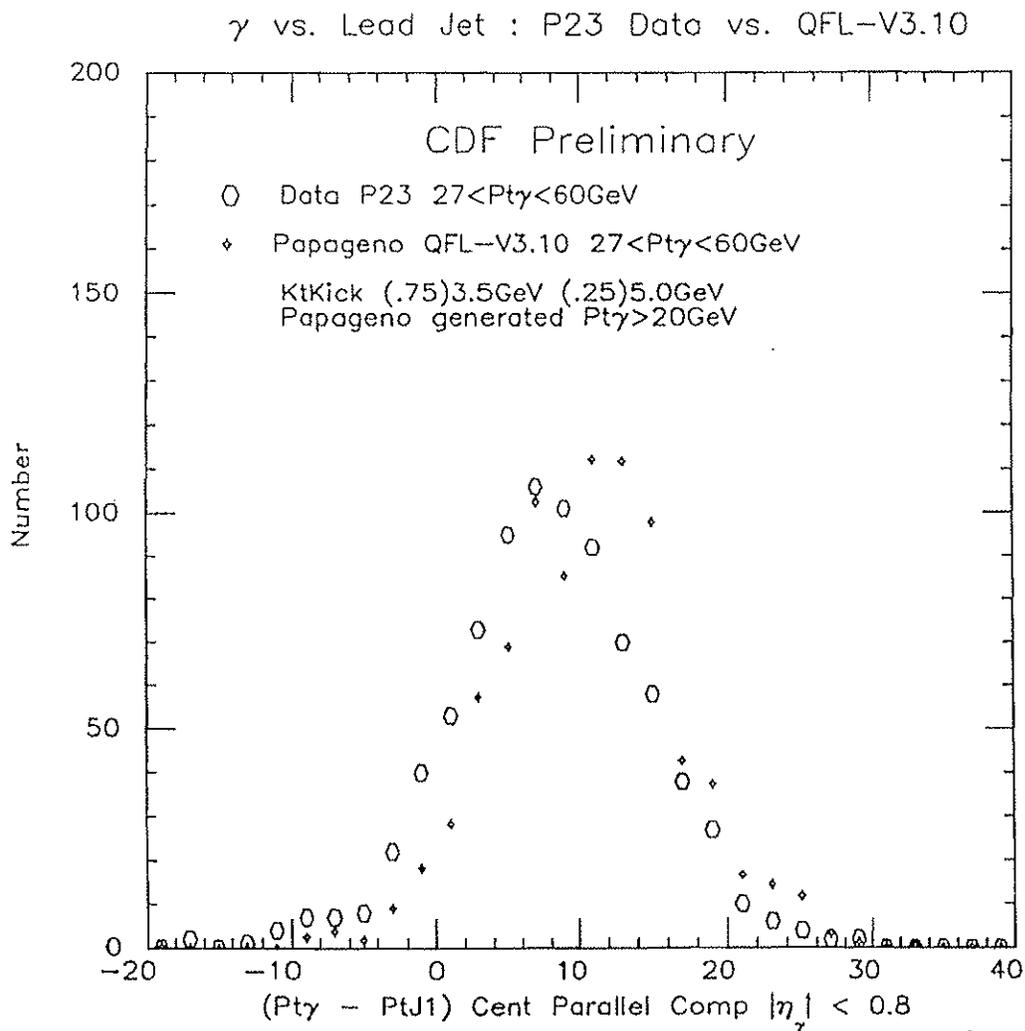
Figure C.13: $K_{T\parallel}$ Component for P23 Data and MC Simulation Without Jet Corrections. $27 < P_{T\gamma} < 60$ GeV and the second jet $P_{Tjet} < 5$ GeV. The mean and RMS's for the distributions are 7.9 and 6.7 GeV for the data and 10.6 and 6.2 GeV for the MC respectively.

P23 Corrected Data
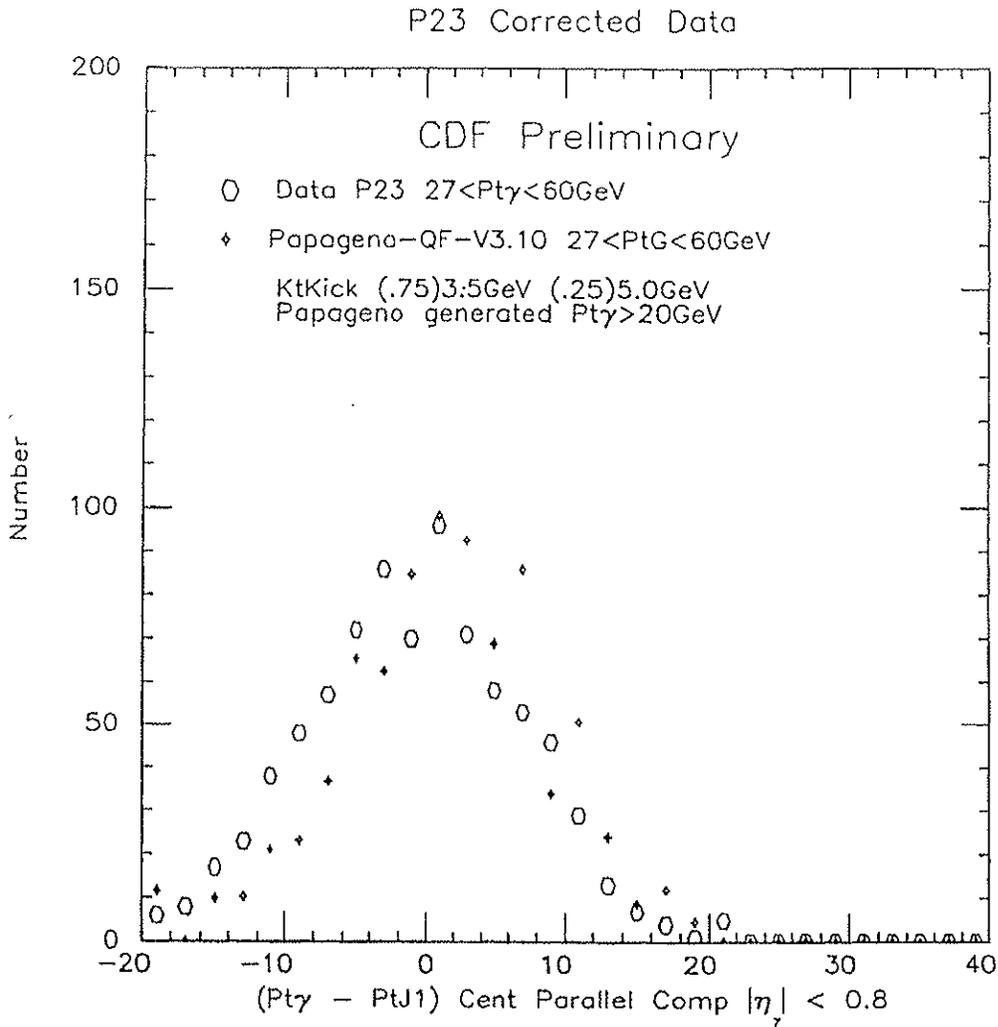
Figure C.14: $K_{T\parallel}$ Component for P23 Data and MC Simulation After Jet Corrections. $27 < P_{T\gamma} < 60$ GeV and the second jet $P_{Tjet} < 5$ GeV. The mean and RMS's for the distributions are $-.07$ and 7.5 GeV for the data and 1.4 and 7.2 GeV for the MC respectively.

Appendix D

Cos θ^* with P10 Data

In this appendix we present the $\cos\theta^*$ distribution as measured from the P10 data. The P10 data is consistent with the P23 data and we originally had hoped to present the data in the body of the thesis both as an independent data set and combined with the P23 data to help reduce statistical and systematic errors. The 10 GeV corrected jet P_T cut was demonstrated to be no problem in the P23 sample because the leading recoil jets were in the 20 GeV range and only a few events had lead jets down near 10 GeV. However in the P10 sample the expected lead recoiling jets would be around 10 GeV and here the possibility of identifying falsely clustered underlying event as the lead jet is very large but of course it is not possible to raise the jet P_T because most of the events would be discarded with no jets. For this reason the P10 data were thought to be unreliable and are presented in the appendix only for completeness.

Variable	Cut	# Passing P10
# 3D tracks	< 1	
P_T Photon	>10 GeV	
P_T Lead Jet	>10 GeV	
Isolation(cone=0.7)	<2.0 GeV (EM Only)	
E_T 2nd CES Clus	<1.0 GeV	
MEtSig	<3.0	
|ZVert| Pos	<50.0 cm	
|StripX| Pos	<17.5 cm	
StripZ Pos	217.0> StripZ >14.0 cm	
Total Passing Level 3		
Total Passing All Cuts		

Table D.1: P10 Events Passing Offline Cuts

D.1   The P10 Data Set and Phase Space Cuts

As reported in Chapter 3 the P10 trigger was added later in the Run and was heavily prescaled in LEVEL 2 and the effective luminosity for the P10 data set was 74 pb^{-1}. The online cuts used to identify good photon candidates were the same as those in the P23 sample except for the level 2 threshold difference and prescale. Offline the additional 2.0 GeV isolation cut was not used on the P10 sample, otherwise all cuts were the same; this was for simplicity because for photons around 10-15 GeV, 15% isolation is pretty much the same as 2.0 GeV and sometimes even more restrictive. The number of events passing various photon candidate cuts are shown in Table D.1.

Obtaining the trigger efficiency for the P10 data was a little trickier than it was for the P23 sample as there was no lower threshold photon trigger than the P10. There was a diphoton trigger that triggered when there were two EM clusters identifiable in an event with P_T's above 5.0 GeV. The efficiency was determined from the diphoton data [49] and the P10 trigger was found to be fully efficient at 16 GeV but again we found it useful to dip

152

lower to 10 GeV and make the corrections. The trigger efficiency can be seen in figure D.1 with the same parameterization used in Chapter 4 as for the P23 data. The fit parameters were A=1.0060 ± .0074, B=0.79736 ± .05313, C=1.5287 ± .00220, D=11.050 ± 0.007.

The same 2 regions of η^*-η_B cuts were made on the P10 data as the P23 to keep the η acceptance as flat as possible. The minimum P_T used in the P10 sample was 10 GeV which allowed the minimum P^* cut to drop to 12.6 and 16.7 GeV in regions 1 and 2 respectively. All others cuts remained the same. Figure D.2 shows the effect of the minimum P_T cut on the usage of P10 data.

D.2   P10 Cosθ^*

The background subtraction for the lower P_T photons is not as sensitive to uncertainty as the P23 sample because the multiple photons from the background at lower average energy are not so merged together and therefore have on average much poorer χ^2 fits to the single electron shower profiles. This reduces the systematic error from the uncertainties in the χ^2 efficiencies but the overall errors are by percentage larger due to significantly poorer statistics in the sample. The data are shown in figures D.3 and D.4 for the Sumjet and Leadjet methods respectively.

The data and their systematic errors before normalization are tabulated in Table D.2.
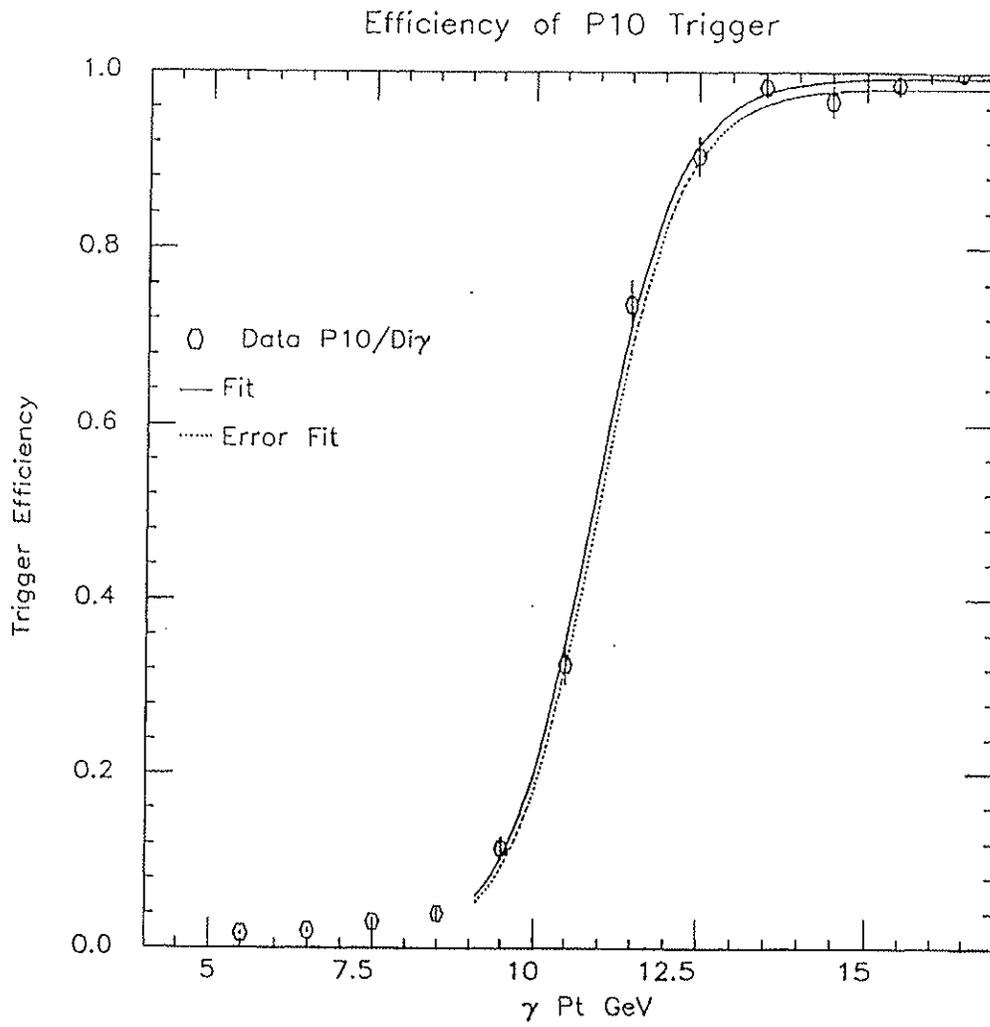
Figure D.1: P10 Trigger Efficiency as Determined from Diphoton Data.

154

Figure D.2: P_T vs η^* for the P10 Data.

155
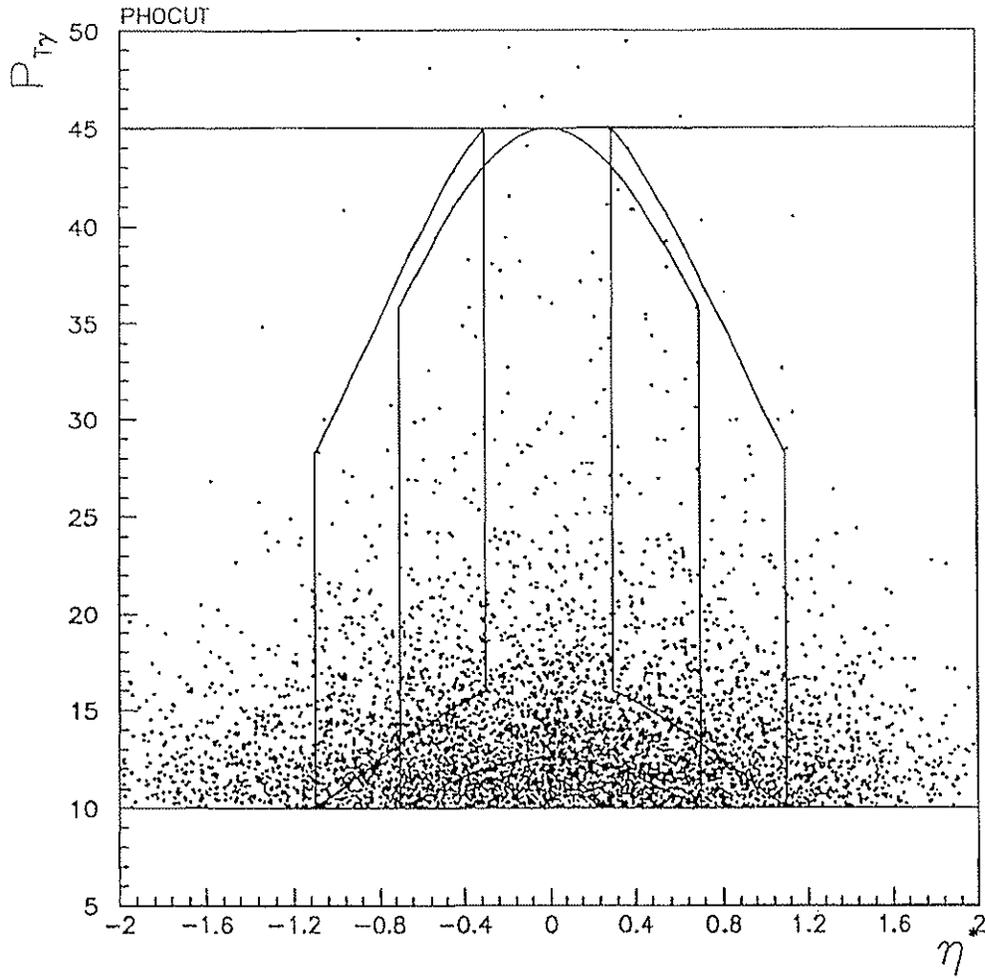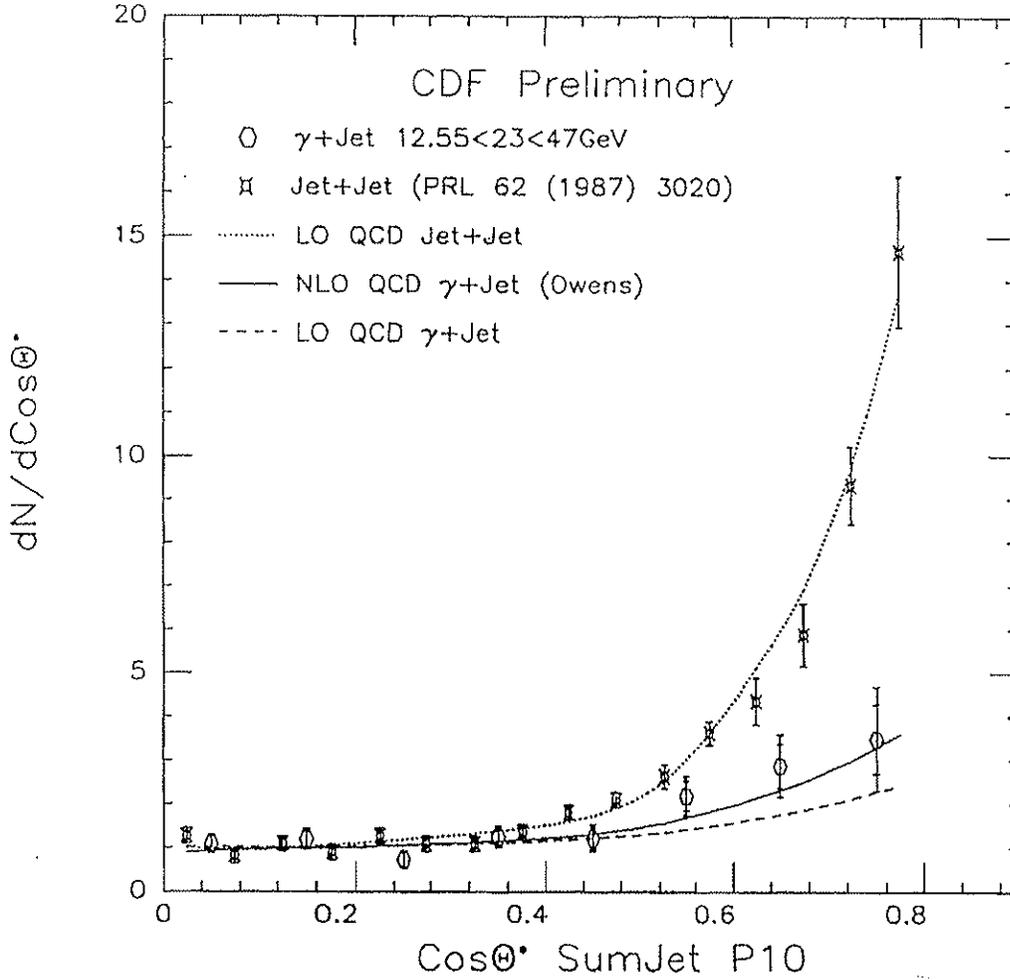
Figure D.3: Direct Photon Cosθ^* for the P10 Data with the Sumjet Method. Background subtracted, inner error bars statistical errors only, outer error bars are statistical and systematic errors added in quadrature.
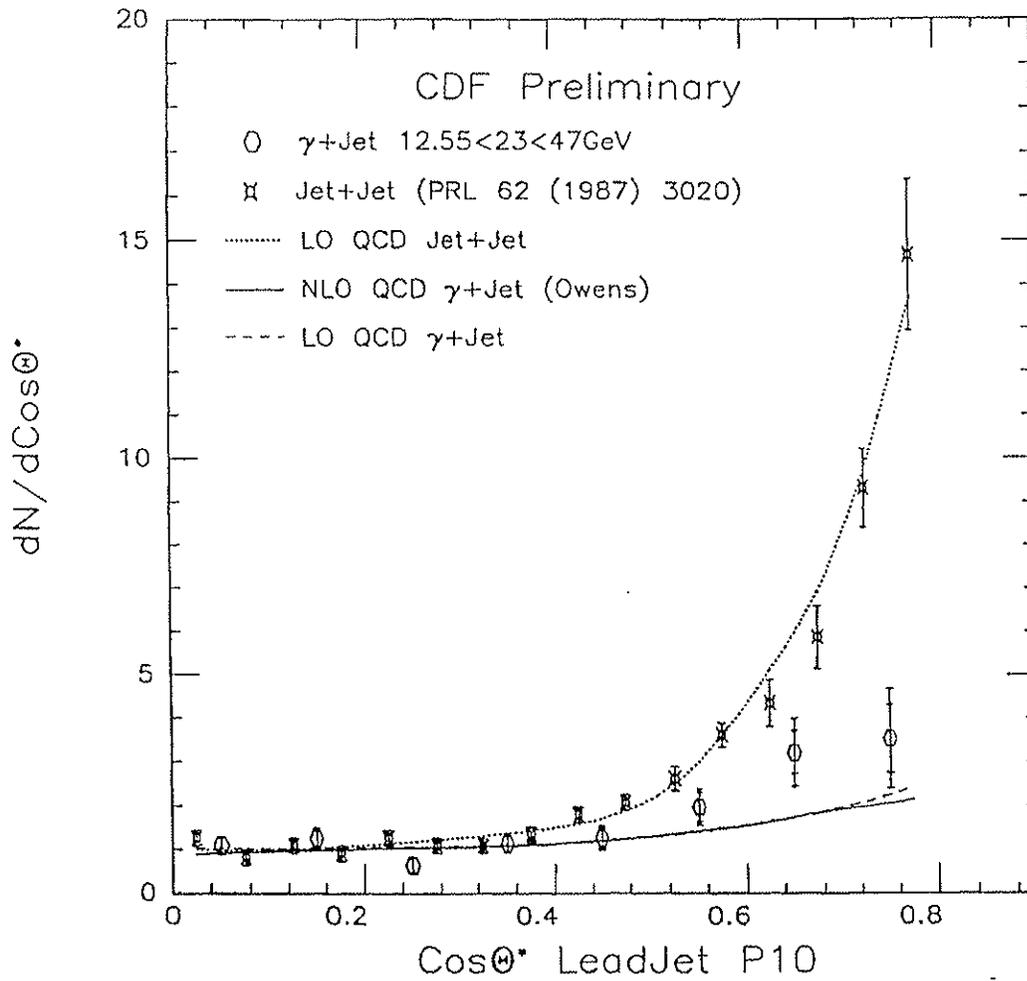
Figure D.4: Direct Photon Cosθ^* for the P10 Data with the Leadjet Method. Background subtracted, inner error bars statistical errors only, outer error bars are statistical and systematic errors added in quadrature.

Sample	$\cos\theta^*$	γ's	Stat	Trig	Acc	Eff	Norm	Tot
P10 SUMJ	.05	95.69	15.56	0.70	3.83	2.87	9.85	19.04
	.15	105.85	16.51	0.90	4.23	2.30	10.89	20.38
	.25	63.96	15.21	0.36	2.56	5.17	6.58	17.55
	.35	110.46	17.88	1.45	4.42	0.31	11.37	21.69
	.45	107.03	21.29	1.80	4.28	11.46	11.01	26.98
	.55	192.48	30.45	5.67	7.70	7.94	19.80	38.39
	.65	91.18	15.95	0.59	4.10	0.44	16.04	23.01
	.75	110.85	25.66	2.70	4.99	19.16	19.51	37.93
P10 LeadJ	.05	105.88	16.82	0.74	4.24	2.54	10.65	20.52
	.15	121.75	17.51	0.88	4.87	5.06	12.25	22.51
	.25	60.61	15.85	0.40	2.42	7.60	6.10	18.76
	.35	109.62	19.05	1.34	4.38	3.25	11.03	22.72
	.45	122.72	21.90	2.05	4.91	7.78	12.34	26.85
	.55	190.29	31.28	6.17	7.61	9.16	19.14	39.05
	.65	107.02	16.23	0.85	4.82	4.40	18.90	25.77
	.75	117.59	25.64	2.74	5.29	17.30	20.76	37.93

Table D.2: Sources of Error in the P10 Data

Appendix E

Loose Ends

E.1   Background Cos θ^*

Since we use the CES χ^2 to subtract the background from the signal and then demonstrate that the resulting $\cos \theta^*$ distribution looks nothing like the dijet angular distribution, it is natural to ask what does the background angular distribution look like? It is not completely clear what the background angular distribution should be like as isolation cuts may preferentially select certain dijet diagrams over others due to subtleties in parton coupling differences between quarks and gluons or to the details of fragmentation and the application of the isolation cuts for photon identification. However, one does expect the background angular distribution to be be more forwardly peaked like the dijet distribution than the direct photon distribution because of the presence of gluon propagators to all orders. The very strict isolation cuts were designed to reduce the background as much as possible and so the 'subtracted' leftover background has very poor statistics. We can however reverse some of our isolation cuts and try and enhance background rather than signal and subtract out

the signal and see the result. To do this the very strict isolation requirements were reversed. Events were passed if the energy within the cone of r=0.7 had unclustered EM $P_T \gtrsim 2.0$ GeV and if there was a second strip cluster with $P_T > 1.0$ GeV. All photon triggers online passed a 15% isolation for a cone of r=0.4, so this represents the minimal isolation. The plots are shown in figures E.1 and E.2 for the Sumjet and Leadjet methods respectively.

The angular distributions for the background (both methods) are consistent and they are close to the dijet distribution, but not quite as steep. We offer them without further comment.

E.2 LO, NLO and α_s

It is of some interest to measure the running of α_s over P_T ranges covered by the direct photon data reported here. The difference in CM angular distribution between the LO and NLO direct photon subprocesses permits a potentially powerful method of performing such a measurement. The first step would be to place hard cuts on the jets to try and isolate positively $2 \rightarrow 2$ (γ+jet) and $2 \rightarrow$ (γ+2jet) events and compare the CM angular distribution of each isolated subprocess to the theoretical prediction. If all matches well then one could fit the theoretical LO and NLO diagrams to the data allowing the relative amounts of each (dependent upon α_s) to be the free parameter. The best fit would give the best guess of α_s. This prescription has many pitfalls and is wholly dependent upon the separability of the subprocesses into distinct final state diagrams. It is also somewhat dependent upon good theoretical treatment of gluon bremstrahlung radiation to NLO. It does however exploit the most dramatic and easily distinguishable feature of LO and NLO direct photons, their

160

Background dN/dCosΘ*
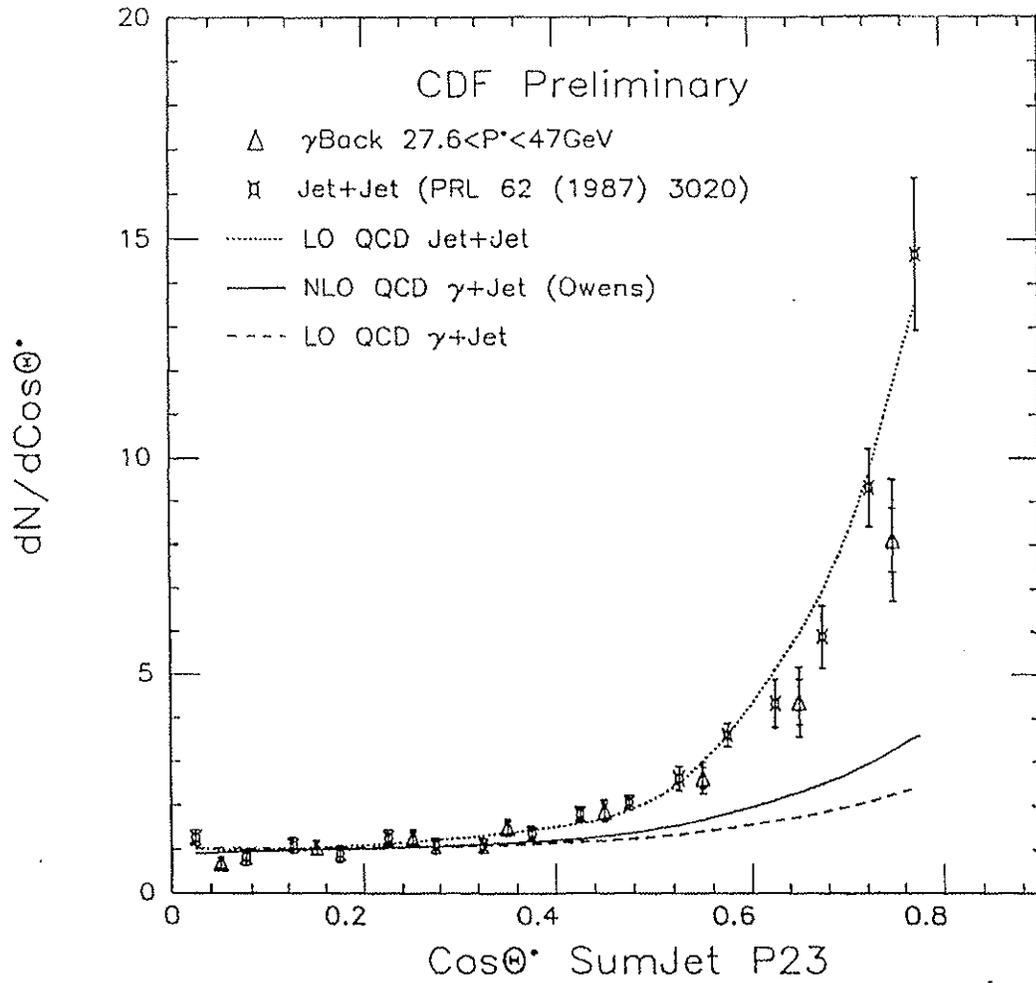
Figure E.1: Isolated Background Cosθ^*. Signal subtracted, Sumjet method.

Background dN/dCosΘ*
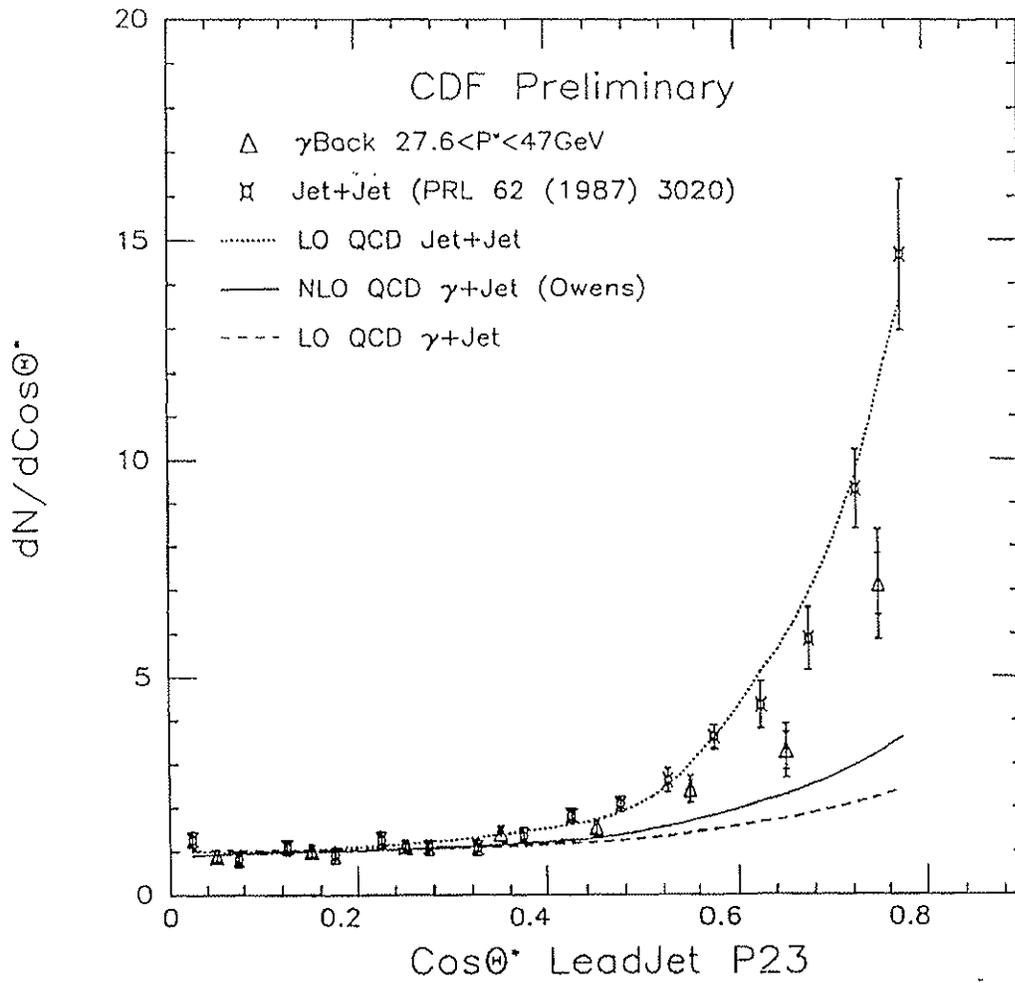
Figure E.2: Isolated Background Cosθ^*. Signal subtracted, Leadjet method.

CM angular distribution. Unfortunately with this data set it is not possible to do this with a background subtracted data set as the statistical and systematic uncertainties become too large; however it is possible to demonstrate that there is a difference in CM angular distribution between LO and NLO events.

Given all these caveats, the data are shown in figure E.3 with the sumjet method only and all the cos θ^* cuts used in Chapter 6. The circles are the data shown in Chapter 6 (all data passing cuts), the squares are the data with a hard cut on the second jet P_T <5.0 GeV (corrected) to select from the sample events that are likely to be LO only. The triangles are the data with a cut on the second jet P_T >7.0 GeV (corrected) to select a sample that is likely to be higher order only. The steeper rise of the triangles compared to the other curves is to be noted.

Direct Photon dN/dCosΘ* Unsubtracted Data
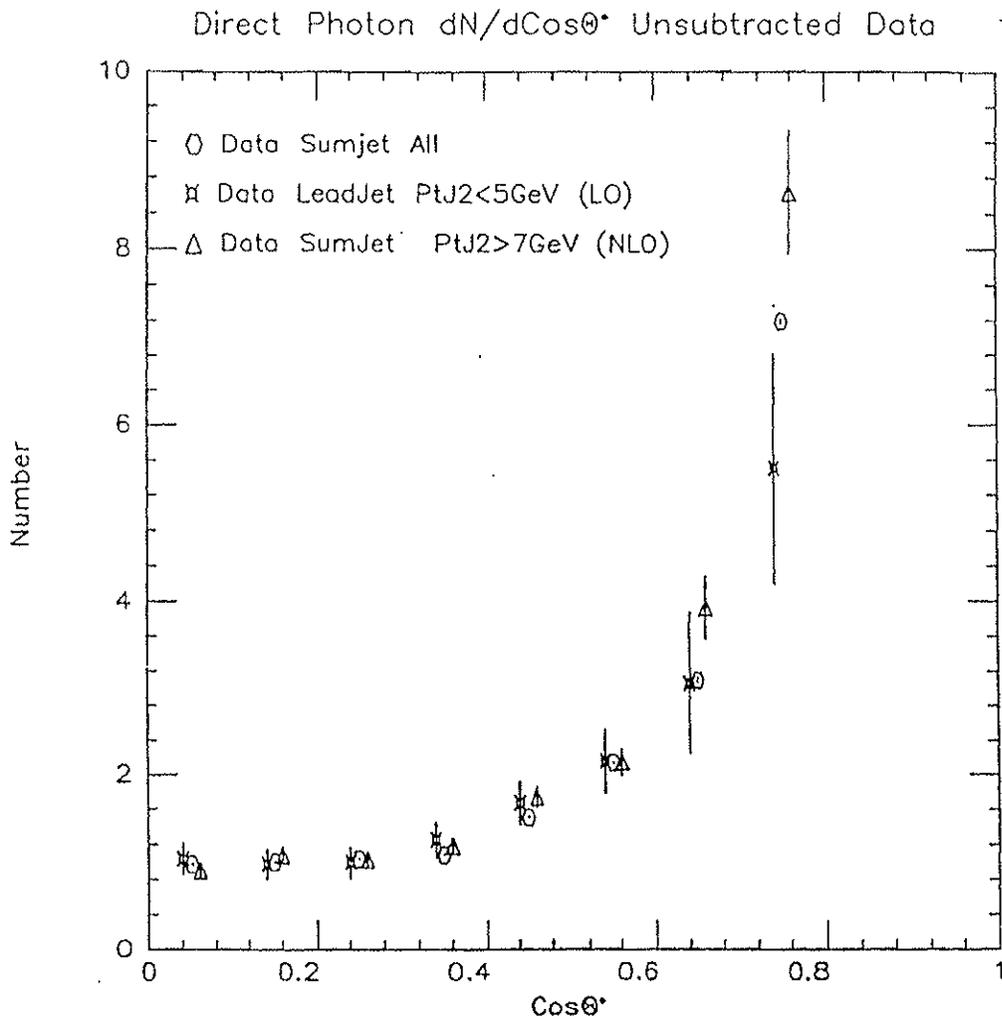
Figure E.3: Unsubtracted Data CosΘ* for Data with Hard Cuts on the Second Jet. Statistical errors only.

Bibliography

[1] E. Rutherford, Phil. Mag., **21**, 669 (1911).

[2] R. Hofstadter, Ann. Rev. Nucl. Sci., **7**, 231 (1958).

[3] M. Briedenbach *et al.*, Phys. Rev. Lett., **23**, 935 (1969).

[4] M. Gell-Mann and Y. Ne'eman, Phys. Lett., **8**, 214 (1964).

[5] G. Zweig, CERN Preprint TH401, (1964).

[6] J.E. Augustin *et al.*, Phys. Rev. Lett., **33**, 1406 (1974).

[7] J.J. Aubert *et al.*, Phys. Rev. Lett., **33**, 1404 (1974).

[8] S.L. Glashow, Nucl. Phys., **22**, 579 (1961).

[9] S. Weinberg, Phys. Rev. Lett., **19**, 1264 (1967).

[10] A. Salam, Nobel Symposium #8, edited by W. Svartholm (1968).

[11] F.W. Busser *et al.*, Phys. Lett., **46B**, 471 (1973).

[12] B. Alper *et al.*, Phys. Lett., **44B**, 521 (1973).

[13] G. Altarelli and G. Parisi, Nucl. Phys., **B127**, 298 (1977).

[14] E. Eichten *et al.*, Rev. of Modern Phys., 56, No.4, Oct. (1984).

[15] R.K. Ellis and J.C. Sexton, Nucl. Phys., 269, 445 (1986).

[16] J.F. Owens, Rev. of Modern Phys., 59, no.2, 465 (1987).

[17] H. Bauer, J. Ohnemus and J.F. Owens, Phys. Lett. 234B, 127 (1990).

[18] D. Pierce and I. Hinchcliffe, Private Communication.

[19] I. Hinchcliffe, Papageno Event Generator, Private Communication.

[20] C. Fabjan and T. Ludlam, Ann. Rev. Nucl. Part. Sci., 32, 335 (1982).

[21] F Abe, *et al.*, Nucl. Instr. Meth. Phys. Res., Sect. A 271,387 (1988).

[22] L. DeMortier, CDF Gas Gain DAQ, CDF Note# 533.

[23] J. Walsh, Alarms and Limits, CDF Note #1159.

[24] V. Scarpine, Ph.D. Thesis, University of Illinois, December (1991).

[25] B.L. Winer, Ph.D. Thesis, University of California, Berkeley, February, (1991).

[26] G. Drake *et al.*, Nucl. Inst. Meth. in Phys. Res., 269, 68 (1987).

[27] E. Barsotti *et al.*, Nucl. Inst. Meth. in Phys. Res., 269, 82 (1987).

[28] D. Brown and M.E.B. Franklin, CDF Note #605.

[29] D.N. Brown and M.D. Shapiro, CDF Note #874.

[30] P. Derwent, Ph.D. Thesis, University of Chicago, December (1990).

[31] W. Trischuk, Ph.D. Thesis, Harvard University, April (1990).

[32] T. Hessing, Ph.D. Thesis, Texas A&M University, December(1990).

[33] F. Abe *et al.*, Phys. Rev. Let., to be submitted.

[34] B. Hubbard, Ph.D. Thesis, University of California, Berkeley, November (1989).

[35] D.N. Brown, Ph.D. Thesis, Harvard University, June (1989).

[36] F. Abe *et al.*, Phys. Rev. D., **43** no. 7, 2043 (1991).

[37] F. Abe *et al.*, Phys. Rev D., to be submitted.

[38] L.F. Nakae, CDF note #1475.

[39] R.M. Harris, CDF Note #1329.

[40] Particle Data Group, Phys. Lett. B., **239**, (1990).

[41] R.M. Harris, CDF Note #1472.

[42] M. Schub, Ph.D. Thesis Purdue University, (1989).

[43] F. Abe *et al.*, Phys. Rev. Lett., **62**, 3020 (1989).

[44] L.F. Nakae, CDF Note #1739.

[45] R.M. Harris, S. Kuhlmann, and R. Blair, CDF Note #1432.

[46] P. Bagnaia *et al.*, Phys. Lett., **144B** 283, (1984).

[47] D.N. Brown and B.L. Flaugher, CDF note #1340.

[48] L. Keeble, and B.L. Flaugher, CDF note #1513.

[49] M. Takano, Ph.D. Thesis, Tsukuba University, (1992).